DEVELOPMENT OF AN EXPERIMENTALLY-VALIDATED COMPACT MODEL OF A SERVER RACK

A Thesis
Presented to
The Academic Faculty

by

Graham Nelson

In Partial Fulfillment
of the Requirements for the Degree
Master of Science in the
School of Mechanical Engineering

Georgia Institute of Technology
December 2007

DEVELOPMENT OF AN EXPERIMENTALLY-VALIDATED

COMPACT MODEL OF A SERVER RACK

Approved by:

Dr. Yogendra Joshi, Advisor
School of Mechanical Engineering
Georgia Institute of Technology

Dr. S. Mostafa Ghiaasiaan
School of Mechanical Engineering
Georgia Institute of Technology

Dr. Sheldon Jeter
School of Mechanical Engineering
Georgia Institute of Technology

Date Approved: August 13, 2007

ACKNOWLEDGEMENTS

I would like to thank my advisor, Dr. Joshi, for all of his encouragement and for sharing some of his seemingly-infinite thermal-management wisdom with me along the way. I also really appreciate the support of my committee members, Dr. Ghiaasian and Dr. Jeter.

I also could not have done this without the help of my colleagues and friends from the Microelectronics Thermal Laboratory at Georgia Tech. Every single person in this group was always willing to offer insight or to help any way they could.

I would especially like to thank the gentlemen in the data center labs. Thanks to Dr. Jeff Rambo for his patience and guidance early on. I would like to also extend a special thanks to Qihong Nie and Ludovic Burton for their participation in many useful brainstorming sessions. I would like to say thank you also to David Harman for his assistance in the lab. Lastly, I'd like to thank the fellas in Dr. Garimella's group for putting up with all of the noise that resulted from the heated arguments between the data center guys.

TABLE OF CONTENTS

LIST OF TABLES

LIST OF FIGURES

LIST OF SYMBOLS

f_{app}	apparent friction
p	pressure
N	number of fins
H	fin height
L	fin length
b	width of heat sink gap
W	heat sink total width
υ	velocity
ρ	density
K_c	coefficient of contraction
K_e	coefficient of expansion
x^+	hydrodynamic entry length
μ	viscosity
α	permeability
Δm	thickness of porous medium
k_L	loss coefficient
Re	Reynold's number
D	hydraulic diameter
λ	friction number
k_R	absolute roughness
ζ	resistance coefficient
$\Delta\overline{T}$	difference between the mean outlet temperature and inlet temperature
S_i	pressure drop source term (pressure drop per unit length along flow direction)

D_{ij}	Darcy coefficient matrix
C_{ij}	inertial resistance coefficient matrix
C_2	inertial resistance factor
$1/\alpha$	viscous resistance coefficient
γ	porosity
E_f	total fluid energy
E_s	total solid energy
k_{eff}	porous media effective thermal conductivity
ρ_f	porous media fluid density
ρ_s	porous media solid density
S^h_f	fluid enthalpy source term
k_f	porous media fluid thermal conductivity
k_s	porous media solid thermal conductivity
U_θ	fan swirl tangential velocity component
U_r	fan swirl radial velocity component
r	radial distance from fan center
I	turbulence intensity
ΔT_{max}	difference between the maximum outlet temperature and the inlet temperature
$\dot{m}$	mass flow rate
c_p	specific energy
q	heat transfer rate
$C_{1\varepsilon}$, $C_{2\varepsilon}$, C_μ	input constants in k-ε turbulence model
σ_k, σ_ε	turbulent Prandtl numbers

LIST OF ABBREVIATIONS

CFD-HT	Computational Fluid Dynamics and Heat Transfer
CRAC	Computer Room Air Conditioning
MTBF	Mean Time between Failures
VFD	Variable Frequency Drive
RFP	Raised-Floor Plenum
HVAC	Heating, Ventilation, and Air Conditioning
POD	Proper Orthogonal Decomposition
TEC	Thermoelectric Cooler
CFM	Cubic Feet per Minute (ft^3/min)
GPM	Gallons per Minute (gal/min)
ADC	Analog-to-Digital Converter
PIV	Particle Image Velocimetry
SNR	Signal-to-Noise Ratio
CCD	Camera Charging Device
Re	Reynolds Number
POD	Proper Orthogonal Decomposition
RTD	Resistance Temperature Detector

SUMMARY

A simplified computational fluid dynamics and heat transfer (CFD-HT) model of an electronics enclosure was developed. The compact model was based on a server simulator, which dissipates a variable amount of heat at an adjustable air flow rate. Even though a server simulator does not accurately represent the geometry of an actual electronics enclosure, the modeling of such a unit deals with many of the same issues as the modeling of actual enclosures. Even at the server simulator level, a disparity in length scales prevents detailed modeling of intricate components – most notably grilles, fins, and fans. Therefore, a compact model for each of these components was developed. Fan performance curves were determined experimentally for varying fan rotational speeds. In addition, component pressure drop characteristics were found experimentally for grilles and fin banks, and these empirical relationships were applied to the model as well. To determine the validity of the simplifications employed in the model, experimental outlet temperature and velocity measurements were taken to compare to those provided by the CFD-HT simulations.

CHAPTER 1

INTRODUCTION

Data processing equipment – such as servers, telecommunications hardware, and data storage devices – is commonly contained within a standardized cabinet enclosure, or rack. The performance of this equipment is highly dependent on the ability to maintain the operating temperatures within a specified range. Because of the extremely high heat load densities associated with this type of machinery, and because of the necessity to protect equipment at all lengthscale levels, common methods used in the cooling of typical occupied spaces – such as offices and auditoriums - is far from adequate. Special data center facilities are devoted to attacking this problem.

Most modern data centers protect the equipment within by removing heat at the room level – rather than at the chip level, which is handled by the vendors of the specific equipment. A significant characteristic of data centers is the existence of multiple lengthscales, ranging from those at the chip level to the room level. The development of a CFD-HT model that is detailed enough to resolve all of these patterns would pose too large of a computational demand to be feasible at the current time or in the foreseeable future. Therefore, the thermal design of most data centers is often based solely on past experience and "best practice" approaches.

The heat generated by the electronic hardware is commonly removed at the room level by Computer Room Air Conditioning (CRAC) units. In the past, the units have been sized and place in the room based on an estimation of mean heat loads. This often leads to over or under-provisioning of cooling resources. The resulting inefficiencies in data center thermal management have driven a recent need to develop software tools that will provide more accurate predictions of the temperature and velocity patterns in data centers. In order to overcome the computational demands necessary to make fully

resolved predictions, engineers must utilize a number of assumptions in simplifying the detailed geometries and airflow characteristics. These assumptions are needed at multiple lengthscales.

This thesis presents a method of characterizing data center thermal characteristics at the rack level. The model presented here is based on a rack composed of four server simulators, which were stacked in a cabinet. It was necessary to employ many simplifications in creating a CFD-HT model of a server simulator. Experimental data from these server simulators were used in providing boundary condition input information for compact component models, as well as for comparison with system-level simulations.

This chapter will provide basic background information on data center designs and on ongoing efforts to improve data center design methods. Representative results from prior related studies – both experimental and analytical – will be summarized. Current methods of developing compact or reduced-order models of server racks and other sub-systems of electronics enclosures will also be discussed.

1.1 Thermal Management of Mission-Critical Electronic Equipment

A company's electronic equipment is often mission-critical. Therefore, it is extremely important to ensure that that equipment is well-protected. The amount of power that a computer processor can have depends on the ability to remove the heat. In the past, cooling schemes were developed based on simple energy balances and "guess and check" approaches. Fans and heat exchangers were oversized in order to account for any errors in these approximations. Because the heat loads of computer equipment are now much more highly concentrated (at the chip level), it is inadequate to develop cooling strategies based on simple energy balances. Failure of electronic equipment does not occur when the mass-averaged temperature of a system or a sub-system reaches critical temperatures. Failure occurs at the chip. Designers of thermal management schemes must keep this in mind, and new techniques of heat removal must be developed, or the industry will hit a brick wall.

A data center is essentially any facility that is used to house large quantities of electronic equipment. The equipment in such a facility usually performs one of three tasks: data processing, data storage, or telecommunications. The facility can either be private (owned by a single company) or shared by multiple users. Most medium-sized to large company have one or more data center facilities, which vary in size – from a small room inside an actual office space to an off-site facility that can be as large as 50,000 m^2 or more. Figure 1 shows a typical medium-sized data center facility.

Figure 1: Typical Data Center Facility [1]

Electronic equipment in data centers is typically stacked into enclosures known as cabinets or racks (see the figure above) to protect the electronics from dust and other particulates in the air. The racks allow the passage of air through grilles located strategically at the front and back of the rack, or at the top and bottom – depending on the cooling scheme. The amount of space in a rack is conventionally measured in a unit known as a U, where one U is equal to approximately 45 mm (1.75 in). Though racks vary in size, the standard rack, defined by ASHRAE, is 42U in height (1.82 m), with a footprint of 610 mm (24 in) by 1020 mm (40 in).

At one time, a rack of this size was only able to accommodate one or two computers, but currently, it might hold as many as 60 or more high-density computers or "blade servers" [2]. Although these computers are compact in design, they are still each able to carry out all of the tasks of a full-sized computer; thus, the management of the dissipated heat is often a difficult task – especially given that the data center is full of these racks. To get an idea of the amount of heat dissipated by these facilities as compared to standard office spaces, consider the following: according to [2], a typical PC consumes approximately 250 W over a footprint area of 0.0728 m^2, which equates to a

power density of approximately 3,500 W/m^2. A current cabinet, on the other hand, with a 0.619 m^2 server rack may dissipate around 6 kW of heat (or more), which equates to a power density of about 9,700 W/m^2 – about three times the amount of heat per unit area of a standard PC. In fact, the heat densities of this type of equipment are expected to continue to increase over the next several years according to projections by ASHRAE (See Figure 2).

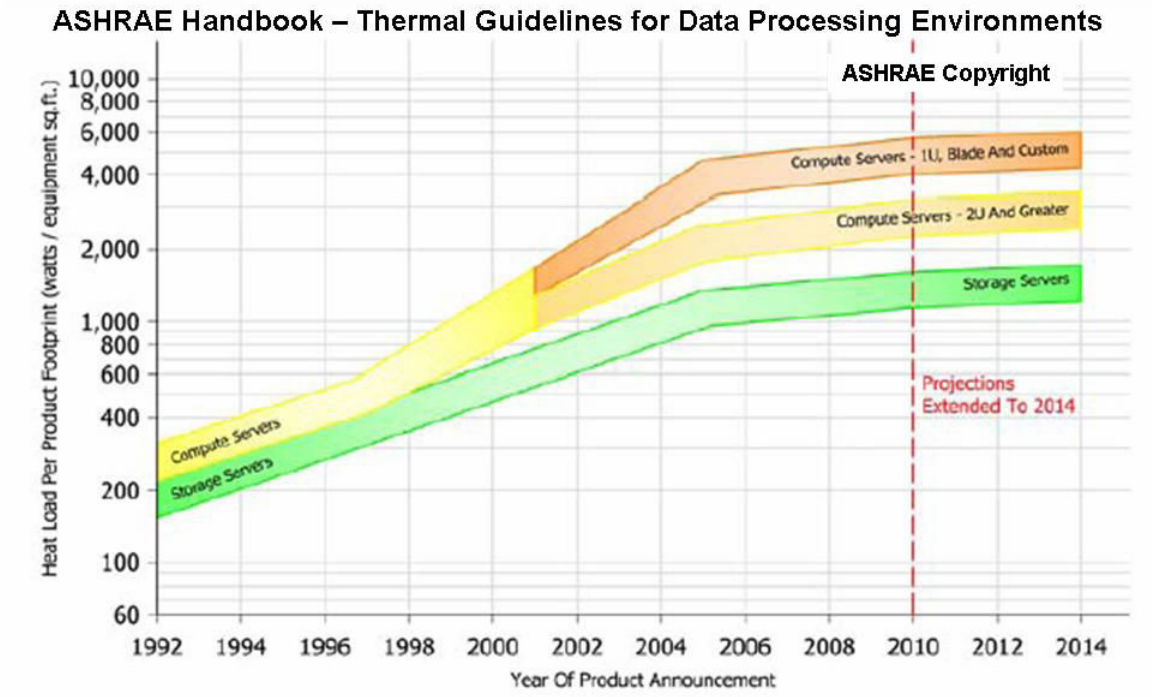

Figure 2: Heat Density of Data Processing Equipment Over Time [2]

The world's economy is highly reliant on this computer equipment being in operating order, and for many companies, such equipment is mission-critical. Therefore, it is extremely important for such equipment to be well-protected and well-maintained. Because of the high heat densities associated with data centers, standard cooling schemes such as those used for office spaces or even large amphitheatres are simply inadequate. Special measures must be undertaken to ensure that such equipment will operate under safe conditions.

Often, the approach to designing a thermal management scheme of a data center facility is based on sets of guidelines, which are derived from previous data center observations. To improve on this practice, much effort has recently been placed on making predictions using computational fluid dynamics and heat transfer (CFD-HT) modeling (Refer to Appendix A for a brief description of CFD).

1.2 Data Center Thermal Design Based on Empirical Observations

The state-of-the-art data center removes heat by way of Computer Room Air Conditioning (CRAC) units, which are usually housed within the facility along with the electronic equipment. The CRAC units create a self-contained air-cooling system, where air is circulated only within that data center space. The heat is removed through a chilled water loop, in which a pump delivers chilled water to the CRAC units from a chiller that is located outside the facility. The chiller typically delivers chilled water to the CRAC units at approximately 11^{o}C (52^{o}F). A blower then forces air over a heat exchanger coil (most often a fin-and tube) in the CRAC unit and passes the air into the room. While some CRAC units do utilize a Variable Frequency Drive (VFD) fan, they are typically designed to run at a fixed fan speed, and a chilled water valve is used to vary the supply air temperature. That supply temperature is varied based on the return air temperature, as measured by sensors on the CRAC return.

The CRAC units may be either “downflow” or “upflow,” depending on the designed cooling scheme of the space. An **upflow** unit, often utilized for an office or telecommunications equipment facility, delivers cooled air through ducts that are routed above the room to supply diffusers located along the ceiling. The air then passes through the racks, removing heat from the enclosed electronic equipment. The heated air is then returned to the CRAC units through the front or side.

It is much more common for a data center to employ one or more **downflow** (rather than upflow) CRAC units to deliver air through a space beneath the floor, which is

known as a plenum. This type of facility is known as a Raised Floor Plenum (RFP) data center. Figure 3 shows a schematic of the air flow within this type of facility [1]. The floor of the facility is built above a plenum, which allows the passage of cool air delivered by the CRAC unit blowers. The chilled air is delivered to the room through porous tiles arranged strategically around the floor of the facility. The chilled air comes up through the floor, passes through the racks, rises to the ceiling, and is returned through the top of the unit, where it is then cooled by a chilled water heat exchanger.

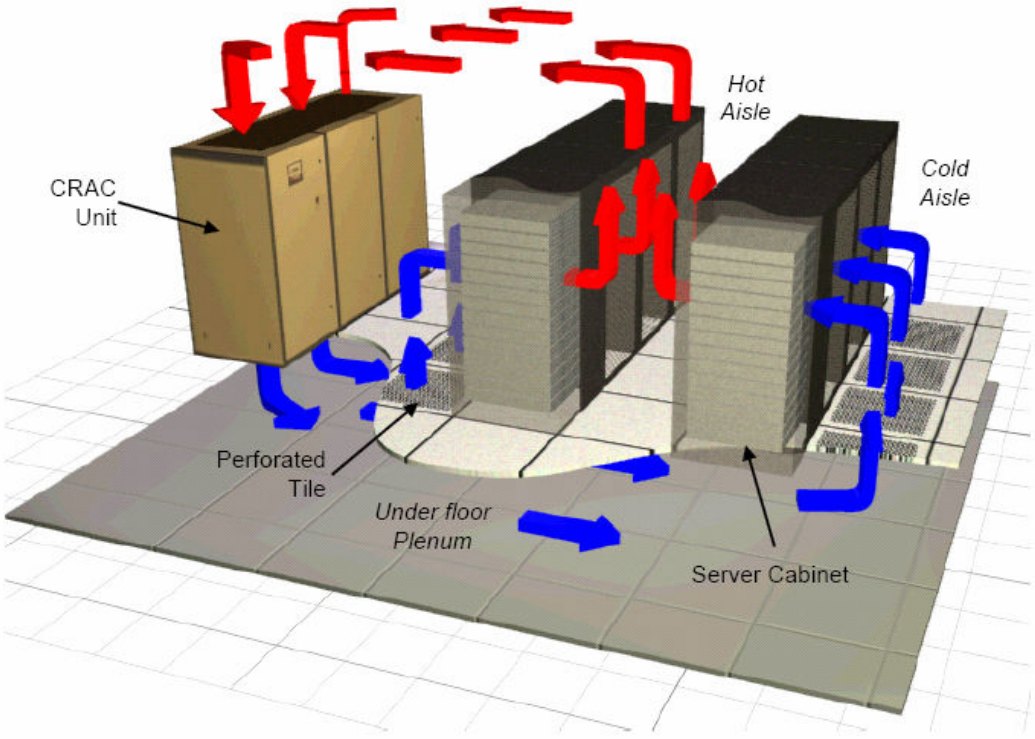

Figure 3: Air Flow Schematic of a RFP Data Center [1]

Data center plena can range in height from 30.5 cm (1 ft) to over 91 cm (3 ft). The height of the plenum often depends on the amount of available space between floors, although the typical plenum has a depth of around 46 cm (18 inches).

The heat is removed at the room level, whereas it is being generated at the chip level. This presents a significant problem. Different electronic equipment will dissipate

different heat loads, and also because the real data center is a dynamic environment, the CRAC equipment must be oversized and electronic equipment must be placed in the room according to a prediction of the expected thermal patterns. If the room is not laid out well, hot spots will exist, and the CRAC units will have to oversupply the room with cold air. A superfluous amount of cold air will go to units that don't need it in order for the warmer parts of the room to be cooled sufficiently. This of course is extremely inefficient. It is estimated that if current technologies were implemented correctly, a 25% savings in the required cooling power could be achieved [3].

Many steps can be taken to increase the efficiency of the thermal management scheme in a data center facility; for example, the tiles in the above figure (Figure 3) are arranged in what is known as a hot aisle-cold aisle arrangement. The idea is that a designer must separate the cold supply air from the warm exhaust air by alternating rows of perforated and non-perforated tiles. Imagine, on the other hand, that the porous aisle on the right in the above figure were moved and placed between the two rows of racks. In that scenario, the warm exhaust from the left aisle of racks would mix with the cold supply air entering the racks on the right, reducing the cooling effectiveness.

The so-called hot aisle-cold aisle arrangement is one of many "best practices" of data centers, as laid out by ASHRAE in [4]. Many of the design guidelines for these types of facilities are based on "rules of thumb" determined from past experience and empirical investigations of data center facilities. Several of these best practices are given in [2]. For example, it is recommended that the hot aisles be separated by the cold aisles with an actual physical structure.

Another such best practice observation is that the static pressure in the plenum – created by the CRAC blowers – is non-uniform, and this creates a non-uniform distribution of air flow rates throughout the room. Care must be taken to place racks accordingly. Many factors lead to the non-uniform distribution of static pressure in the plenum, such as the plenum footprint, the CRAC position, the perforated tile porosity, the

arrangement of perforated tiles, and the plenum depth. In [5, 6], the air flow through porous tiles was studied in an experimental facility containing a thin row of porous tiles leading away from a CRAC unit. In that study, it was observed that a high velocity near the CRAC exhaust would create a relatively low static pressure in the plenum, which would result in reversed flow – or air being pulled from the room to the plenum – through the porous tiles in close proximity to the CRAC units. In [7], it was predicted that a deeper plenum would reduce the CRAC exhaust speed enough to more evenly distribute the air throughout the room. Measurements were taken in [8] to determine if this reversed flow phenomenon would occur in a facility with a deeper plenum and with a room with a wider footprint. The data confirm that a data center with a deeper plenum would distribute the air more evenly. Reversed flow rarely occurs. So, it was concluded that it is better to have a deep rather than a shallow plenum.

There are many of these types of observations that are applied during the data center design phase [2]. For example, the first row of porous tiles should be a minimum of three tiles away from CRAC units, and porous tiles should always be arranged in aisles rather than in random locations. Also, all leaks in the floor should be adequately sealed in order to prevent wasted cold air.

In [9], an experimental investigation of a data center was performed. This study looked at the effect of rack placement on the inlet and outlet temperatures. A row of racks was placed in front of a CRAC unit. It was found experimentally that the mean temperatures of racks in a row would vary by as much as 17^{o}C. It was also found that the inlet temperature to a rack would increase almost linearly from a vertical position of 500 mm to a vertical position of 1700 mm by approximately 4.5^{o}C. Lastly, it was noticed that this change in inlet temperature would in turn affect the outlet temperatures of a rack. The study showed that the outlet temperature would increase by 5 or 6^{o} from a vertical position of 500 mm to a vertical position of 1700 mm.

While much of this type of information is quite useful, there is a large drawback to designing data centers based on guidelines developed by past observations of different facilities. No two data centers are exactly alike. A designer must develop some way of predicting what cooling scheme would work best for a particular facility. When a data center is being designed and built, it is difficult to predict air flow and temperature patterns based on previous data centers. Therefore, numerical techniques must be developed to provide a more effective framework for an efficient design.

1.3 Data Center Thermal Design Based on Analytical Predictions

As previously mentioned, current practice is to size the air conditioning units based on total energy balances, and racks are simply placed in a room based on basic intuition and "best practices." In reality, the heat loads in data centers are almost always non-uniformly distributed [10]. After a data center is designed and built, and the equipment is placed in the facility, racks are often simply shifted around in order to keep the racks with the highest heat loads in areas of the room known to have lower temperatures or higher air flows. This is inefficient and time-consuming. To provide a more accurate framework for designing these facilities, many efforts have been made to predict the thermal behavior of data centers using either curve-fitting computer programs or CFD-HT.

It has been shown [10] that using some sort of predictive method to obtain the temperature and velocity maps of a data center could help improve the efficiency. In [11], a method was developed to obtain a detailed model of the thermal behavior of a data center based on experimental data taken throughout the facility. In essence, they created a way to estimate the thermal map of a data center as a function of three different inputs, which are described as follows. The **workload distribution** was defined as the distribution of heat around the data center. The **cooling configuration** included the CRAC unit distribution, air flow, and supply temperature, along with factors such as

server fan speeds. Lastly, the **physical topology** was basically defined as the placement of physical objects in the room (including doors, walls, server racks, etc.). It was assumed that the temperature map is a function of these three parameters alone. Temperature points were measured throughout the room, and those data were used to "train" the software. Another set of measurements was compared to predictions by the "curve-fitted" model, and over 75% of their predictions were within 0.5^{o}C and over 92% were within 1^{o}C.

The previous method disposes of the physics of the system in the interest of simplification (and a reduction in the required computational effort). Since each data center is different, it would be impossible to use a previous curve-fitted model of a data center to predict what would happen in a planned facility where experimental data are not available. Thus, it would be better to develop models based on physical laws that govern fluid flow and heat transfer. This is the basis of CFD-HT.

In [12], a commercial CFD-HT code, Fluent, was used to develop a 2D model of a data center to determine the effect of total heat input, inlet air velocity, rack spacing, location of the HVAC system, ceiling height, inlet air temperature, rack density and floor height on the maximum temperatures of electronic components. Additionally, a study was performed to determine the sensitivity of temperature to the different turbulence models that can be used in a CFD-HT solver. Table 1 contains these results. The results show that the chosen turbulence model has a large effect on both the computational demand (represented by the number of nodes of each case required for convergence) and the temperature results.

Table 1: Effect of Turbulence Models on Temperature [12]

Turbulence Model	T_{max} (^oC) of Case 1	T_{max} (^oC) of Case 2	Number of Nodes in Case 1	Number of Nodes in Case 2
Laminar	703.1	684.4	1721	797
Standard k-ε	85.2	84.2	194	209
Renormalization Group Theory k-ε	141.7	134	317	336
SA (Vorticity based production)	112.8	102	279	787
SA (strain/vorticity based production)	135.2	211.4	348	1100
Reynolds Stress Modeling	85.1	85.6	677	1900

The transfer of heat in a data center is primarily by two methods: conduction or convection. Each occurs on different lengthscales. For example, conduction may occur at the sub-micron scale through a chip, while convection occurs within the cabinets containing electronic equipment and in the room that contains these cabinets. Therefore, a model that can accurately predict all of these processes requires at least six decades of lengthscales [13]. A mesh that contains sufficient control volumes to do so is literally impossible to handle at this point, based on the ability of even the most advanced computing platforms. Therefore, predictive CFD-HT models must be created either at the chip level, the rack level, or the room level in a data center environment – but not at multiple levels simultaneously.

In [3], a numerical case study was performed to predict the effect of different RFP data center parameters on the heat extraction by the CRAC units. A data center model was created using the software 'Flovent.' Each server rack was represented in this model as a single cubic block dissipating a uniformly-distributed heat load with a constant and uniform air flow rate. The CRAC unit model was also a cuboid block, but with a fixed

flow rate of 5.7 m^3/s and an outlet temperature of 15^oC. The CRAC units were sized based on the mean heat loads, which is how a data center facility would normally be designed. The efficiency study was based on the average inlet temperature to the CRAC unit. According to predictions by this numerical model, when the heat is dissipated non-uniformly, the CRAC units near areas of high heat loads must operate at higher than their capacity (which of course is impossible). This is evidence of the necessity to develop CFD-HT models to aid in designing a data center.

In [14], a CFD-HT model of a prototype data center was developed and compared to experiments taken at the facility. Each experimental rack was composed of four compartments that would each deliver a 0.283 m^3/s (600 CFM) flow rate (from three parallel fans) and a heat load ranging from 0 to 3,600 W. Each of these compartments was modeled as a "cuboid block," which was assigned a constant 0.283 m^3/s (600 CFM) flow rate and a uniformly-distributed heat load of either 0 or 3,600 W. Temperatures were measured at several locations around the room, and those were compared to temperatures predicted by the model. The average error between temperatures at these points ranged between 7% and 12%, depending on location in the vertical direction. Rack inlet temperatures were measured as well, and an average error of between 11% and 17% was found, depending on the rack row.

The previous two studies modeled each of the racks as a solid cuboid block, with constant flow rates and uniformly-distributed heat loads. By using such "black box" models, the physics of the system is lost. In real racks, the heat loads are not distributed evenly, and many "hot spots" will exist within the rack, which often have a significant negative impact on the equipment within. Furthermore, the actual geometries of the electronic equipment within a rack will lead to significant variations in temperatures and air velocities, not only inside the rack, but also at the exit of the rack, which will affect the room-level patterns. Therefore, it is necessary to come up with a method of characterizing the racks themselves.

1.4 Rack-Level CFD-HT Modeling

Typically, the only dynamic control of a current data center is a response to the inlet air temperature at the return of the CRAC unit. Mainly, if the air entering that unit is warmer than the set point, then the chilled water valve allows more water to pass in order to deliver colder air to the entire room. This would be an adequate solution only if the main goal was to cool the space that contains the electronic equipment, rather than the equipment itself. Therefore, since most current data centers do not have the ability to dynamically redistribute cold air to local hot spots, it is necessary to place the racks in the room according to the amount of heat loads that they produce and the estimated amount of cold air that each of the racks requires.

The proper delivery of cold air to specific locations of data centers has been shown to be a difficult task. In a recent study by [15], it was found that an inadequate supply of cold air to racks can result in high inlet temperature rises from the bottom to the top of the hardware due to a recirculation of air in the room. In fact, they found a temperature rise of $12^{o}C$ from the porous tile to the inlet of the top of the rack, which could be harmful to the computer equipment at this height. The study noted that this phenomenon could be avoided if modifications were made to the grille on the door of the rack itself.

The previous study is further evidence of the fact that a rack in a data center thermal model should not merely be modeled as a black box with a constant heat load and flow rate. In reality, the performance of a rack depends on the often intricate details of the equipment inside. Therefore, it would be more beneficial to come up with better approximations than previously used.

Unfortunately, a complete and detailed thermal model of a cabinet still requires at least five decades of lengthscales [16]. A real rack is an interactive entity, and it cannot be represented as a passive and uniform black box. For one, the purpose of the fans that are mounted in front of the server equipment within racks is to facilitate the movement of

air over the components when needed. The racks are not uniform, and this is often done for a reason.

Another study [13] noted that servers could be strategically arranged within a rack itself. Three different strategies were listed. Number one, servers with high heat loads could be placed near the bottom of the rack in order to draw the majority of the cold air. The disadvantage to this, however, would be that the hot exhaust from the bottom of this rack would "thermally pollute" the equipment above. Number two, it was suggested that the high-heat servers be placed at the top to avoid passing heat to equipment above. This may not work, though, if the inlet temperature is too high at the top of the rack to be able to adequately cool that equipment. The third strategy would be to spread out the heat as much as possible to minimize high power densities. A very simple CFD-HT model of a rack was developed to determine which strategy would work best. Heat-generating components were modeled as solid blocks, and many detailed components – such as heat sinks and heat spreaders – were omitted. It was found using this model that spreading the heat as evenly as possible would result in the best thermal performance. It is important to note, however, that the modeled rack was not actually a physical entity, and therefore the model could not be validated experimentally.

In [16], a reduced-order model of a rack was created using observations of CFD-HT results (See Figure 4). The air in this particular rack is drawn through an internal plenum from the bottom, and it exits through the top. Heat is transferred by convection to a thermoelectric cooler (TEC), and the heat exchange on the bay side is done by a fan, which allows air in the bay to circulate past the heat exchanger and over the components and heat sinks in the bay. The CFD-HT model was developed for a single bay of the rack and its associate plenum part – rather than the entire rack. This was done because a model of the entire rack was not feasible given the required number of volumes in the mesh.

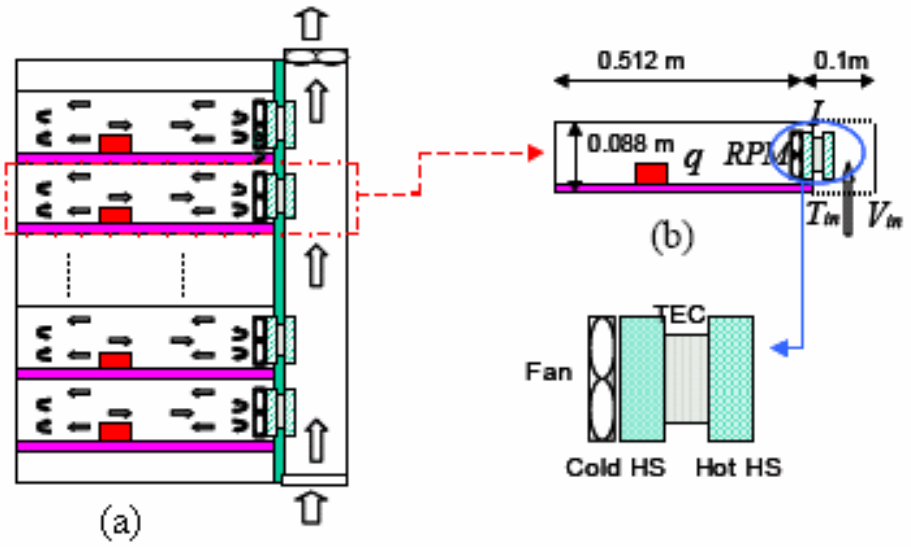

Figure 4: (a) Cabinet Considered and (b) a Single [16]

Of course, to be able to model each enclosure independently of the surrounding ones, it must be assumed that a negligible amount of heat passes from one bay to another. Compact models were developed for each of the components, and the proper orthogonal decomposition (POD) method – a technique for using observations of velocity and temperature fields to develop models that do not require CFD-HT simulations – was used to construct a reduced-order model of the enclosure subsystem. The POD model was then compared to the CFD-HT model of the enclosure, and it was estimated that the POD model could replace a CFD-HT one – within about 10% error. Again, it is important to point out that neither the CFD-HT model nor the POD model were validated experimentally.

In [17], an experimental study was performed to determine whether it is possible to accurately model an air-cooled electronic enclosure using CFD-HT. It was noted in this study that there are many complex structures in such a cabinet that inhibit the capability of CFD-HT to come up with accurate predictions. For example, it is difficult to predict flow patterns over components downstream of fans (but not upstream of fans). Also, it is difficult to capture complex grille exit flow patterns that exist due to induced wakes and approaching swirling flow upstream of grilles. Lastly, it was noted that

components within such a structure often cause very complex flow conditions to develop, such as separations and wakes. These flow features greatly affect the pressure drops and the convection heat transfer coefficients. This would make the prediction of both very difficult. Also, according to the authors of this study, turbulence models must always be introduced, and current turbulence models often lead to complicated flow patterns like swirls and re-circulating flows that lead to large errors between models and experimental results. This study also tested the accuracy of the different turbulence models developed for flow over components. The authors found that all of the turbulence models over-predicted the deceleration of the flow over the components. Further, it was found that the predicted Nusselt numbers of the CFD-HT models did not agree with those found experimentally.

In [18], a CFD-HT model of a simpler geometry was created: an array of printed circuit boards (PCB's) through which air is forced by axial fans. Due to the infeasible amount of grid cells required to model details such as heat sinks and grilles in a system-level model, these components were treated as solid blocks with air flow resistances. The resistance characteristics were found by creating detailed CFD-HT models of each component and finding the pressure drops as functions of the inlet velocity. The purpose of the study was to determine the flow rates through each of the passages between PCB's. The simulations were compared to experimental flow rate measurements, and good agreement was found. This could probably be attested to the fact that the geometry is somewhat simple – an array of boards through which air is forced.

1.4.1 Methods of Representing Heat Sinks in Rack-Level CFD-HT Models

In system-level models, it is impossible to model components with small relative dimensions in enough detail. Heat sinks are a good example, as the thicknesses of the fins themselves and of the spaces between the fins require a large mesh to capture the details

of the different heat transfer modes; thus, compact models of these components must be used in system-level CFD-HT simulations.

One way to model an array of fins (such as a heat sink) is by assigning an equivalent heat transfer coefficient to the boundary where the heat sink is attached. These coefficients can be estimated by analytical or empirical means, such as those described in [19]. For the approach to be applicable, though, the exact geometry must match those found in the literature. Also, if detailed flow models are required, one must seek some way of representing the flow resistance of the heat sinks, which this type of model does not include. In [20], the pressure drop across a heat sink was derived from theoretical heat sink models. Three different analytical models were discussed. Equations 1 (1.1) and 2 (1.2) were derived from the Flemings and Darcy pressure drop equations, and Equation 3 (1.3) was derived from a force balance on the heat sink [20]:

$$\Delta p = \left(\frac{f_{app} N(2HL + bL)}{HW} + K_c + K_e \right) \left(\frac{1}{2} \rho \upsilon_{ch}^2 \right) \tag{1.1}$$

$$\Delta p = \left(4 f_{app} x^+ + K_c + K_e \right) \left(\frac{1}{2} \rho \upsilon_{ch}^2 \right) \tag{1.2}$$

$$\Delta p = 4 \left(f_{app} x^+ + K_c + K_e \right) \left(\frac{1}{2} \rho \upsilon_{ch}^2 \right) \tag{1.3}$$

In these equations, f_{app} is the apparent friction. N is the number of fins. H is the fin height, and L is the fin length. Also, b is the width of the heat sink gap, and W is the total width of the heat sink. υ_{ch} is the heat sink channel velocity. K_c and K_e are the coefficients of contraction and expansion, respectively. Lastly, x^+ is the hydrodynamic entry length. Also, a detailed CFD-HT model of a heat sink was developed using the commercial software package 'Flowtherm.' Pressure drops were found as functions of the airflow using each of the four models. Experiments were then performed on the actual heat sink, and the results were compared.

It was found that there was not good agreement between the analytical models and the experimental data. Equations 2 and 3 both under-predicted the pressure drop by approximately 86%. Equation 1 under-predicted the experimental pressure drops by approximately 29%. The detailed CFD-HT model, on the other hand, showed good agreement with the experimental data.

Since a detailed heat sink model requires too large of a mesh to be implemented in a system-level CFD-HT simulation, however, many designers represent them as flow-resistance black boxes, such as in [21], [22] and [23]. The heat sink is geometrically modeled as a cuboid block, and one must input the relationship between the flow rate and the pressure drop across the heat sink. Also, an effective conductivity must be applied. This is known as a porous media model, and it will be discussed later in more detail.

The inputs for the porous media model can be found experimentally or by using a detailed CFD-HT model of the heat sink, like the one discussed previously. In [22], a porous media model of a heat sink was compared to a detailed CFD-HT model. Overall, good agreement was found for both pressures and temperatures between the two models.

In [24], the shortcomings of a porous media model are listed. Since the fins are not present in the porous media model, channel flow is not well-represented, but rather a "plug flow" exists. Also, the authors note that the large differences in the outlet velocity profiles between the actual geometry and the porous block model can often lead to large pressure-drop discrepancies. The pressure drop in reality will be dependent on the distinct flow patterns caused by the characteristics of the specific fin geometries. Despite these issues, however, the authors note that it is still possible to create an accurate model using a porous media, depending on the situation.

1.4.2 Methods of Representing Fans in a Rack-Level CFD-HT Model

Because of the complex geometries associated with fans (See Figure 5a), accurate simulation models require complicated meshing schemes with large numbers of mesh

volumes. Therefore, for system-level CFD-HT modeling "macro" models of fans are required [25]. According to [26], fans are often modeled in large systems as simple rectangular faces with a given pressure-jump-versus-flow-rate relationship. The authors note that such a model would be improved by adding the hub, and they present a simple model (See Figure 5b). Figure 6 shows a typical performance curve for a fan.

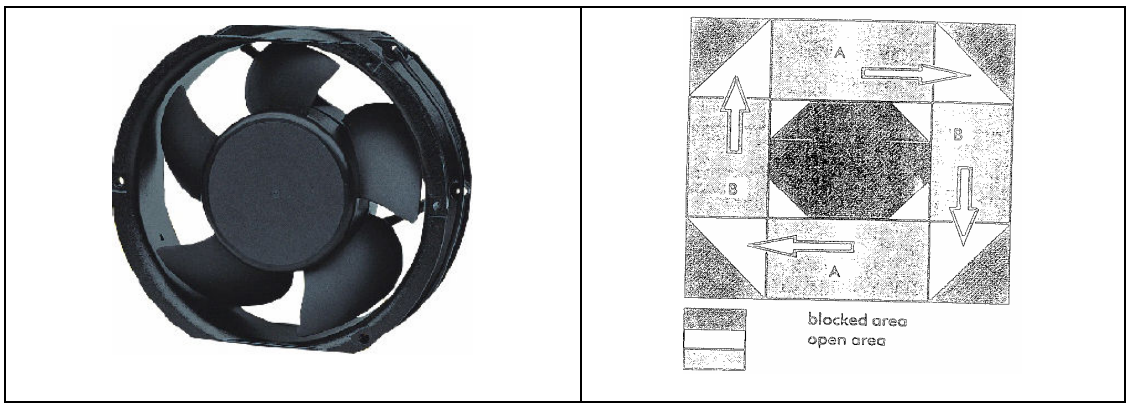

Figure 5: Typical (a) Electronics Cooling Fan (b) CFD Fan Model [26]

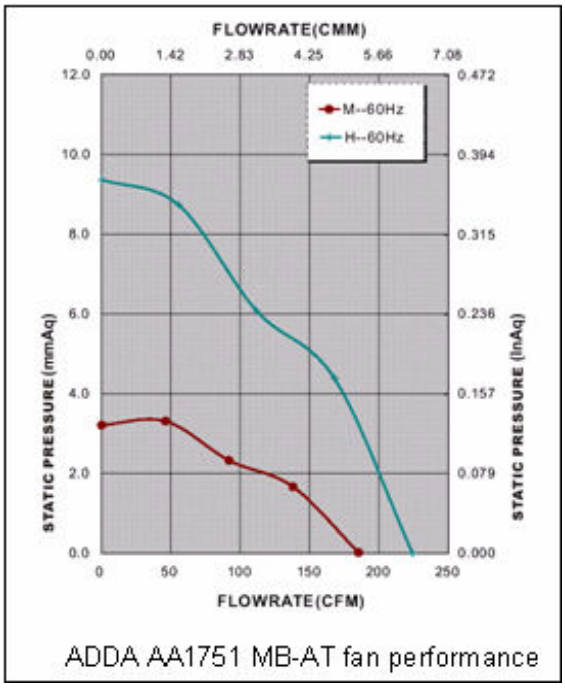

Figure 6: Typical Fan Curve

It is easy to implement simple fan models with basic fan curves, but unfortunately, that may not be enough to accurately predict all of the flow patterns. For example, it was found in [27] that while simple models of fans involving only fan

performance curves can provide accurate results when air is being pulled over components, particular attention must be paid to fan swirl when heat sinks and packages are located downstream of the fans. It was found that the presence of swirl always enhanced the cooling.

Unfortunately, the task of predicting the swirl of a particular fan is a difficult one. The fan swirl may be broken up into two components: the axial and the tangential velocity components. In [17], a detailed CFD-HT model of a fan was developed and compared to experimental results. Particular attention was paid to the prediction of fan swirl by the CFD-HT models. It was found that even the most detailed fan models cannot accurately predict the swirl velocity of a fan. The models anticipate approximately constant radial and tangential velocities, whereas the experiments prove otherwise.

1.5 The Focus of this Study

Based on the above discussion, it is clear that a CFD-HT model can provide a designer with an invaluable tool in predicting the temperature and velocity patterns in a data center facility. This will allow one to place most of the equipment in a facility more effectively. In order to create an accurate CFD-HT model of an electronic enclosure, however, many approximations must be made. This is done not only in order to simplify the model development process, but also because it is infeasible to run extremely detailed simulations using current technologies. Each assumption made in a design process can lead to discrepancies between the CFD-HT results and experimental observations; therefore, each assumption must be experimentally tested for validity. This thesis will present an effort to produce such an experimentally-validated CFD-HT model of an electronics enclosure.

CHAPTER 2

EXPERIMENTAL TOOLS AND METHODS

As previously discussed, there are essentially two ways of making rack-level temperature predictions. One is to use experimental observations to create empirical relationships. In this method, the physics is usually ignored, and it becomes difficult for one to apply the model to a specific geometry that is different than the one used to develop that model. The other method is to use CFD-HT analysis to model a rack (or a portion of a rack). Unfortunately, it is currently infeasible and in most cases impossible to create a CFD-HT model that is detailed enough to capture many key details. Therefore, much effort has been devoted to creating so-called "compact" models of electronics enclosures. Certain components with detailed geometries – e.g. fans and heat – are simplified in order to decrease the mesh size and hence reduce the computational demand.

In previous studies, much of the validation for these CFD-HT models has involved a comparison between the compact versions of component models and detailed ones, but rarely experiments. It is also difficult to know a priori whether a compact model of a component will make the system-level model behave differently than it does in reality. Therefore, in order to truly test the validity of a compact model, experimental results should be used as the basis of comparison, rather than detailed component modeling.

This chapter will introduce the server simulators, which were used to develop the compact CFD-HT model of an electronics enclosure. The advantage of a server simulator – rather than an actual server – is the ability to better quantify and control the parameters of interest. Most notably, one may choose to dissipate a known heat load at a chosen air flow rate. Generally, neither of these values is known precisely for a real server. Also,

real computer equipment is unsteady over time. Therefore, a server simulator can be used to more effectively assess data center equipment models.

This chapter will also describe the measurement tools used and the experimental methods applied. Experiments were used not only to validate the CFD-HT model, but also to provide empirical inputs, such as fan performance curves and component pressure drop characteristics.

2.1 Basis for the Experimentally-Validated Compact CFD-HT Model

2.1.1 Server Simulator Basic Description and Dimensions

Each server simulator is 43.2 cm (17 in.) wide and 44.5 cm (17.5 in. or 10 U) in height. The depth of the simulator is approximately 69 cm (27.125 in.). Figure 7 shows a front and rear isometric view of a server simulator (in (a) and (b), respectively).

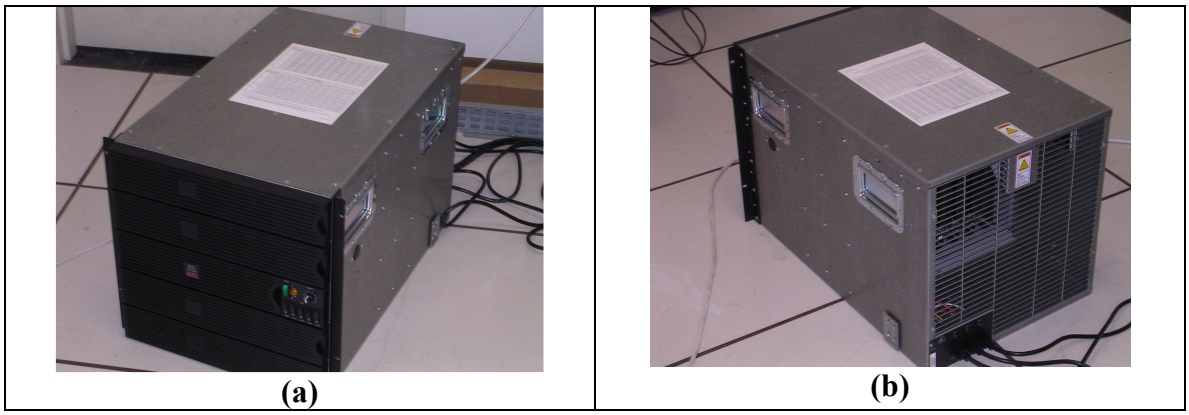

(a) (b)

Figure 7: APC Server Simulator (a) Front and (b)

Figure 8 is a photograph of the server simulator taken overhead, with the top of the cabinet removed. The basic components are labeled in the figure and described in the following pages.

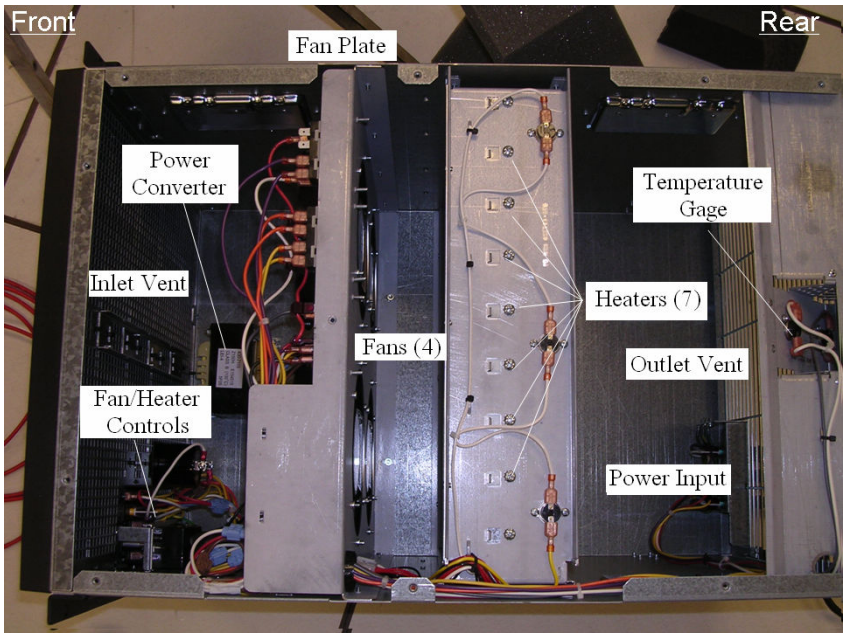

Figure 8: Overhead View of Server Simulator

Basically, air is pulled through the inlet grille by four parallel fans. The air is then forced over seven parallel finned heaters and through the outlet.

Inlet Grille

The inlet grille is composed of essentially two different layers (See Figure 9).

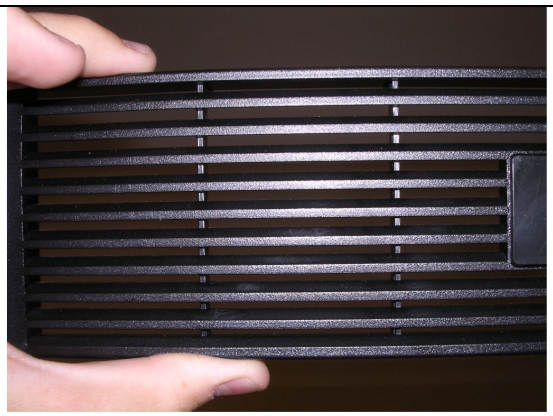

(a) (b)

Figure 9: Inlet Grille (a) Front Plastic Grille and (b) Metal Grid

The front plastic grille is approximately 19 mm (0.75 in.) thick. Each opening is about 3.175 mm (0.125 in.) high. This plastic part has a porosity (open area per total area) of approximately 37%. The thin metal grille is directly attached to the back of the plastic part and is then screwed to the front of the server simulator. The openings of the metal grill are 6.35 mm (0.25 in.) square, and the porosity of the metal grid is approximately 53%.

Fans

A fan plate is located 25.4 cm (10 in.) from the front of the server simulator. Figure 10 is a photograph of the fan plate taken from the front of the server simulator, with the inlet grille removed. The outlet of each of the four fans is mounted to the plate, and the fans are centered on the plate and spaced 5.1 cm (2 in.) apart. Each fan has an outer diameter of 16.8 cm (6.625 in.) with an 8.2 cm (3.25 in.) diameter hub in the center. The fans are cylindrical, with a depth of 5.1 cm (2 in.).

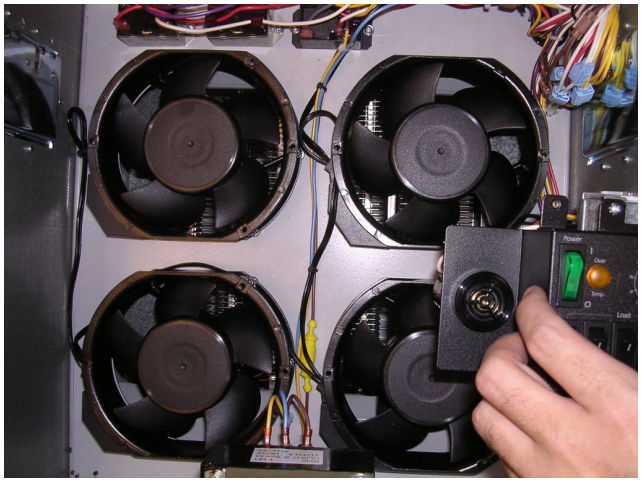

Figure 10: Fan Plate

Each fan is the same: an AC fan, model number AA1751HB-AT – manufactured by ADDA Corporation. The manufacturer provides data for the fan with a power input of 115 V and 60 Hz. According to ADDA, the fan rotates at 3000 RPM at that speed and has a maximum static pressure of 93.16 Pa (0.374 in. H_2O) at shutoff flow. Also, a maximum air flow rate of 0.103 m^3/s (218 CFM) is estimated. Figure 11 gives the fan curve provided by ADDA Corporation.

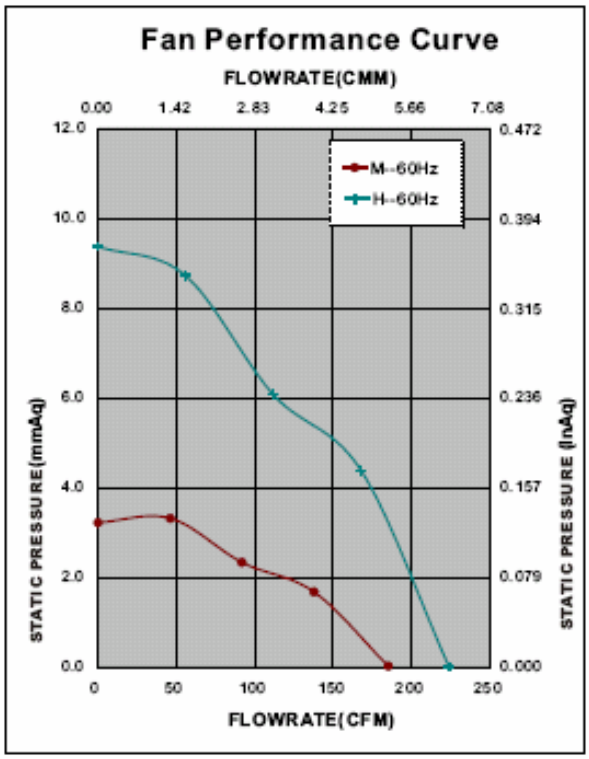

Figure 11: Fan Curve Provided by the Manufacturer

The curve labeled “H” in the above figure is the one hypothesized, whereas the curve labeled “M” was measured by the manufacturer.

Heaters

The space that contains the heaters begins 7.62 cm (3 in.) beyond the fan plate, or 33 cm (13 in.) from the front of the server simulator. The entrance to the heater space is a 31.8 cm (12.5 in.) square opening that begins 8.3 cm (3.25 in.) from the bottom of the simulator. The space itself is 40 cm (15.75 in.) high, 40.6 cm (16 in.) wide, and 10.2 cm (4 in.) deep. There are seven heaters, which are centered in the heater space (so the center of the heaters is located 38.1 cm (15 in.) from the front of the server simulator). Figure 12 shows the heater space.

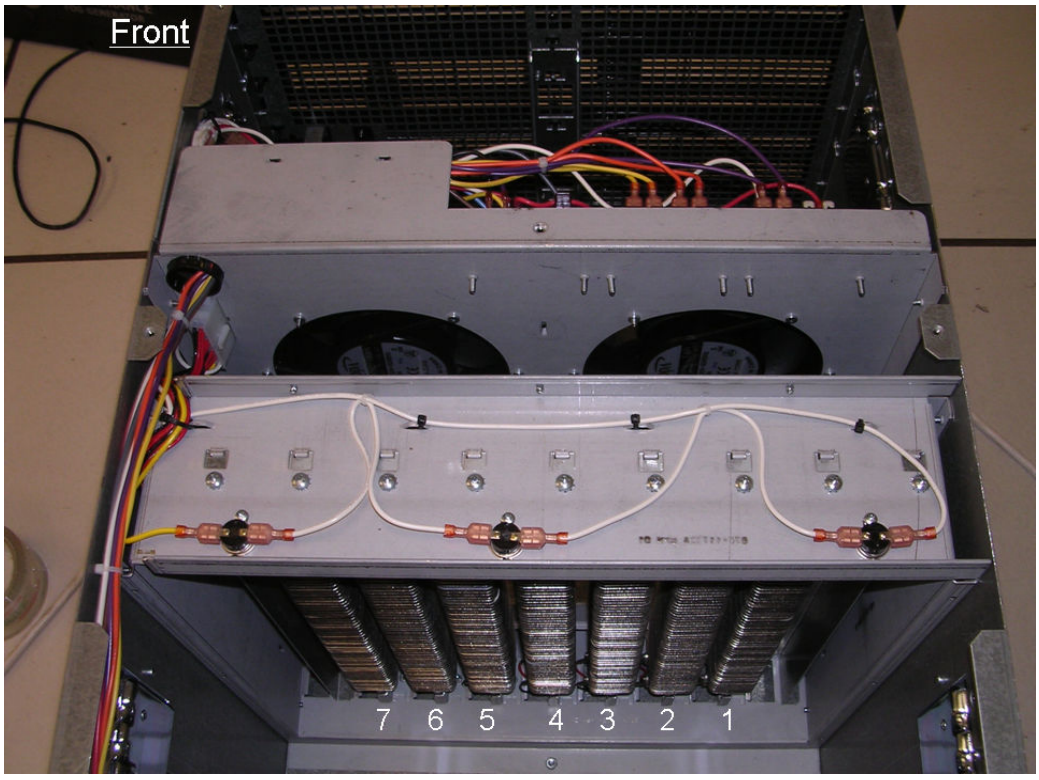

Figure 12: Overhead View of the Heater Space

The heaters shall be referred to by their numbers – 1 through 7 – beginning with the one closest to the left side of the server simulator. Figure 13 is a close-up photograph of two of the heaters.

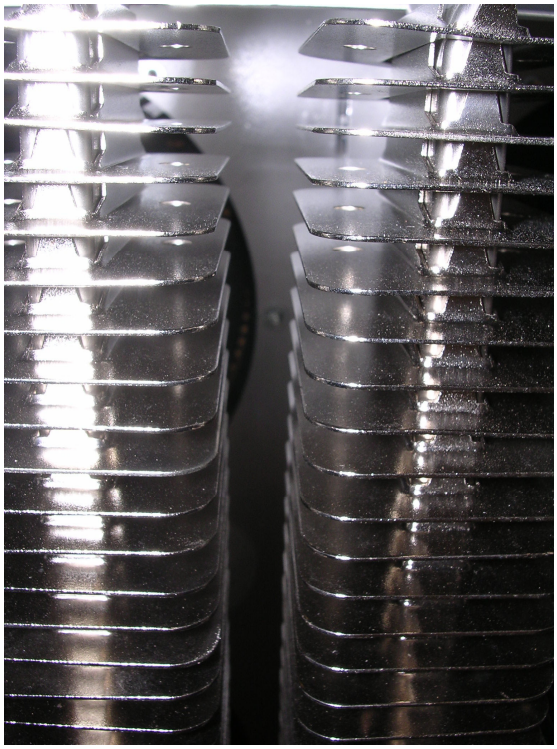

Figure 13: Heaters and Fins

Each heater measures 6.35 mm (0.25 in.) wide and 4.13 cm (1.625 in.) deep. Each of the heaters is surrounding by an array of 56 fins. Each of the fins is 3.5 cm (1.375 in.) wide, 5.1 cm (2 in.) deep, and 0.635 mm (0.025 in.) thick. The fins are each spaced about 5.1 mm (0.2 in.) apart. There is approximately 9.5 mm (0.375 in.) between the fins of one heater to the fins of another (the centers of the heaters are 1.45 cm (1.75 in.) apart).

The heat is generated by an electrical current that passes through each heater. The heater's sheath is made of stainless steel, and the fins are made of nickel-plated steel.

Server Simulator Controls

A dial on the front of each server simulator allows one to vary the rotational speed of the fans. Also, switches located next to the fan speed dial allow one to control the total amount of heat dissipated. Figure 14 shows the set of controls.

Figure 14: Server Simulator Controls

It is important to note that the fan dial knob rotates fluidly. In other words, the knob does not click into place for each dial setting, and one must judge the particular setting number by sight alone. The manufacturer (APC) provides a table with the estimated airflow through the server simulator for each dial setting. Table 2 gives the manufacturer's estimated airflow values for a 208V 60Hz power source. It should be noted here that the power comes in to the experimental facility from a 208V-3Phase branch circuit.

Table 2: Airflow vs. Dial Settings as Provided by the Manufacturer

Dial Setting	Airflow m^3/s (CFM)	Dial Setting	Airflow m^3/s (CFM)
1	0.09439 (200)	6	0.1510 (320)
2	0.1015 (215)	7	0.1793 (380)
3	0.1085 (230)	8	0.2265 (480)
4	0.1156 (245)	9	0.2784 (590)
5	0.1321 (280)	10	0.3068 (650)

The switches control how much overall heat is dissipated. The heat can be increased in multiples of 250 W up to a possible 5750 W. Figure 15 shows the amounts of heat dissipated by each heater.

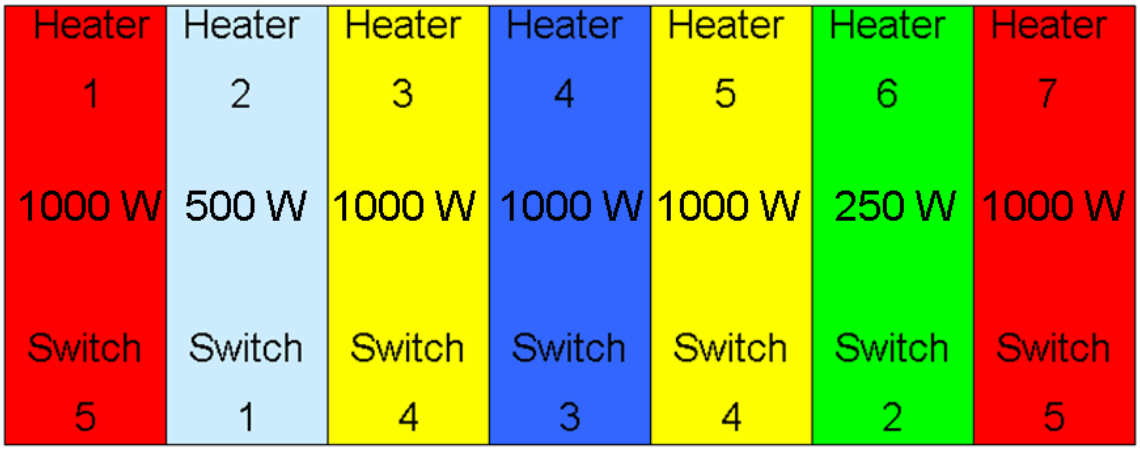

Figure 15: Heat Loads of Each Heater

The heaters are numbered from left to right of the server simulator – facing the front. Heaters with similar colors in the above figure are turned on and off by the same switch. Notice that the heat is generated symmetrically except when either heater 2 or heater 6 is turned on.

Miscellaneous Server Simulator Dimensions

The outlet grille is approximately 88% porous. A 7.6 cm (3 in.) temperature gage is located at the top center of the outlet. Its purpose is to sound an alarm if the exit temperature is too high. The power box is located in the bottom left (if facing the outlet) of the outlet grille. It measures 16 cm (6.3125 in.) wide and 8.9 cm (3.5 in.) high. The power converter is located about 6.4 cm (2.5 in.) from the front of the unit. The converter is 10.2 cm (4 in.) wide, 8.9 cm (3.5 in.) high, and 7.6 cm (3 in.) deep.

2.1.2 Rack Dimensions

Shelves are mounted in a rack to allow one to stack up to four server simulators vertically. This will create a 40U rack. In other words, this rack could contain as many as forty blade servers. Figure 16 shows the server simulators stacked in a rack enclosure.

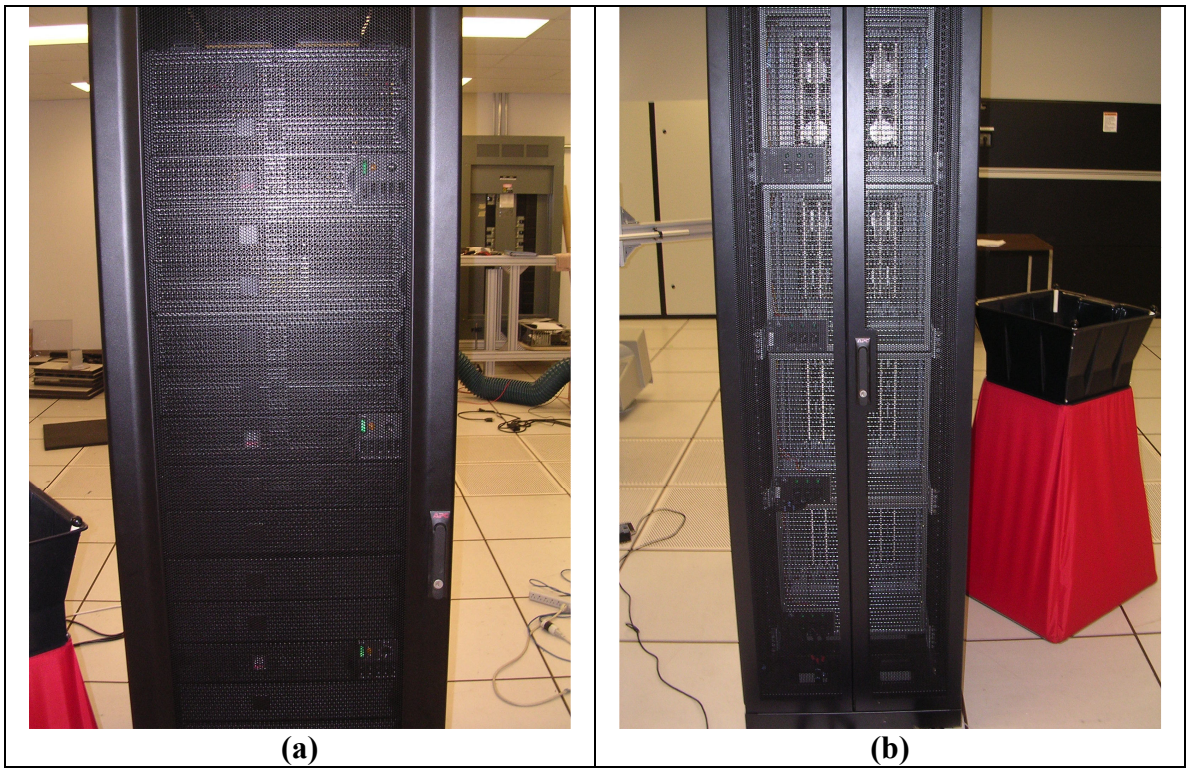

Figure 16: Rack (a) Front and (b) Rear

The rack is 58.4 cm (23 in.) wide and 1.067 m (3 ft 6 in.) deep. The total external height of the rack is approximately 2.134 m (7 ft.), but the internal space begins approximately 14 cm (5.5 in.) off the ground. The server simulators are mounted such that a 7.3 cm (2.875 in.) gap exists between the inlet grille of the rack and the inlet of the simulator. This creates a 30.5 cm (1 ft) gap between the outlets of the server simulators and the outlet grilles of the rack. Refer to Figure 17 to visualize the exit plenum and server simulator mounts.

Figure 17: Server Simulator Mount in Rack

The rack grilles allow the passage of air from the front of the rack to the back, while protecting the equipment from dust and other particulates in the room. Both the inlet and the outlet grilles consist of circular openings that measure 6.35 mm (0.25 in.) in diameter. The porosity of the rack grilles is approximately 60%.

2.1.3 Experimental Facility

All experimental data were taken at the Consortium for Energy Efficient Thermal Management's (CEETHERM's) data center laboratory at the Georgia Institute of Technology. Figure 18 shows the data center laboratory. The 104 m^2 (1120 ft^2) facility houses four Computer Room Air Conditioning (CRAC) units. There are two upflow CRAC units (one APC and one Liebert) that each have a capacity of approximately 75 kW and can produce a flow rate of about 4.248 m^3/s (9,000 CFM). There are also two downflow units (one APC and one Liebert), and they each have a nominal cooling capacity of approximately 90 kW and an air flow rate of about 5.663 m^3/s (12,000 CFM). A 450 kW capacity chiller, along with a 0.01136 m^3/s (180 GPM) pump, delivers chilled water to the CRAC units.

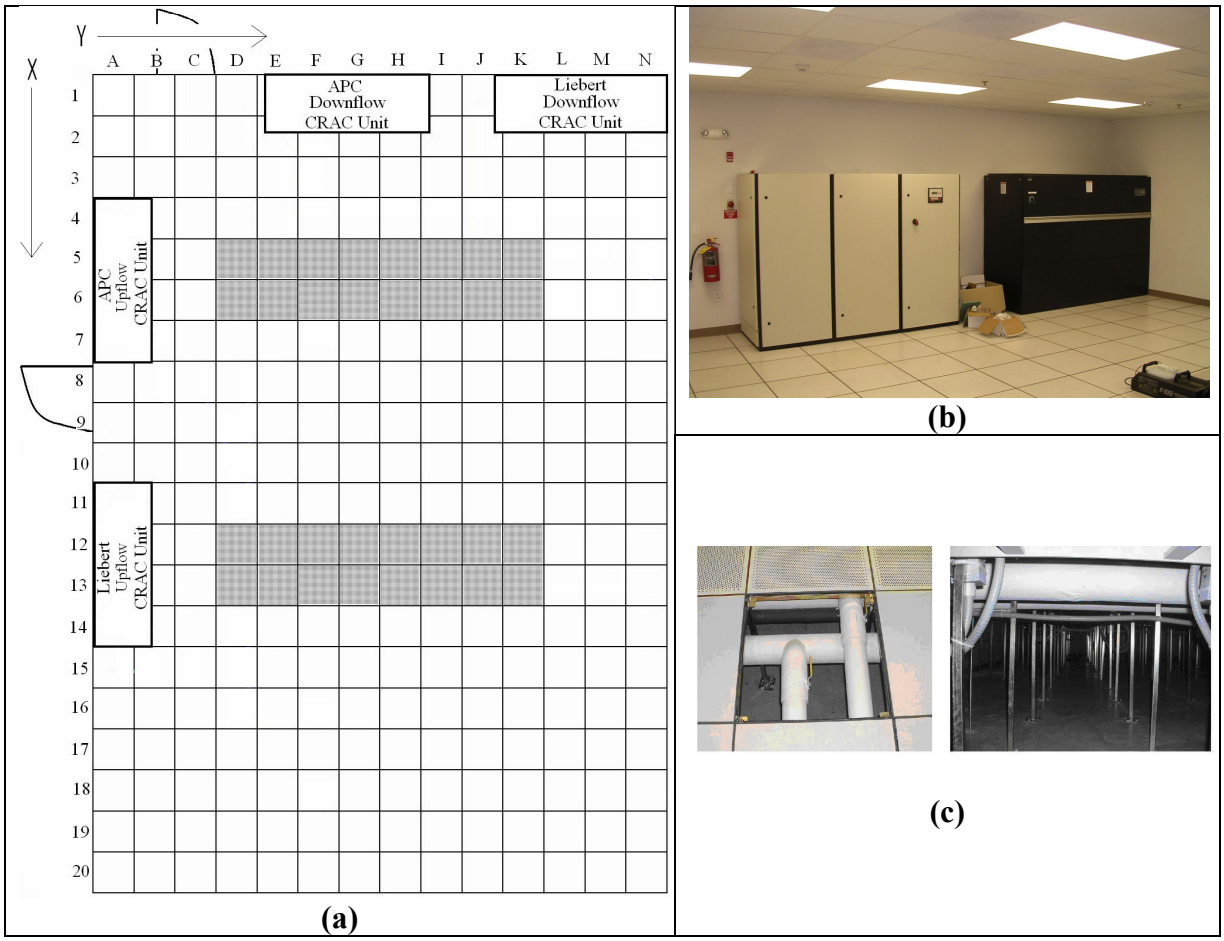

Figure 18: (a) Data Center Facility (b) Downflow CRAC Units (c) Plenum

The APC units are typical CRAC units in that they employ a blower with a constant flow rate. The APC units measure the air temperature at the CRAC return, and a valve controls the amount of chilled water to the cooling coils accordingly (to vary the temperature of the air that is output through the plenum to the room). The Liebert units, on the other hand, each employ a variable-frequency drive (VFD). This VFD drive allows the CRAC unit to control the rotational speed of the AC motor that powers the blower; therefore, the Liebert units can control both the temperature of the outlet air (by varying the chilled water amount) and the flow rate (by varying the blower speed). This added control is creates a more stable temperature environment in the room. This is important to note because one major basis of comparison between the CFD-HT model of the server simulator and the actual server simulator was the outlet temperature map, and it was

assumed in the model that the inlet temperature of the server simulator was uniform. The inlet temperature of the model was set at 22.22°C (72°F), which was based on the set point of the Liebert unit.

When the server simulator outlet temperatures were measured, the Liebert downflow CRAC unit was the only one running, and the room was almost void of any other heat-generating units. The server simulator was placed at a location in the room that was far away from porous tiles so that large variations in temperature at the inlet would not occur. It was observed that under these conditions, the temperature of the room was approximately steady, ranging from about 21.83°C to 22.61°C (71.2°F to 72.7°F).

2.2 Measurement Tools and Methods

2.2.1 Temperature Measurements

As mentioned previously, the outlet temperature map of the server simulator enclosure and of the rack served as a major basis of comparison between the compact CFD-HT model and the actual unit. There were a couple of different methods of measuring the outlet temperatures of the server simulator, but all methods used Omega Type T thermocouple wire. Both the copper and the constantan wires had diameters of 0.127 mm (0.005 in.). Figure 19 shows the predicted error of a Type T thermocouple wire over a range of measured temperatures.

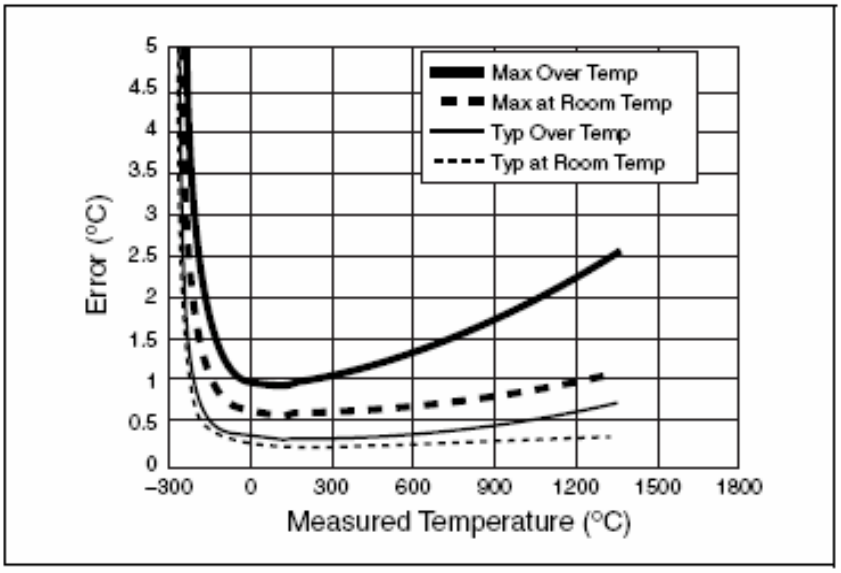

Figure 19: Expected Errors of Type-T Thermocouple Wires [28]

The server simulator outlet temperatures ranged from about 22°C to about 95°C, so the error is typically expected to be around 0.4-0.5°C (0.72-0.9°F) according to the previous figure. It is important to note that the previous figure gives the expected error of just the wire itself.

There is also some uncertainty involved with the data acquisition system. All temperature measurements were taken using National Instruments FieldPoint 8-Channel Thermocouple Input Modules, model FP-TC-120. The modules were attached to a Fieldpoint Network Interface, model FP-1601. Figure 20 shows the FP-1601 and FP-TC-120 modules. Although only one FP-TC-120 module is shown attached to the FP-1601 unit in the picture, it is possible to connect multiple units together to provide many inputs. All connected modules may be powered by a single 12V DC power source that is wired to the FP-1601 module.

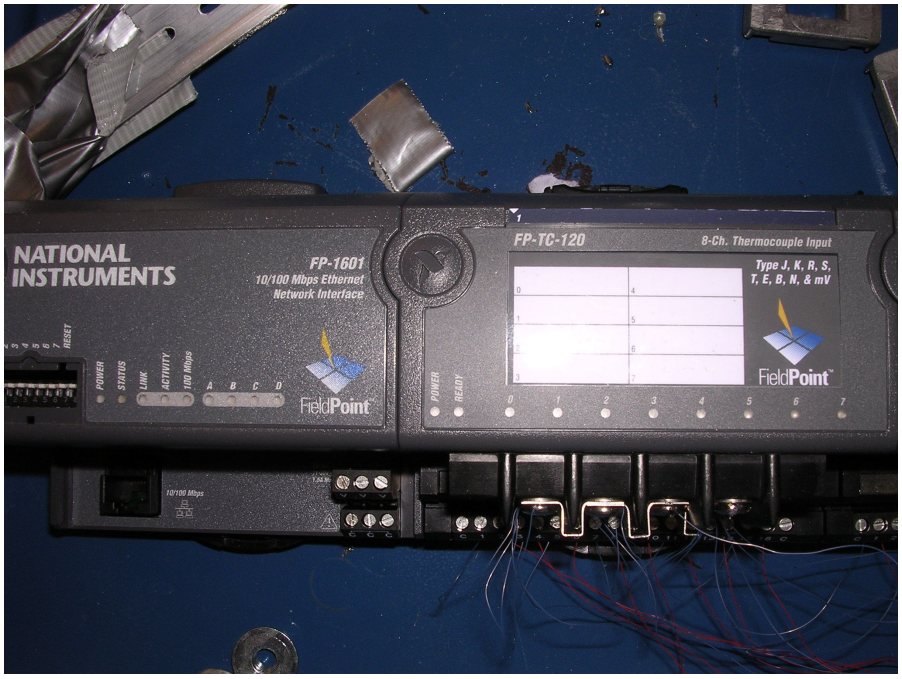

Figure 20: FP-1601 and FP-TC-120 Data Acquisition Modules

As can be seen in the above photograph, the FP-TC-120 module has eight input channels, which are labeled 0-7. All eight of these channels share a common ground reference, and this reference is isolated to that module (so other modules are not connected to the same reference ground). Each of the channels is filtered by the module and is sampled by a 16-bit analog-to-digital converter (ADC).

The module can output either voltage or temperature. When temperature is output by the module, a cold-junction compensation is performed. The module itself has a built-in temperature-measuring element in the terminal bases and connecting blocks. The module uses the temperature data from these elements to compensate for the cold junctions. This method assumes that the base itself is isothermal (constant temperature) throughout, and the temperature of the thermocouples is then assumed to be a default function of the input voltage. All measurements were taken using National Instruments' **Lab**oratory **V**irtual **I**nstrumentation **E**ngineering **W**orkbench (Labview).

According to the manufacturer of the modules, [28], any errors in the data acquisition system can be attributed to gain and offset errors, differential and integral

nonlinearity, quantization errors, noise errors, errors in linearization algorithms, and errors in the cold-junction temperature measurements. The latter may be a significant portion of the error, especially due to any thermal gradients that may exist within the modules themselves. In order to estimate the error that comes from the presence of a thermal gradient, the manufacturer recommends the following procedure: When a particular unit is connected to other units, note the heat dissipated by the connected units. Take the larger amount (between the two units) of heat dissipated, and divide it by 20 W/^{o}C. For example, if a module is between an FP-1601 communication module, which requires 4.5 W of power, and another FP-TC-120 module, which requires 0.35 W of power, one would estimate the maximum thermal gradient error by dividing 4.5 W by 20 W/^{o}C. This would result in an error of 0.225^{o}C. This is the largest possible thermal gradient error that an FP-TC-120 module would have, given the measurement method.

The cold-junction accuracy is listed by the manufacturer as 0.15^{o}C, and the gain error is estimated to be between 0.01 and 0.03%. So, if one sums the maximum thermocouple uncertainty (0.5^{o}C), the cold-junction uncertainty (0.225^{o}C), and the estimated thermal-gradient uncertainty (0.15^{o}C), the uncertainty of the temperature data acquisition system is expected to be around 0.875^{o}C.

To verify that the FP-TC-120 modules (and specifically the cold-junction compensations) were correctly predicting the temperatures, a calibration was performed for thermocouples attached to 17 channels. Each of the 17 thermocouples was placed in a bath of water within a thermocouple calibrator. The calibrator was used to vary the water temperature, which was indicated by a digital display of the temperature, which was measured by a Resistance Temperature Detector (RTD). The maximum temperature difference between the FP-TC-120 and the temperature reported by the thermocouple calibrator was found to be only 0.37^{o}C, which is within the expected error of the Type T thermocouple wire; therefore, it is impossible to know the source of the discrepancy – especially because the differences in temperatures were not systematic (in other words,

the thermocouples did not consistently over or under-predict the temperatures). This difference can be attributed not only to the thermocouple wire and the data acquisition modules, but also to the calibrator itself, as the digital output on the calibrator had a resolution of only 0.1^{o}C. Appendix D has more information about the calibration of thermocouples, along with a representative calibration curve.

Temperature Measurement Methods

Two different temperature-measurement systems were developed for taking both server simulator and rack outlet temperatures. Detailed temperature maps would require many data points, and an entire rack could not be covered in thermocouple wires. Therefore, it was necessary to create a mobile system for thermal mapping – one that would be detailed enough to accurately map the outlet temperatures, but would also not be a significant flow obstruction, which would alter both the velocity and the temperature patterns.

Initial server simulator outlet temperature measurements were made with a five-by-five grid of thermocouple wires. A rectangular metal frame was constructed to contain this grid. Notches were cut at every inch of the metal grid, and a line was tied across the notches to form a grid of wire. The ends of the thermocouples were then glued at the intersection of these lines. This grid would allow a coarse temperature map of the entire server simulator outlet to be obtained at different points of time in order to study the transient behavior of the unit. Figure 21 gives the x and y position of each of the thermocouples of this rough 5-by-5 grid, with the origin at the middle of the server simulator outlet.

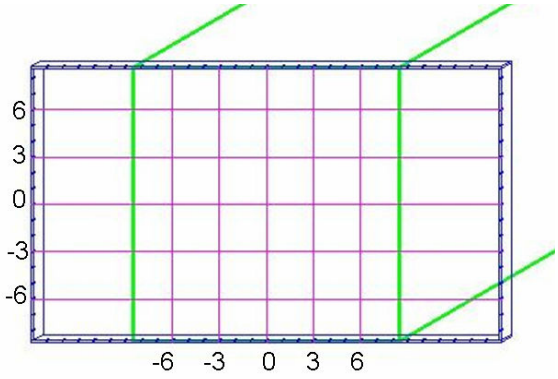

Figure 21: Rough Grid Thermocouple Locations

In order to get more detailed temperature measurements of the server simulator outlet, seventeen thermocouple wires were attached (one every 2.54 cm (1 in.)) to a single vertical strand of the wire. Figure 22 is a photograph of this assembly.

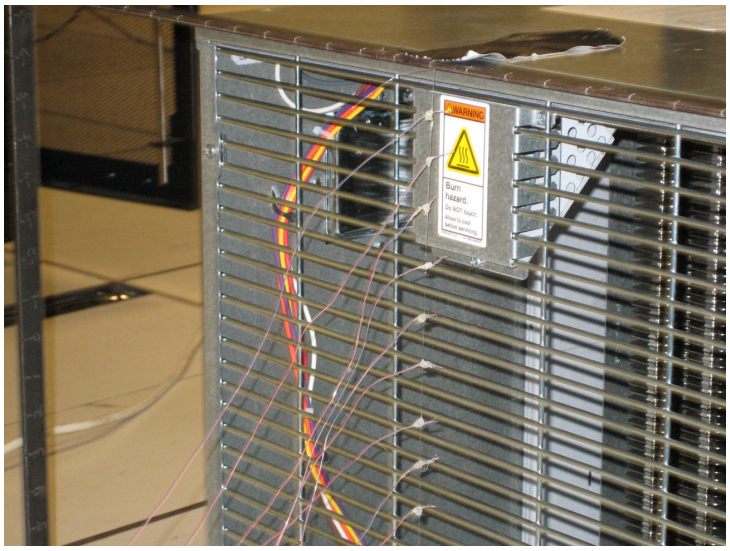

Figure 22: Vertical Row of Thermocouple Wires

The vertical row of 17 thermocouples was traversed horizontally – every one inch – to seventeen horizontal positions. Each row of temperatures was collected for two minutes, and the temperature values at each point were then averaged. This created a temperature map of the server simulator outlet from 289 data points.

To improve upon this temperature-measurement design, a smaller frame was built (5.1 cm by 61 cm). Notches were cut at the middle of the vertical piece and at every 2.54

cm (1 in.) along the 61 cm (24 in.) piece. Instead of creating a grid using line, the grid was made of thermocouple wire itself. A single copper wire was strung horizontally along the frame and then wired to the ground slots on the data acquisition unit. The insulation sheathe was removed at every inch along the wire within the frame. Twenty-three constantan wires were then soldered at these exposed points along the single copper wire, and the twenty-three constantan wires were then wired to different channels of the data acquisition module. Each row of temperatures was taken over a two-minute interval, and again an average temperature was found at each point. The horizontal row was attached to a traverse so that temperatures could be taken at 17 vertical locations (one every inch) for each server simulator. This again created a data map of 289 points. Figure 23 shows the thermocouple row setup.

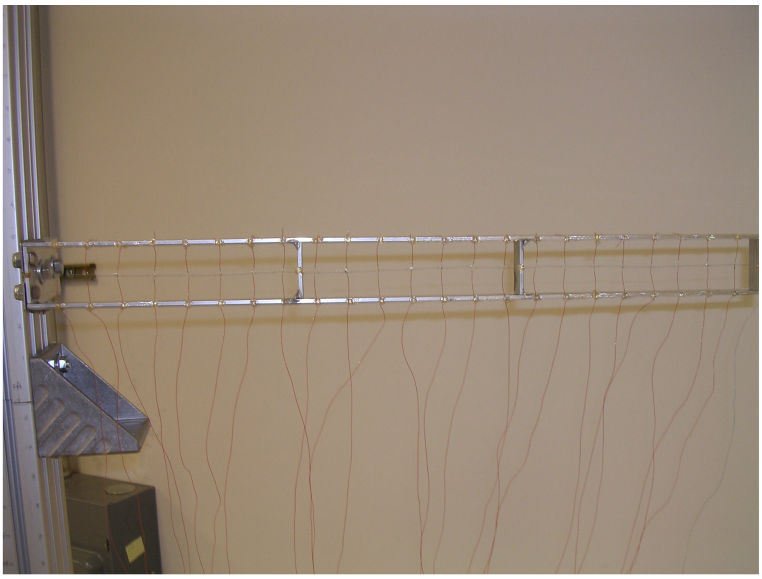

Figure 23: Thermocouple Row

In order to verify that the measurement methods are repeatable, consider the following: Figure 24 shows the outlet temperatures of the server simulator (with the same heat loads and dial setting) using the two measurement methods. It should be noted that the thermocouples were actually located approximately 6.35 mm (0.25 in.) outside the outlet grille of the server simulator. The figure on the left (a) was obtained by using the vertical row of thermocouples that were glued to a wire mesh and then traversed

horizontally. The figure on the right (b) was obtained by using the thermocouple grid that was traversed vertically.

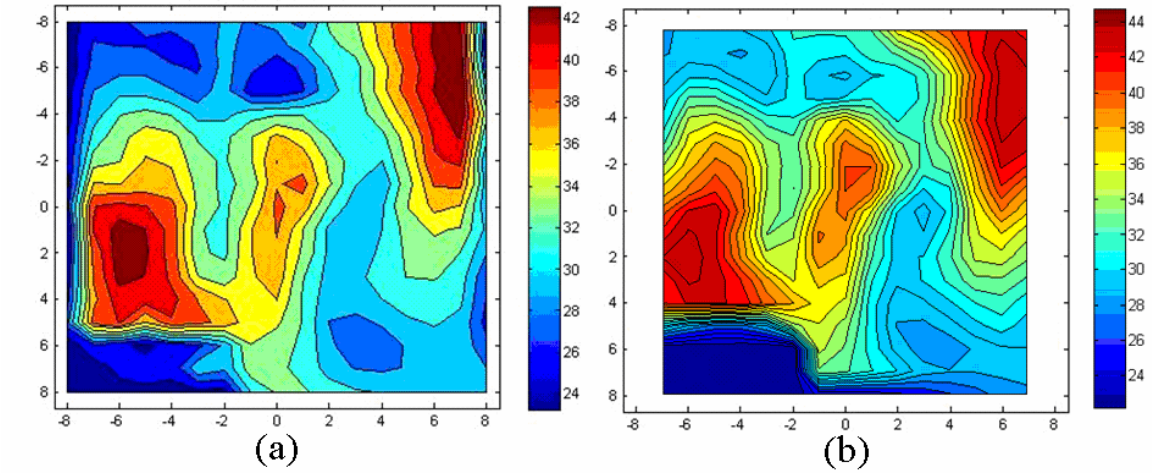

Figure 24: Repeatability between Temperature Measurement Methods (a) Vertical Row of Thermocouples Attached to Grid (b) Horizontal Row of Thermocouple Wire

The results confirm that the second measurement method is valid and that the temperature measurements are repeatable. It is important to point out that these measurements were taken at two different points in time, and in comparing the two it should be noted that the ambient conditions may not have been exactly the same for both cases. This second method was used for the majority of server simulator and rack outlet temperature measurements.

2.2.2 Fan Pressure Characteristics and Component Pressure Drop Measurements

In order to model the server simulator and rack accurately, it was necessary to determine the flow characteristics of many of the components. For example, in order to model fans, one must know the static pressure that a fan imposes as a function of the air flow rate through that fan. This is known as a fan performance curve. Conversely, to model grilles and banks of fins one must know the pressure *drop* as a function of the air flow rate through those components.

Differential Pressure Transducers

All differential pressure measurements were taken with an OMEGA PX137-001 DV Pressure Transducer. Figure 25 shows some of the pressure transducers with tubing and wiring.

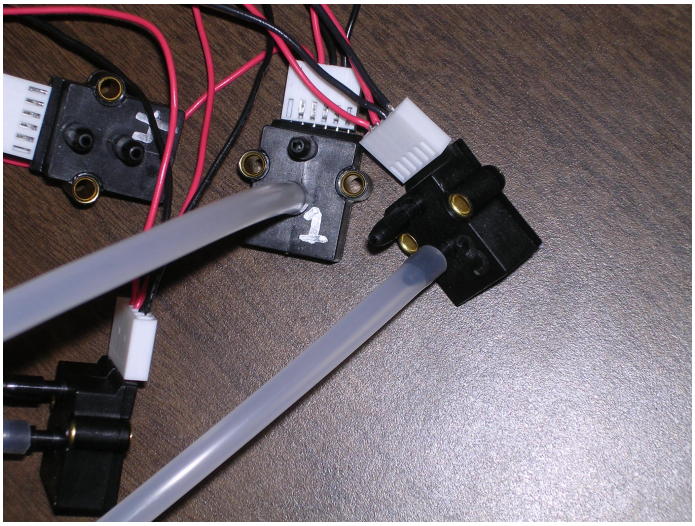

Figure 25: Pressure Transducers

There are two ports on the transducer. Tubing may be attached to either or both of these ports to measure differential pressures. The bottom port is the positive side, and it may be used alone if the gage pressure is the desired output.

Essentially, a strain gage is attached to a diaphragm that is between the two pressure sources, which are then connected to either or both of the ports. The deflection of the diaphragm by an imposed pressure on either side of the transducer is measured by the strain gages, and a voltage is produced.

The transducers are powered by a 12 V DC power source, so a 12 V AC-to-DC adapter was used. There are six metal pins at the top of the transducer. The second and fourth pins must be wired to the positive and negative leads of the voltage supply, respectively. The third and fifth pins give the positive and negative voltage outputs, respectively, as a function of the pressure difference (The first and last pins are not used).

The transducer has a differential range of 0 to 6895 Pa (1 PSI), and an output range of 18 ±1 mV. According to the manufacturer, the voltage output of the transducers is expected to be repeatable within approximately 0.01% of the full scale voltage output (0.0018 mV). Since the calibration curve shows that 1 V ≈ 375,000 Pa, the overall uncertainty of pressure drop measurements is approximately 0.7 Pa.

The voltage readings were taken with a FieldPoint FP-AI-112 16-Channel, 16-Bit Analog Input Module. This module is similar to the FP-TC-120, except that there are 16 channels, as opposed to 8. All of the negative output leads of the pressure transducers were wired to the same ground terminal, and each of the positive leads was then wired to a separate channel input in the FP-AI-112 module. The error depends on the input range selected, and it should be noted that all pressure measurements reported in this study were taken with the ±65 mV range. According to the manufacturer, the effective resolution (which includes quantization errors and noise) for this range is approximately 3 μV. The manufacturer also quotes the typical accuracy as being between 0.03 and 0.1% of the measured value. All pressure measurements were taken with Labview at a frequency of 500 Hz for two minutes per pressure measurement.

Airflow Test Chamber

An AMCA 210-99 Airflow Test Chamber was used to determine both the fan curves and the pressure drop characteristics of the main components (fins and grilles). Figure 26 shows the main components of the airflow test chamber. The main components of the main chamber are the **inlet**, the **static pressure tap**, the **differential pressure taps**, the **nozzle plate**, and the outlet **blast gate**. A **flexible duct** connects the outlet of the main chamber to a **counter blower**.

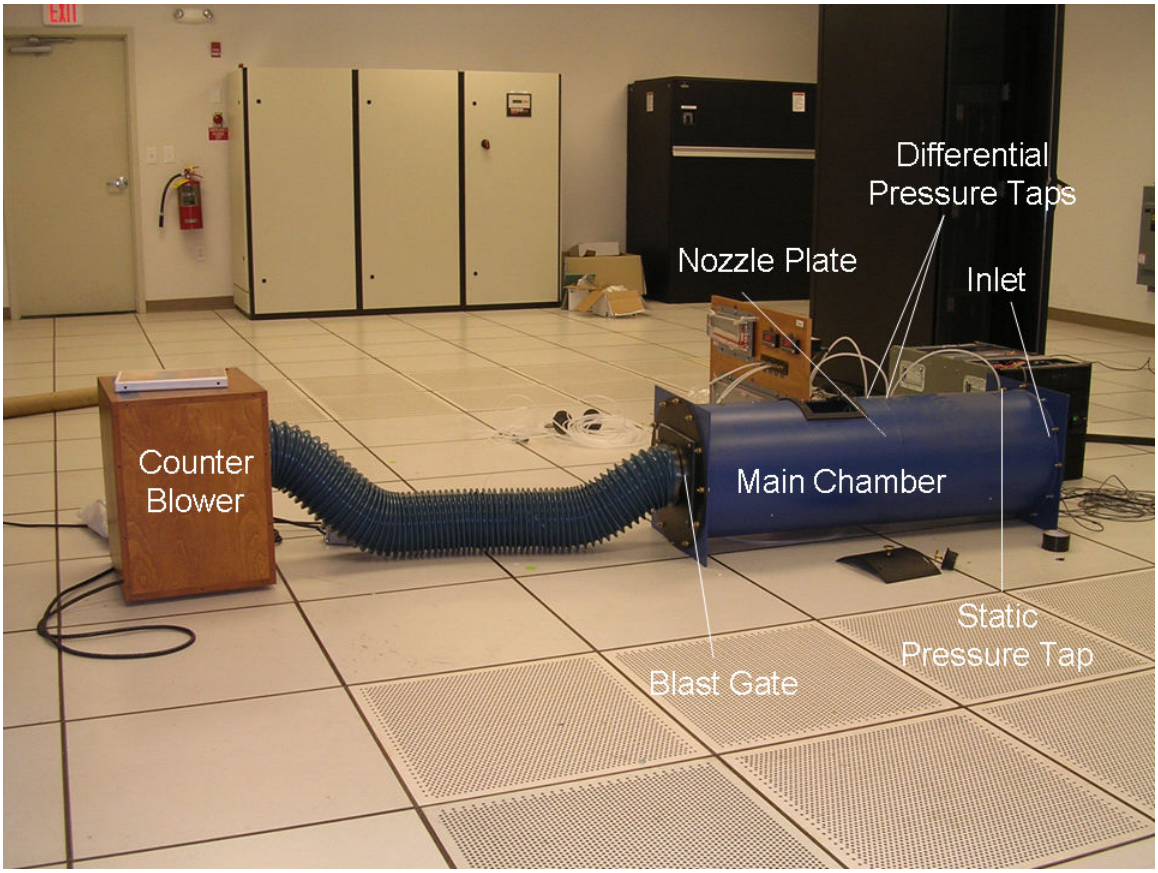

Figure 26: Airflow Test Chamber

The static pressure tap, which is just beyond the inlet, allows one to measure the differential pressure across the component of interest – whether one is interested in a fan performance curve or a system impedance. Figure 27a shows an overhead view of the main chamber, and Figure 27b shows a fan (the one used in the APC server simulators) mounted to the inlet. There is a plate of nozzles about halfway through the chamber (See Figure 27c).

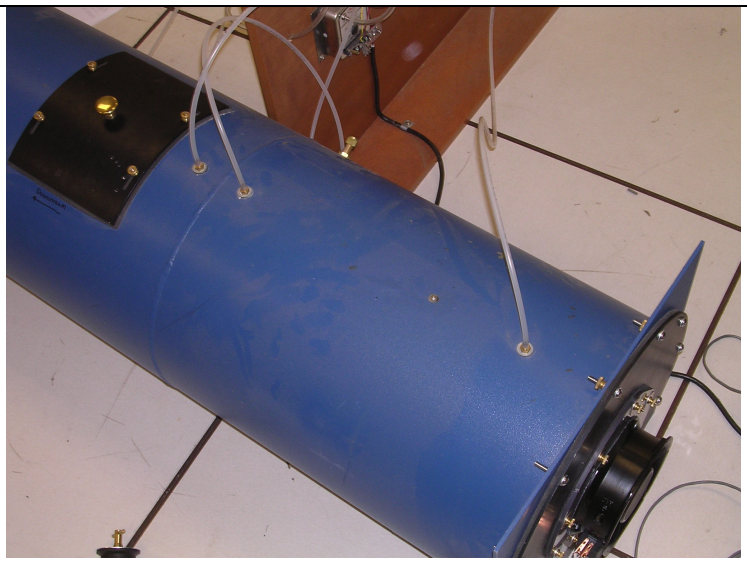

(a)

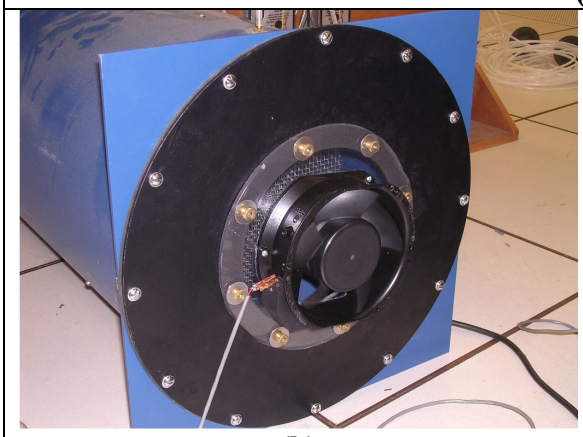

(b)

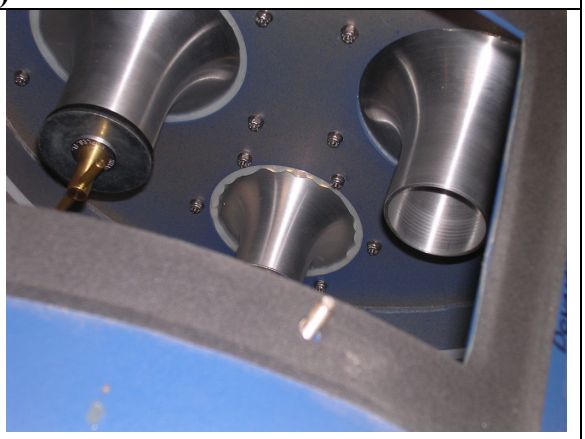

(c)

Figure 27: Airflow Test Chamber (a) Overhead View (b) Fan Mounted to Inlet (c) Nozzle Plate

The purpose of the differential pressure measurement across the nozzle plate is to estimate the air flow rate. The plate contains five nozzles: one 0.688 in., one 1.0 in., one 1.6 in., and two 2.0 in. nozzles. The air flow through the chamber is a function of the differential pressure across one or more of the nozzles. The manufacturer provides these relationship curves. For example, Figure 28 shows the air flow rate vs. differential pressure measured across the plate with only a single 2 in. nozzle open, and the rest sealed with stoppers.

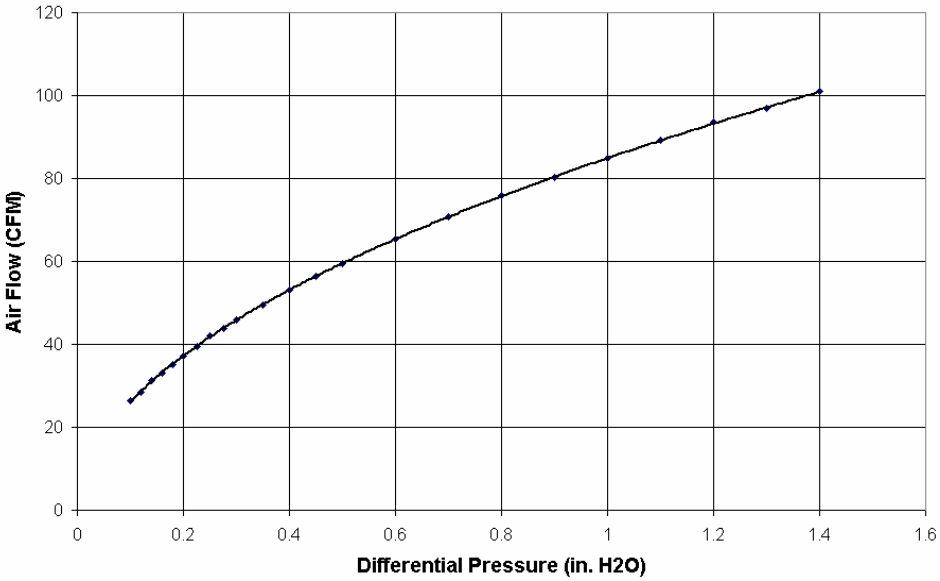

Figure 28: Air Flow Rate vs. Differential Pressure across 2 in. Nozzle

It is important to note that the lower limit of the differential pressures is 24.91 Pa (0.1 in. H_2O). This is to ensure that the flow through the nozzle is fully turbulent. A maximum of 996.4 Pa (4.0 in. H_2O) is also imposed in order to ensure that compressibility is not a factor. See Appendix D for the remaining nozzle curves. It is important to point out that the manufacturer does not present any information about the uncertainty involved in converting from differential pressure to air flow rate. The effect of this uncertainty will be discussed in Chapter 4.

The flow rate in the chamber can be varied in one of two ways (See Figure 29).

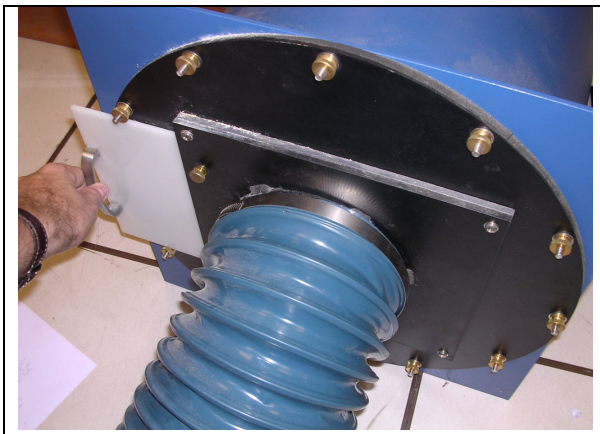

(a)

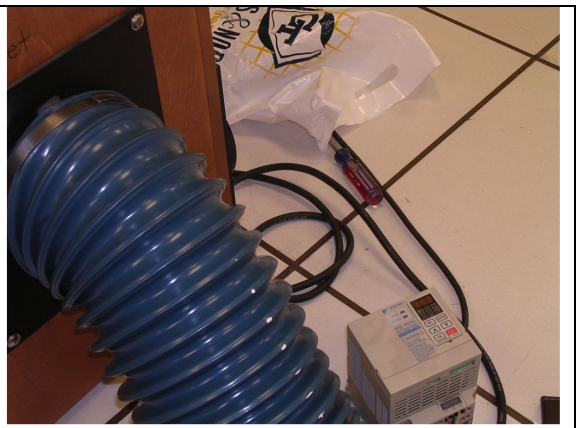

(b)

Figure 29: (a) Blast Gate (b) Counter Blower

A blast gate (a) slides along a track at the outlet of the main chamber. One can reduce the air flow rate by simply opening or closing this blast gate and screwing it into place (to prevent leakage). The counter blower (b) is ducted to the outlet of the main chamber through a flexible duct. The blower is run with a MagneTek GPD 205 Controller, which allows one to vary the frequency of the blower by multiples of 0.1 Hz, and thereby vary the air flow rate through the chamber.

Calibration of the Pressure Transducers

The differential pressure detected by the pressure transducers should be linearly proportional to the voltage output; therefore, only two points are needed to determine the relationship between the two. For the sake of completeness, however, the pressure transducers were calibrated before each set of measurements was taken. To calibrate the transducers, the following procedure was used. First, tubing was run from a Durablock inclined manometer with a 2.49 Pa (0.01 in. H_2O) resolution to the pressure taps on either side of the nozzle plate. The manometer was balanced and zeroed, and then the counter blower was set on a low frequency. One or more nozzle stoppers were removed, depending on the desired air flow rate range. Next, the frequency of the counter blower was slowly increased until the manometer reading was above 24.9 Pa (0.1 in. H_2O). This served as the first data point. The manometer pressure drop reading was then recorded for a number of increasing counter blower frequencies.

After the relationship between the counter blower frequency and the manometer pressure reading was found, the pressure transducer was attached to the taps on either side of the plate. Voltage measurements were taken by the pressure transducer at the same counter blower frequencies as before. The inclined manometer pressure was then plotted as a function of the transducer voltage in order to find the relationship between voltage and differential pressure. Appendix D contains more information on the pressure transducer calibrations, but the following is a representative of one calibration curve.

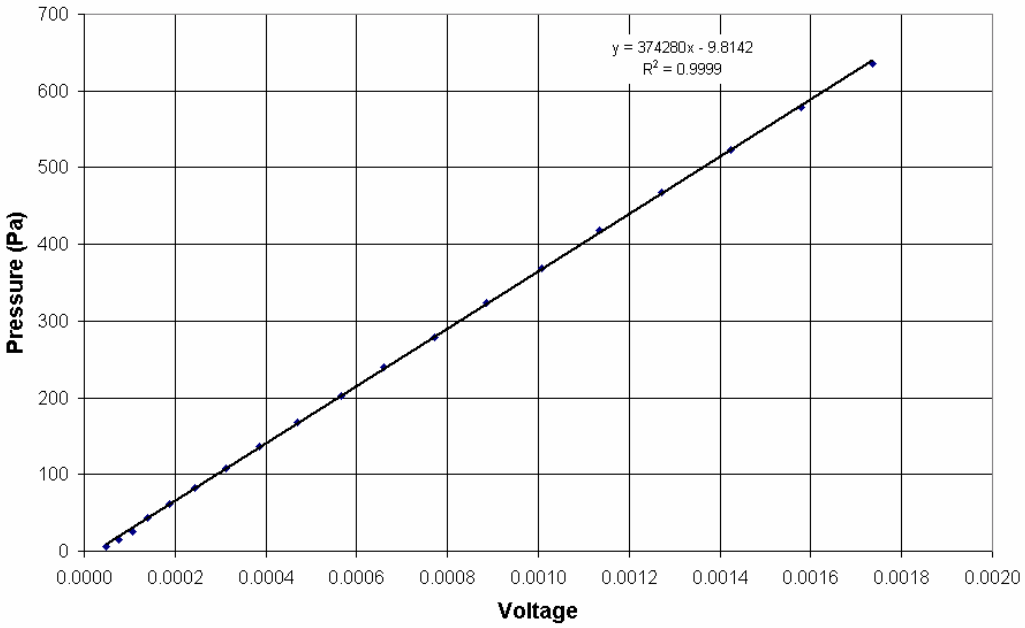

Figure 30: Pressure Transducer Differential Pressure vs. Output Voltage

Note that the relationship between the differential pressure and the output voltage is indeed very linear ($R^2 = 0.9999$).

2.2.3 Velocity Measurements

Particle Image Velocimetry (PIV) Basics [29]

Particle Image Velocimetry (PIV) is essentially an optical method for retrieving the flow dynamics of a moving fluid, which may be liquid or gaseous. The basic components of a PIV system are represented in the following Figure 31.

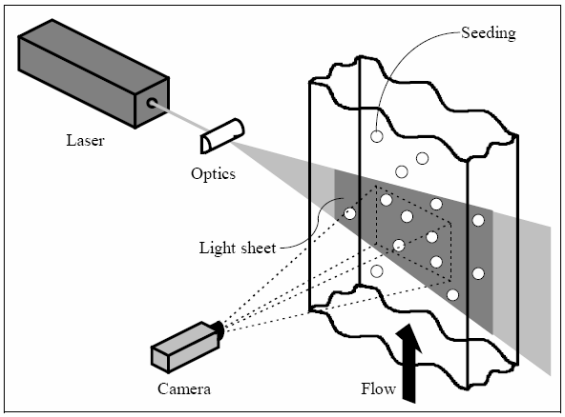

Figure 31: The Basic Components of a PIV System [29]

The basic premise of PIV is that the velocity field may be estimated by measuring the distance that a particle travels and dividing that by the time it takes for that particle to travel that distance (speed = distance/time). To actually accomplish this, the system requires reflective particles, known as "**seeding** particles," to be introduced into the fluid **flow stream**. A **laser** is then pulsed to create a **light sheet** that illuminates the seeding particles. A digital **camera** then captures the image. The laser is then pulsed immediately after the first, and the camera again takes a quick image. Post-processing software is able to detect individual particles and track them between the two images.

There are many advantages of using PIV to calculate the velocities of a moving fluid. For one, the velocity of an entire fluid may be found at an instantaneous point in time. If one uses a typical velocity instrument, such as an anemometer or a Pitot tube, then the velocity can only be measured at a single point at any given time. If the flow velocity is unsteady over time, it is not possible to accurately obtain velocity maps using point-wise measurements. Also, PIV is non-intrusive, meaning that it does not obstruct the flow. Other instruments may alter the flow patterns and throw off the measurements.

Figure 32 shows an example of the PIV process. The first image is a raw photograph of the seeding particles. If one were to toggle between image frames (sequential images), it would be possible to see the basic displacement of the particles. The next step (b) is to subdivide the image plane into "interrogation areas," which can be seen by the yellow lines in (a). Correlations are then used to determine the velocity field over the entire image frame. Images (c) and (d) show an example of post-processed data: velocity vectors and streamlines, respectively.

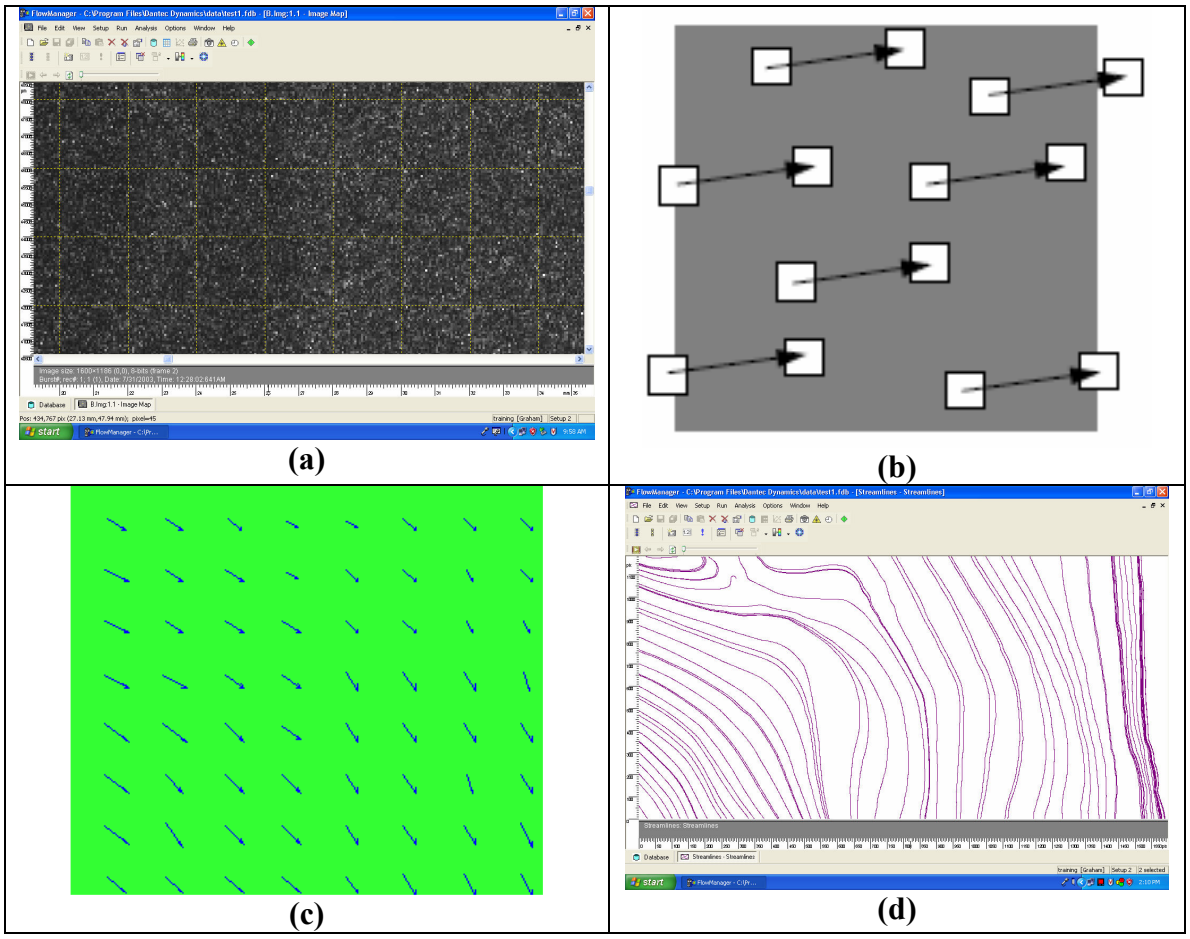

Figure 32: PIV (a) Raw Image (b) Interrogation (c) Post-Processed Velocity (d) Streamlines

The most commonly-used correlation (and the one previously described) is known as "cross-correlation," which uses two separate frames to pick out individual particle displacements. A cross-correlation technique works as follows: Within each interrogation area, an average spatial shift is observed, and the average velocity is then calculated for each interrogation area. After this, the results of each interrogation area are stitched together to form an entire velocity field. Figure 33 shows the overall cross-correlation process.

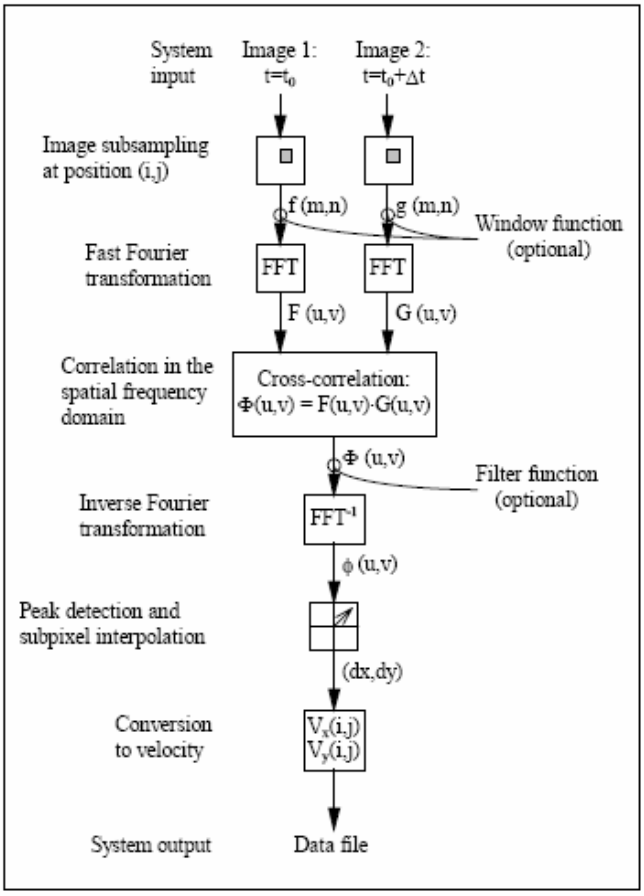

Figure 33: Cross-Correlation Process [29]

The images may be filtered to reduce erroneous velocity vectors that are the result of noise.

It is important to point out that this method assumes the velocity field of the fluid by making optical observations of the seeding particles, rather than the fluid itself. No matter what method one uses to estimate the velocities, there will be random correlations between the initial positions of some particles and the final positions of other particles. This is known as "noise." The seeding method determines the amount of noise in a system, and it is important that the seeding method causes the actual correlations to far outweigh the random ones, in order to provide useful data. One way to reduce the amount of noise is to make the seeding density dense. For example, one rule of thumb is that there needs to be at least ten particles across each interrogation area [29]. Also, the

material of the seeding particle is important. The individual seeding particle must have a large enough diameter so that it has a large enough signal-to-noise ratio (SNR), which allows it to be detected easily. On the other hand, it must be small enough so that it travels with the fluid without altering the flow. It has been observed, for example, that smoke is an excellent seeding choice for low velocity air flows, such as what occurs in a data center environment.

Another rule of thumb is that the seeding must be homogeneous across the entire image map. Figure 34 shows an example of nonhomogeneous and homogeneous seedings.

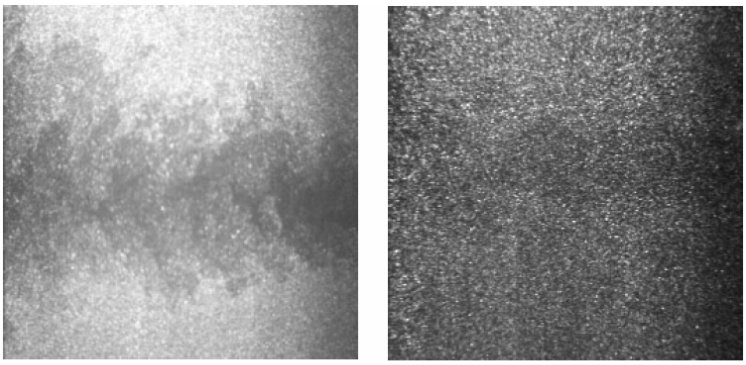

(a) (b)

Figure 34: (a) Nonhomogeneous and (b) Homogeneous Seeding

A nonhomogeneous seeding will often produce useless results. When the image is split into equal interrogation areas, some of these areas will have too many particles, while others will have too few.

Because PIV estimates the fluid velocity of every particle as approximately linear, sequential images should be taken at small amounts of time. Unfortunately though, in order to effectively post-process the images, a particle should travel approximately 25% across an interrogation area. Therefore, the time between laser pulses should be altered according to the estimated velocity of the fluid. It is further recommended that either a 32 or a 64 pixel interrogation area be used, which further confines the time between pulses. It also confines how detailed of a velocity map one may obtain given the requirements and the fluid flow properties.

Stereoscopic PIV System at the Data Center Lab

For this study, a 3-dimensional, or "stereoscopic," PIV system was used. Stereoscopic PIV works just like a conventional 2D PIV system, except there are two cameras instead of one. Each camera focuses on a separate 2D plane, with one image plane directly behind the other. With a typical 2D system, many particles are lost when they travel outside the image plane. Not only can a stereoscopic system reduce the number of lost particles, but it can also determine some velocity component in the third direction (into and out of the 2D plane). Figure 35a shows the system used in the lab.

(a)

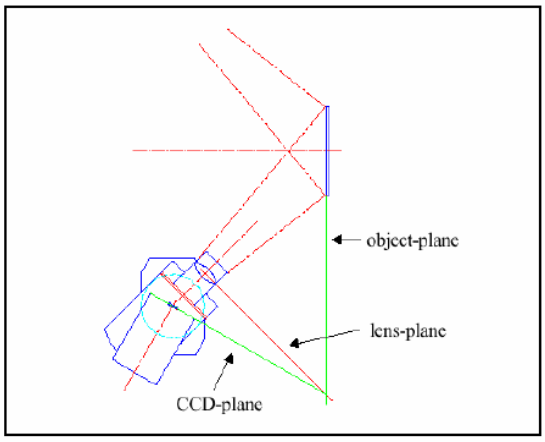

(b)

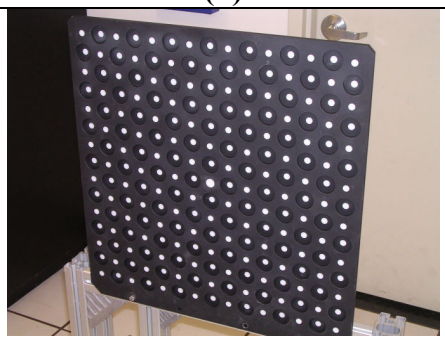

(c)

Figure 35: Stereoscopic PIV (a) Traverse System (b) Camera Basics (c) Calibration Target

Image (a) in the above figure shows the PIV traverse system that was used to take velocity measurements in the data center lab. The traverse allows one to move the entire laser-camera assembly either laterally (toward the CRAC units in the above picture) or vertically (toward the ceiling). Two Flow Sense M2/E 8 bit cameras are mounted

vertically on the traverse. A NewWave Gemini laser emits the light, which is reflected off a pair mirrors to create a laser sheet. The circular black object in the lower left of (a) shows the source of the laser sheet that creates the image plane. Each of the cameras focuses on the same 2-dimensional image plane. This process may be visualized in (b). The camera charging device (CCD) plane can be rotated, while keeping a fixed lens angle, in order to reduce the distortion on the image plane. It should be mentioned that the lasers and cameras were controlled using the Dantec FlowMap System Hub and PIV software FlowManager v. 4.71.

The calibration target, which is pictured in Figure 35c, is used to account for the distortion created by using a stereoscopic PIV system. The target has two levels, which are spaced 6 mm apart. One camera is focused on the white dots of the front level, and the other camera is focused on the dots of the back level. The dots have a diameter of 10 mm, and they are spaced 32 mm apart. The large marker (15 mm) in the middle is used to relate the positions of the two camera planes. Figure 36 shows the 3D calibration.

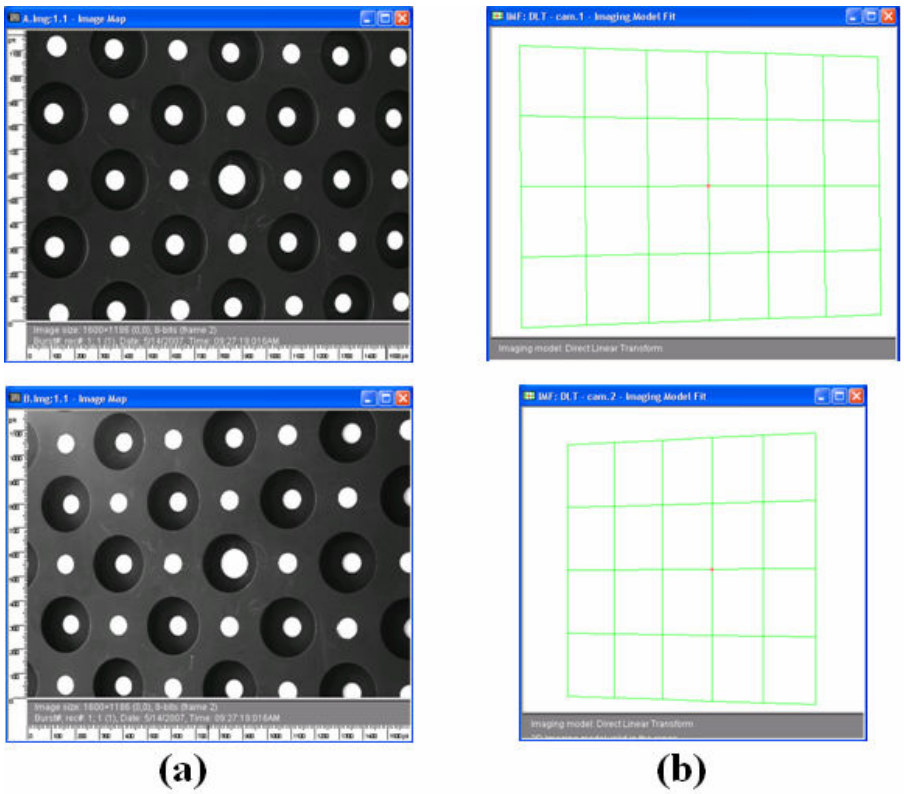

Figure 36: 3D PIV Calibration

The two images in (a) are photographs of the target. The top image is from the top camera, and the bottom image is from the bottom camera. The top camera was focused on the front plane, and the bottom camera was focused on the rear plane of dots. Notice how the line of dots along the camera image goes at an angle. In reality, each line of dots was horizontal, but because the camera is at an angle, the image is distorted. This will have a large effect on the way the velocity is calculated, unless a 3D calibration is performed using FlowManager. The two images in (b) show calibration grids, as found from the FlowManager calibration. When used along with vector maps from each pair of camera images, the distortion is accounted for, and the actual velocity vector maps of that plane may be obtained.

Server simulator outlet velocities were obtained using the PIV system. The velocities were taken for three different dial settings – 2, 5, and 8 – to observe any profile changes that would occur and to estimate the point-wise velocity magnitudes. To do so, PIV data were taken at five different image planes, all perpendicular to the server simulator outlet. Figure 37 shows an explanation of the PIV planes.

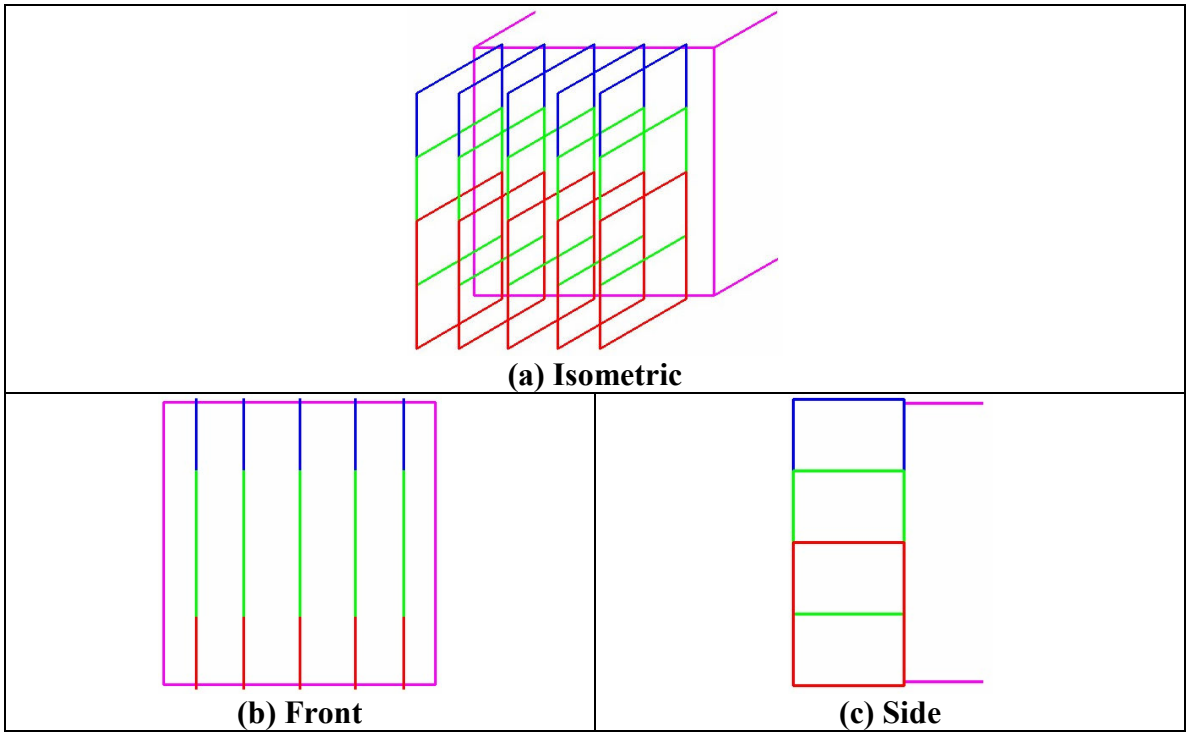

Figure 37: Explanation of Server Simulator Outlet Velocity Measurements

Each outlet plane actually required two sub-planes, as the camera images were only approximately 23 cm (9 in.) in the vertical direction by 17.8 cm (7 in.) in the horizontal. Therefore, ideally, the two images could be stitched together to capture the entire 44.5 cm (17.5 in.) server simulator. To reduce the errors associated with seeding "dropout," in which a particle in one frame travels outside the image frame between images, another plane was taken in the middle to overlap the two top and bottom image planes.

For each point, 40 pairs of images were obtained. In other words, each of the two cameras took two consecutive images a total of forty times. Each camera image from a pair was broken into 32x32 pixel interrogation areas, and an adaptive correlation was used to obtain raw velocity vector maps. A moving-average filter was applied to each of the vector maps in order to delete random vectors that exist due to noise. A moving-average filter essentially looks at a single vector, and it averages the magnitudes of the vectors surrounding it. If the certain vector is not within a certain tolerance of the others, it is omitted. After the moving-average filter was applied, the vector maps from each camera were combined using a 3D calibration to produce the actual vector maps.

In order to actually obtain outlet velocity values, the vectors at a single vertical line in the plane – located approximately 10 mm. outside the outlet of the server simulator – were used. It was noticed that the component normal to the outlet accounted for approximately 98% of the velocity magnitude that close to the server simulator. Therefore, that component was used as the basis of comparison. The data were averaged over the forty points to obtain the velocity values at each of the five planes. See Appendix E for a more detailed description of the process.

2.2.4 Air Flow Rate Measurements

Flow Hood Air Flow Measurements

Air flow rates were taken with a Shortridge Instruments AirData Multimeter ADM-850L, attached to a FlowHood, which directs the air flow across a manifold. The manifold simultaneously senses the total and static pressures at sixteen orifices.

(a)

(b)

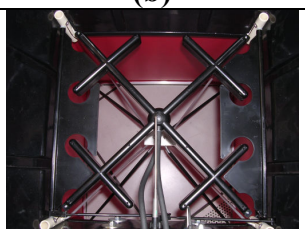

(c)

Figure 38: (a) FlowHood (b)Open Flaps (c) Closed Flaps

Figure 38a shows the FlowHood that was used for CFM measurements of the server simulator. The instrument corrects for its own flow resistance and back-pressure using flaps that open and close – as pictured in (b) and (c). It also corrects for local temperature, and the manufacturer quotes that the air flow values are accurate within ±3% of the reading or ±0.003304m^3/s (7 CFM) over the range of 0.01180 m^3/s to 0.9439 m^3/s (25 - 2000 CFM). The flow hood was used to measure the overall air flow rates at the outlet of the server simulator. The outlet of the server simulator was placed at the entrance of the hood. The open area of the flow hood – the area that was beyond the server simulator – was packed with foam to ensure that no superfluous amount of air could enter the flow hood from the room or exit the flow hood to the room. It is important to note that the air flow rates were measured without any heat dissipation, and therefore, the effect of changing air density on the flow rate was not quantified (See Chapter 4).

CHAPTER 3

DEVELOPMENT OF THE COMPACT MODEL

This chapter explores the compact modeling of an electronics enclosure. Different methods of representing components that are in a typical electronics enclosure are discussed. A compact CFD-HT model of an electronics enclosure was developed using a commercial CFD-HT software package, Fluent. The APC server simulators served as the foundation of the compact CFD-HT model. Although these server simulators do not represent actual server cabinets, they contain many components that will be found within typical electronics enclosures; so, a description of the development of a compact model of each of these components could prove useful for similar applications. Also, the server simulators contain a number of heaters that can be turned off and on, and which each dissipate a known amount of heat. In addition, each of the simulators contains a set of fans, with controllable rotational speeds. This allows one to use experiments to directly compare temperature and velocity maps to those found by the CFD-HT model. This chapter describes the approach to characterizing the server simulator and rack using CFD-HT. A description of the compact modeling of each of the important components is discussed. The results of the empirical fan performance and component pressure drop curves are also presented.

3.1 Basic Model Description and Dimensions

The model was created using GAMBIT 2.2.30, which is Fluent's preprocessing software package. GAMBIT is essentially a graphical interface that allows one to create a geometrical object, define boundary entities and continuum types, and create and export a mesh for use in a CFD-HT solver software package. Fluent 6.2 was then used as the CFD-HT software package through which the Navier-Stokes equations were solved.

3.1.1 Server Simulator Model Description and Dimensions

Figure 39 shows the basic geometry for the compact CFD-HT model of a single server simulator. The figure shows one representation of the important components inside, but the fan, fin, and grille models are discussed later in this chapter.

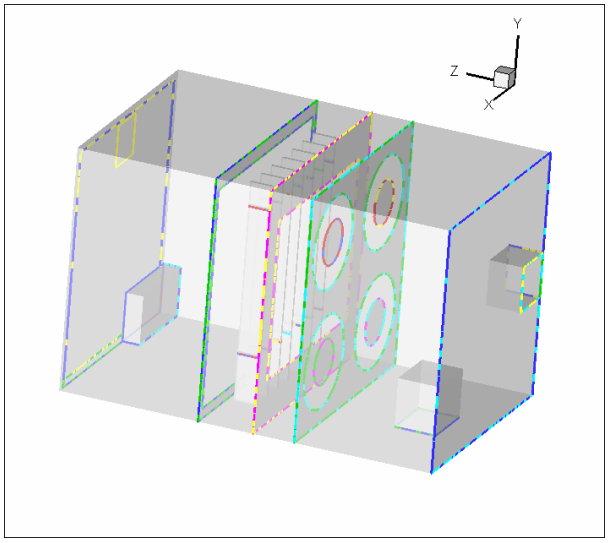

Figure 39: Server Simulator Basic CFD-HT Frame

The cabinet model was 43.2 cm (17 in.) wide, 44.5 cm (17.5 in.) tall, and 69 cm (27.125 in.) long. The outer walls of the server simulator were modeled as infinitesimally-thin adiabatic faces, which are made of aluminum (all materials are aluminum unless otherwise stated). The walls were assumed to be adiabatic based on temperature measurements of the top of the case. Measurements at the lowest dial setting and the highest heat load revealed that the casing temperature of the top of the server simulator –

just before the outlet – only reached approximately 24.4°C (76°F). This was found when the server simulator was surrounded by ambient air. When the server simulator is mounted in a rack and surrounded by other units, the thermal resistance will be much higher, and the heat transfer will be even smaller, and thus negligible.

The inlet and outlet grilles were both modeled as faces (this is discussed later in the chapter). The set of dials on the inlet was modeled as an infinitesimally-thin wall, and the fan speed and heat controls themselves were lumped into a single cubic block for simplicity in meshing. The power converter near the inlet was modeled as a single cubic block as well (refer back to Figure 8 on page 24 for the actual geometrical shape).

The fan plate was also modeled as an infinitesimally-thin wall. Notice that the fans are modeled as circular faces, with a thin circular wall to represent the hub. Three different geometrical fan models were explored. This is also discussed later in the chapter.

The entrance to the heater space was modeled as a rectangular opening in an infinitesimally-thin wall. The heater space is really only as tall as the heaters themselves. The space is bordered by a cubic mass of aluminum that is 0.5 in. thick on the left and right, 0.75 in. on the bottom and 1 in. on the top.

The heaters were modeled as rectangular parallelepipeds, and it was assumed that each heater is stainless-steel throughout the volume of the heaters. One significant assumption in this model was that the heat generation is geometrically uniform and steady over time for each heater. In reality, the heat is generated by a wire, which weaves through a ceramic filling that is surrounded by a stainless steel sheath. The heat removal occurs primarily by convection from the heater surface and the fins; therefore, it was assumed that any temperature gradient within the heater itself is negligible, and the heater can be modeled as a solid block.

It was also assumed that the heat is only generated in the portion of the heater that is surrounded by fins. This assumption was made because the power input occurs just

below the bottom fin, and the electrical wires travel only throughout the portion of the heater that is surrounded by fins. The remaining portion of the heater is used for mounting it to the cabinet. The actual dimensions of each heater (0.25 in. x 1.625 in. x 15.75 in.) equate to a total volume of 6.4 in.^{3} (1.049 x 10^{-4} m.^{3}), but it was assumed that only 10.6125 in. of the height generates heat, which makes the heat-generating volume 4.3 in.^{3} (7.065 x 10^{-5} m.^{3}). It is important to point out that it is unknown how uniform the heat generation actually is. Table 3 gives the assumed volumetric heat generations of each heater, which were used as inputs in the model. The fins surrounding the heaters are not pictured in this figure. Different ways of representing the fins are discussed later in this chapter.

Table 3: Volumetric Heat Generation of Each Heater in CFD-HT Model

Heater	Heat Generation (W)	Volumetric Heat Generation (W/m^3)
1	1,000	1.415 x 10^7
2	500	7.077 x 10^6
3	1,000	1.415 x 10^7
4	1,000	1.415 x 10^7
5	1,000	1.415 x 10^7
6	250	3.539 x 10^6
7	1,000	1.415 x 10^7

The power supply was modeled as a cuboid block as well, and the temperature gage at the top middle of the outlet was modeled as an infinitesimally-thin wall. All wires were neglected in the model, since the wires run through areas of little or no air flow. Including the wiring in the model would therefore be unnecessary.

3.1.2 Rack Sub-System Model Description and Dimensions

In reality, the full-sized electronics enclosure contains four server simulators stacked vertically to form a 40U rack. Within the rack, however, the walls of the server simulator are approximately adiabatic; therefore, a negligible amount of heat will be transferred vertically between server simulators. Also, because fans are utilized to pull air from the front of the server simulator and force air out the back, it can be assumed that not much of the air mixes in the plenum.

Because the server simulators are exactly the same geometrically, and because a negligible amount of heat and air is transferred between the units, a model of a rack can be split into four equal segments, where each segment is composed of the server simulator, the mounts on either side, the space between the rack inlet and the server simulator inlet, and the portion of the exit plenum between the server simulator outlet and the rack outlet. Figure 40 shows the rack sub-system model.

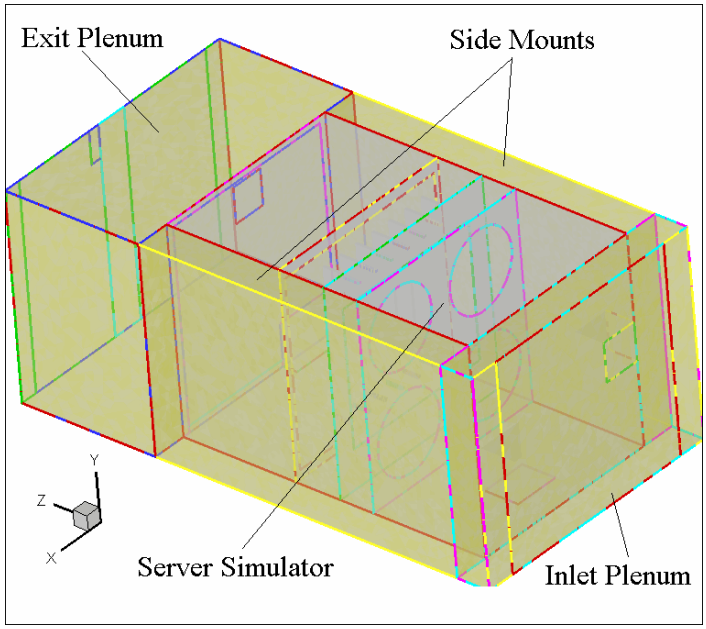

Figure 40: Rack Sub-System Model

The rack sub-system model has a height of 44.5 cm (17.5 in.), a width of 58.4 cm (23 in.), and a depth of 1.07 m (42 in.). The grey-shaded volume is the server simulator

model, and the yellow-shaded regions are the ones added to create the rack sub-system model.

The inlet and outlet grilles of the rack were simulated as faces, like the grille models of the server simulator. The vertical lines on the inlet and outlet of the rack are the outlines of borders – through which fluid cannot pass. The sides of the rack were modeled as adiabatic. Any top or bottom boundaries of the model that are outside the server simulator (basically the tops and bottoms of the rack inlet and outlet plena) were modeled as symmetric borders. A symmetric boundary confines the fluid to the space, while ensuring that there is no frictional pressure drop at that boundary. The server simulator mounts – on either side of the unit – were modeled as cuboid volumes.

3.2 Grille Modeling

There are two grilles in the server simulator: an inlet grille and an outlet grille. There is also an inlet grille and an outlet grille of the rack. As was shown in Figure 9, the inlet grille is composed of a thick plastic channeled grill with a metal grid of square openings behind it. To accurately model the actual openings of both the plastic and metal parts, a large mesh would be required; thus, the details of this grille cannot be contained in a compact CFD-HT model. Similarly, the diameters of the wires that form the server simulator outlet grille and the diameters of the circular openings of the rack grilles are too small to be represented accurately in a system-level CFD-HT model.

All grilles are approximated in GAMBIT (and Fluent) as being infinitesimally-thin **porous-jump** boundaries. A porous jump model is used to represent any thin membrane with a known pressure drop, which is a function of the flow rate. A porous jump model essentially assumes a 1-dimensional flow across porous media (porous media models are discussed in more detail later in this chapter). Such a model can be used for screens, filters, and radiators when conduction heat transfer is not of significant

importance [30]. Equation 3.1 gives the equation for the porous-jump model, which is derived from Darcy's Law (plus an inertial loss term) [30].

$$\Delta p = -\left(\frac{\mu}{\alpha} \upsilon + C_2 \frac{1}{2} \rho \upsilon^2 \right) \Delta m \tag{3.1}$$

In this equation, Δp is the pressure drop, μ is the viscosity, α is the permeability (a measure of the ability of a material to transmit a fluid), υ is the velocity, C_2 is the pressure-jump coefficient, ρ is the density, and Δm is the thickness of the medium. For an interior grille, the user inputs in Fluent are α, C_2, and Δm.

An inlet or outlet grille may be modeled in one of two ways: as a function of just the square of the velocity or as an n'th-order polynomial. If the grille is considered to be infinitesimally-thin, and if the pressure drop is assumed to only be proportional to the dynamic head, then the pressure drop can be represented by the following equation.

$$\Delta p = k_L \frac{1}{2} \rho \upsilon^2 \tag{3.2}$$

where k_L, the nondimensional loss coefficient, is an empirical input parameter. Alternatively, the pressure drop can be represented as a polynomial of any order. The coefficients of a porous-jump model may be found analytically or experimentally.

3.2.1 Analytical Determination of Grille Pressure Drops

The server simulator grille pressure drop characteristics were found analytically using the software program SF Pressure Drop 6.2 by Software-Factory. The pressure drop through grilles and channels is due to three factors: frictional pressure losses, gravitational losses, and changes in kinetic energy [31]. The software worked as follows: **First, the element type was chosen.** The inlet grille was modeled as a thick porous plate, and the outlet grille was modeled as a rectangular metal wire grid. **Second, the Reynolds number was calculated** using

$$\mathrm{Re} = \frac{\rho \upsilon D}{\mu} \tag{3.3}$$

where ρ is the density, υ is the velocity, D is the hydraulic diameter (this is a user input), and μ is the viscosity. **Next, it was determined, based on the Reynolds number, whether the flow is laminar or turbulent** (If Re > 2300, the flow is turbulent). **After this, the frictional pressure drop was estimated** based on the following three equations.

$$\lambda = \frac{64}{\mathrm{Re}} \qquad \text{(for laminar)} \tag{3.4}$$

$$\frac{1}{\lambda} = -2\log\left[\frac{2.51}{\mathrm{Re}\times\sqrt{\lambda}} + \frac{k_R}{D}\times 0.269\right] \quad \text{(for turbulent)} \tag{3.5}$$

$$\Delta p = \lambda \times \frac{L}{D} \times \frac{\rho}{2} \times \upsilon^2 \tag{3.6}$$

In the previous three equations, λ is known as the "friction factor," and k_R is known as the "absolute roughness," which is estimated based on the material.

Lastly, the pressure drops associate with the contraction and expansion of the air through the grille was found using Equation 3.7:

$$\Delta p = \zeta \times \frac{\rho}{2} \times \upsilon^2 \tag{3.7}$$

where ζ is a loss coefficient (different resistance coefficients are used for expansion and contraction). This pressure drop due to the contraction and expansion of a fluid is the largest contributor to the overall pressure drop across a grille.

For both grilles, the gravitational pressure drop and the pressure drop due to changes in kinetic energy were neglected. The latter will only occur if there is a gradual change in cross-sectional area over the length of a pipe or channel, which is not the case.

The pressure drop was found for both the inlet and outlet grilles as a function of the air flow rate. The approach velocity was then found by dividing the air flow rate by the total area of the grille (43.2 cm x 44.5 cm). Figure 41 shows the results.

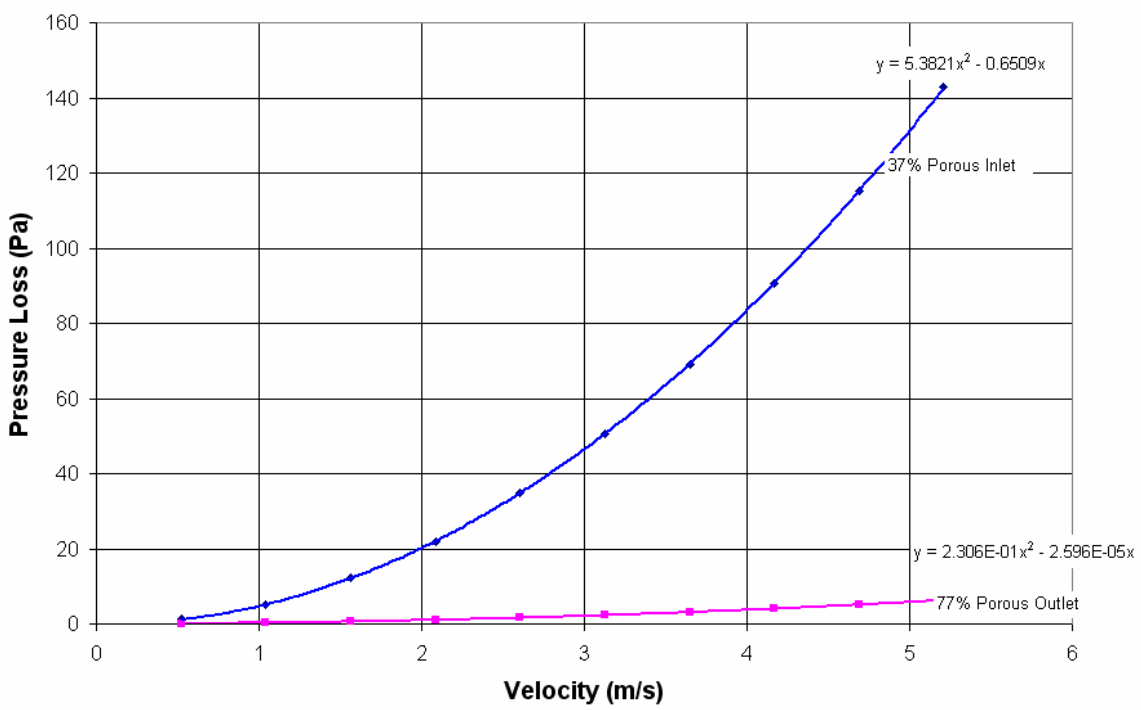

Figure 41: Analytical Server Simulator Grille Pressure Drops

According to the analytical model, the pressure drop of the server simulator outlet grille is negligible as compared to the inlet grille. For both grilles, the pressure drop is of the same form as expected in Equation 3.1; as a result, the data may be fit to a second-order polynomial to solve for the necessary coefficients.

3.2.2 Experimental Determination of Grille Pressure Drops

Analytical models can be a useful tool in determining the pressure drop across a grille with a geometry that exactly matches an analytical model. Unfortunately, models do not exist for every grille. When an actual grille does not exactly match an analytical model, one must experimentally determine the pressure drop characteristics. This was the case with the server simulator and rack grilles.

The airflow test chamber was used to experimentally determine the grille pressure drop characteristics. First, a 10.2 cm (4 in.) square, 15.2 cm (6 in.) long aluminum duct was constructed. The square duct was attached to a round sheet of Plexiglas. The edges of the duct were sealed with silicon in order to prevent leakage. The Plexiglas sheet was

screwed to the front of the airflow test chamber. A layer of foam between the test chamber and the sheet prevented leakage. Figure 42 shows the duct. Images (b), (c), and (d) are of the simulator inlet grille, simulator outlet grille, and rack grille mounted to the experimental duct, respectively.

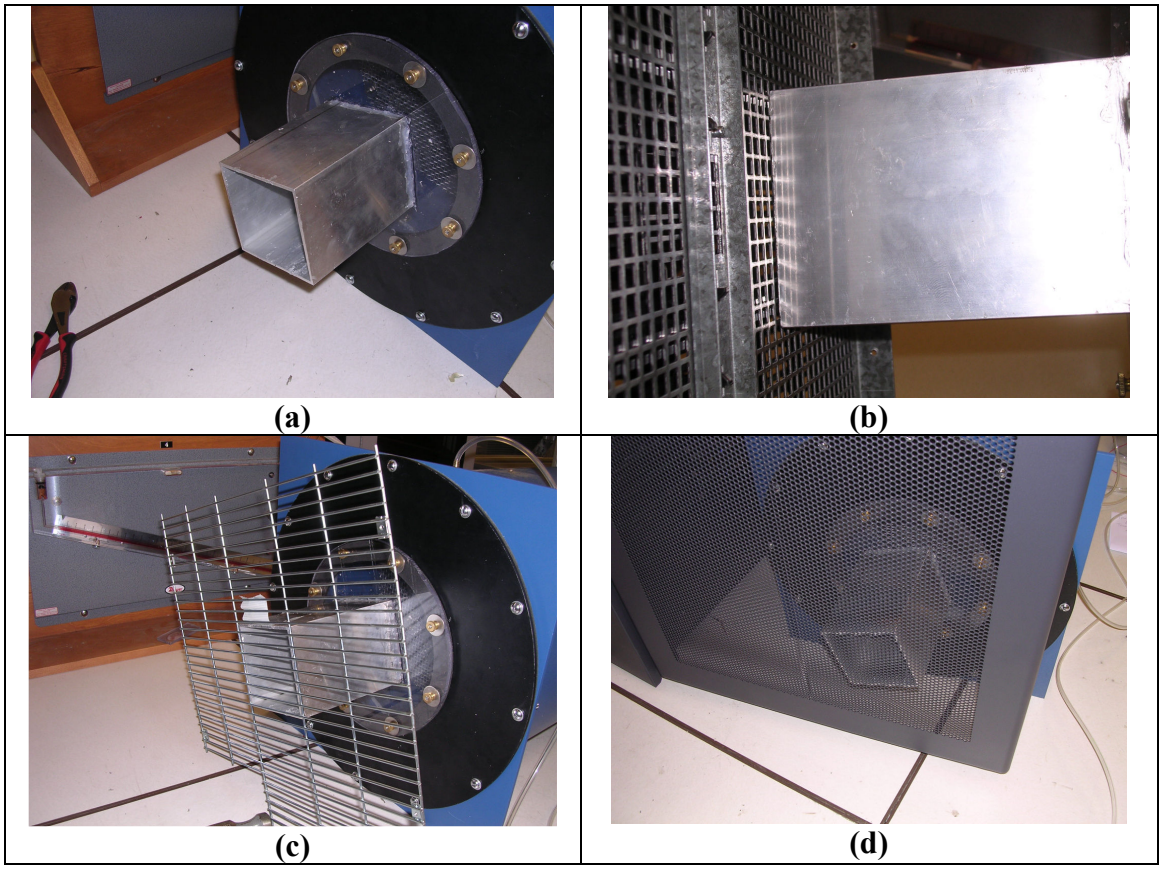

Figure 42: Airflow Test of (a) Duct (b) Inlet Grille (c) Outlet Grille (d) Rack Grille

For the lone duct, the blast chamber was opened all the way, and the counter blower was turned on a low rotational speed. The frequency of the counter blower was increased until there was about 0.1 in. H_2O pressure drop across the nozzle plate. This served as the first data point. The pressure drop across the duct and the pressure drop across the nozzle were taken (using Labview) over a 2 min. interval for each data point. Data were taken at different counter blower frequencies until the air flow rates corresponded to an average velocity of about 3.5 m/s.

The process was repeated with each grille mounted to the front of the duct, as pictured in (b), (c), and (d). Figure 43 shows the results.

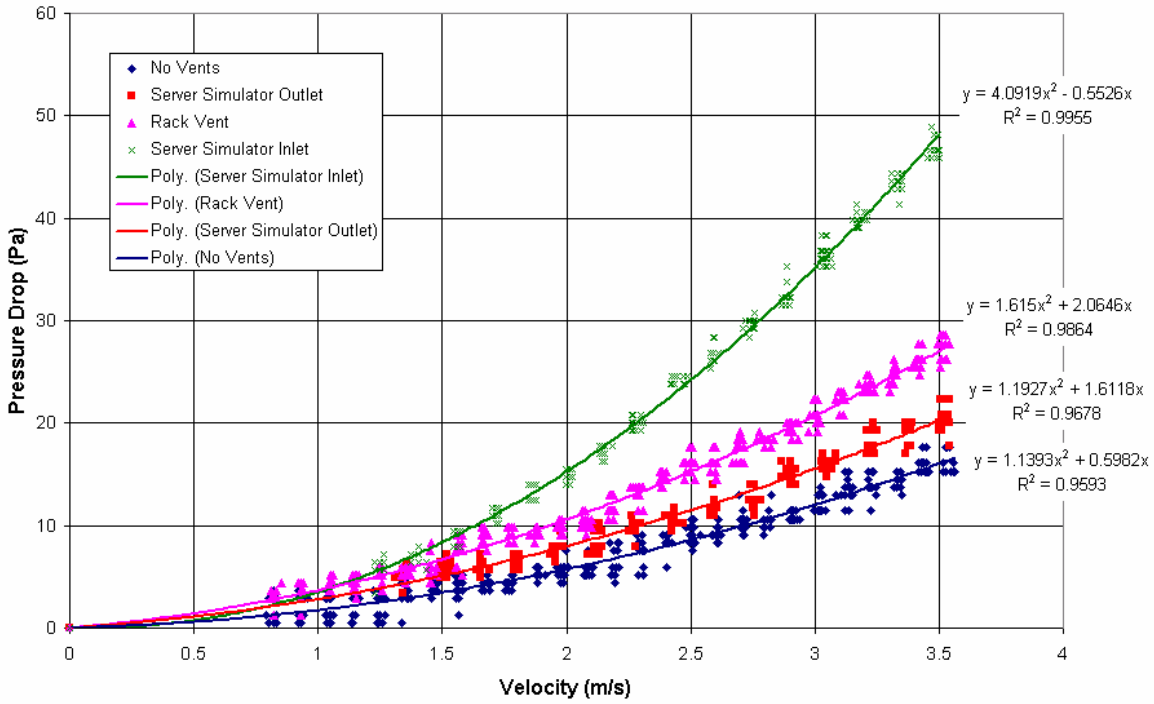

Figure 43: Grille Experimental Pressure Drop vs. Velocity

The experimental pressure drop curves also fit the second-order polynomial form of Equation 3.1. To determine the user inputs, a second-order-polynomial curve fit was applied to each set of data. It is important to note that the grille curves represent the pressure drops across the duct and the grille together. In order to estimate the pressure drops across the grilles alone, the curve-fit of the lone duct was subtracted from each of the grille/duct pressure drop curve-fits. Figure 44 shows the resulting curve fit plots.

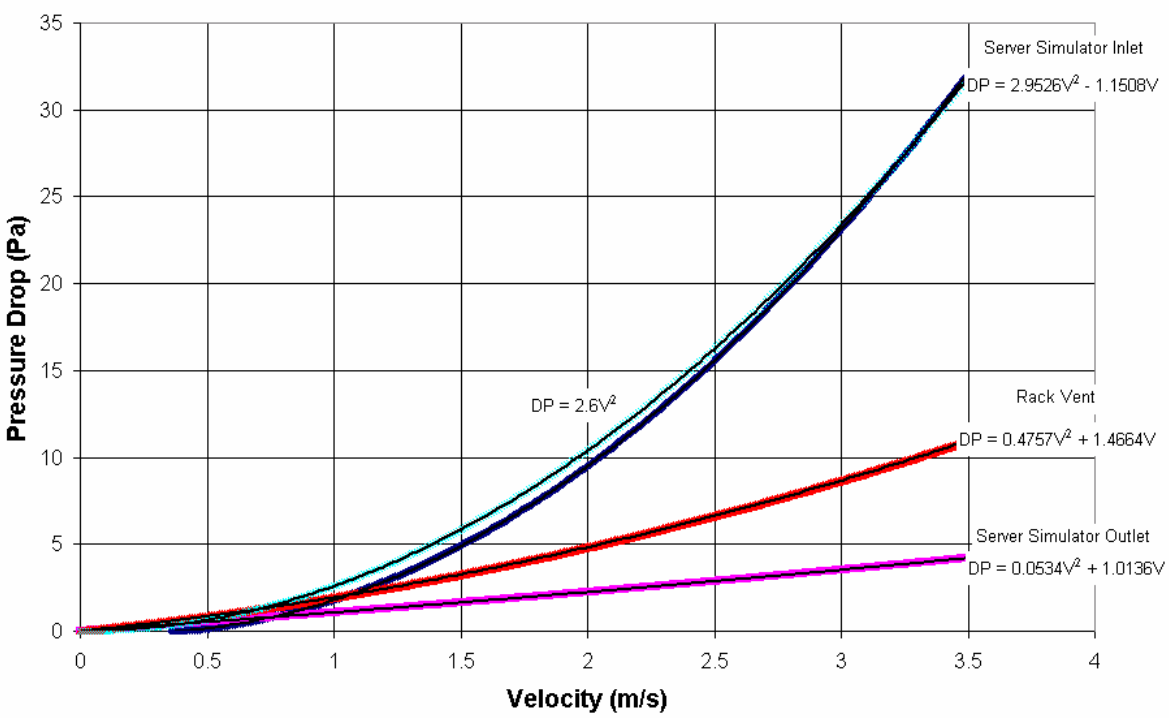

Figure 44: Grille Pressure Drops

The server simulator inlet has the largest pressure drop by far. Note that there are two curves for this grille. The curve with the two coefficients was found by directly subtracting the pressure drop curve of the empty duct from the pressure drop curve of the rack grille mounted to the duct, as previously described. Since the input coefficients in Fluent are confined to positive numbers, a second curve was fit to the server simulator inlet data, with only one coefficient. The second curve was then used to provide the user inputs.

Figure 45 shows a comparison between the experimental and approximate analytical models. The figure illustrates the necessity to test the grilles experimentally, as the analytical model over-predicts the pressure drop across the server simulator inlet grille by greater than 100%.

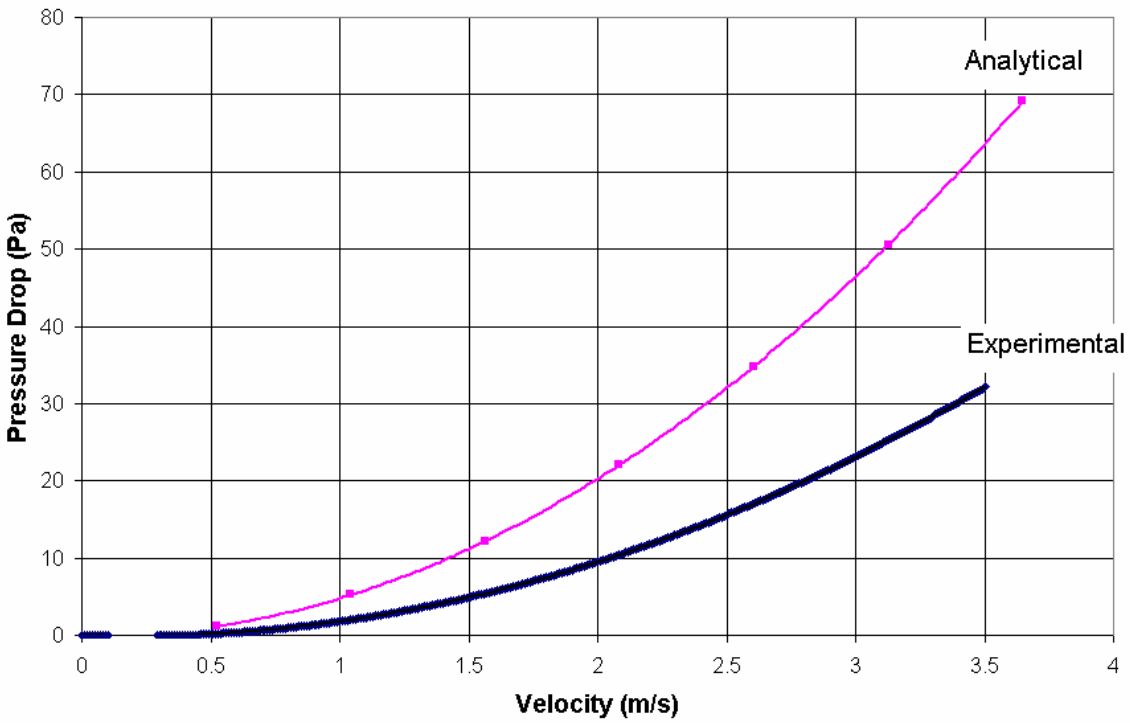

Figure 45: Server Simulator Inlet Grille Pressure Drop Comparison between Approximate Analytical Results and Experimental Data

The experimental results for the pressure drops across all grilles were those used as the inputs for the CFD-HT model.

3.3 Fin Bank Modeling

3.3.1 Barriers to Creating a Detailed CFD-HT Model of the Fins

Even within the fin space, the difference in lengthscales prevents modeling the heater and fins in great detail. Each fin is 0.25 in. (0.635 mm.) thick, and there are 56 fins that are 0.2 in. (5 mm.) apart. The bank of fins surrounding each heater cover a space that is 1.375 in. (35 mm.) wide, 2 in. (51 mm.) deep, and 10.6125 in. (270 mm.) high. The three decades of lengthscales inhibits the ability to even model a single bank of fins surrounding one heater.

In reality, each pair of fins forms a channel through which air may flow. Fluids moving through a channel typically experience what is known as Poiseuille flow, where the velocity profile is parabolic. A turbulent velocity would take on a similar shape but

would have fluctuations over time. The heat transfer coefficient is dependent on the velocity profile; therefore, to accurately model heat transfer through a channel, one would need to solve for the velocity profile first.

To accurately model channel flow in a CFD-HT solver, however, a large number of mesh volumes is required between the channel walls. To illustrate this, consider the following: A two-dimensional channel was created in GAMBIT and Fluent. The left side was given an inlet mass flow rate of 0.01 kg/s, and the top and bottom walls were given a heat flux of 100 W/m^2. The number of mesh volumes between walls was varied to determine the effect on the velocity and temperature profiles. Figure 46a shows the temperature profile with two elements between channel walls, and Figure 46b shows the temperature profile with sixty-four elements between walls.

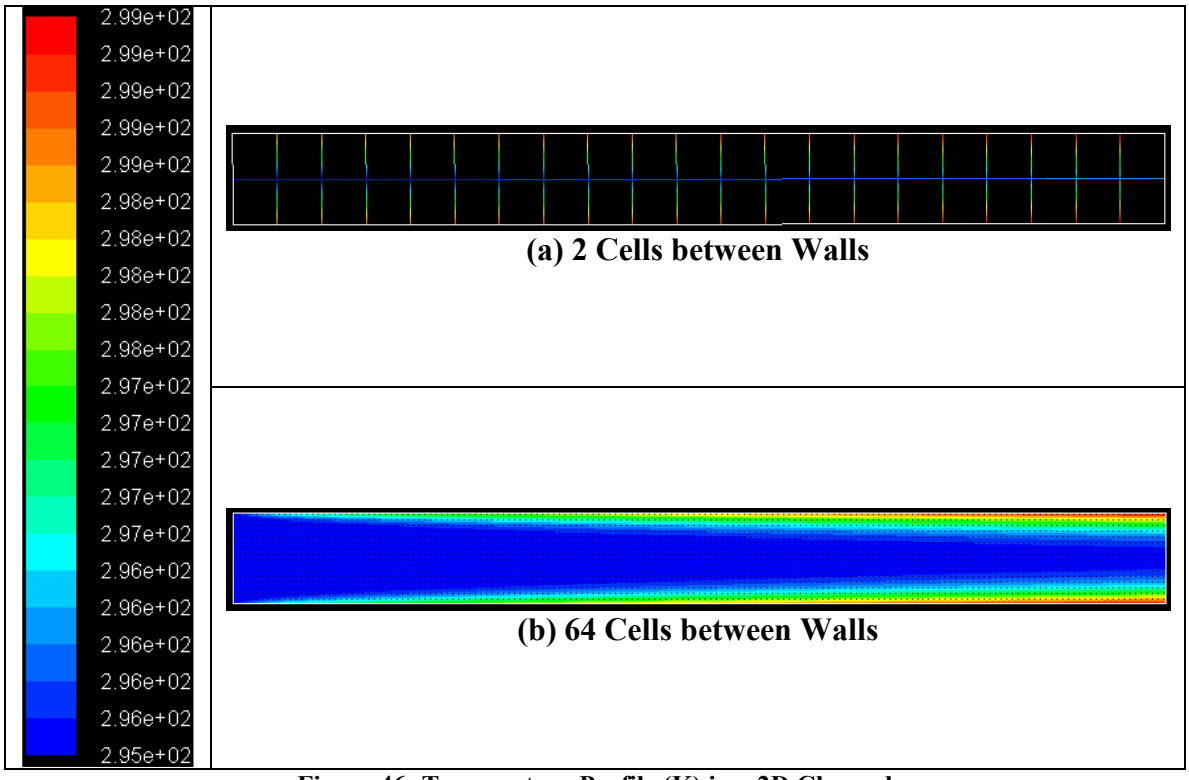

Figure 46: Temperature Profile (K) in a 2D Channel

Figure 47 further illustrates the effect of increasing the number of elements between walls on the average outlet temperature and velocity.

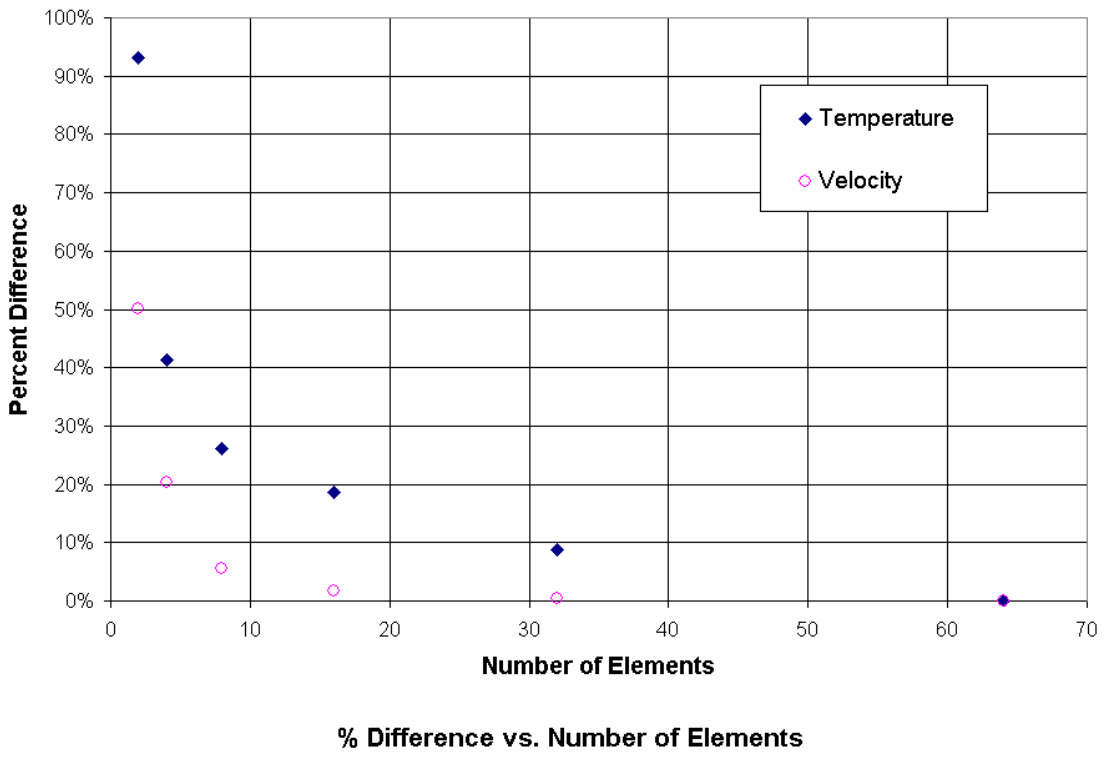

Figure 47: Effect of Increasing the Number of Elements between Walls in a 2D Channel

The temperature % difference was found by comparing the ΔT (temperature change from the inlet to the outlet) of each mesh to the one containing 64 elements between walls. The outlet velocities were also compared to the 64-element solution. The plot shows that for a 2-dimensional channel, at least 32 elements are required to give an average outlet temperature and velocity within 10% of the 64-element model.

It is important to note that the previous case neglects the wall thickness. In order to model the conduction heat transfer, the fins themselves would have to be discretized, resulting in an even larger mesh. Therefore, the first effort to model the bank of fins surrounding the heaters was to model each fin as an infinitesimally-thin face (See Figure 48).

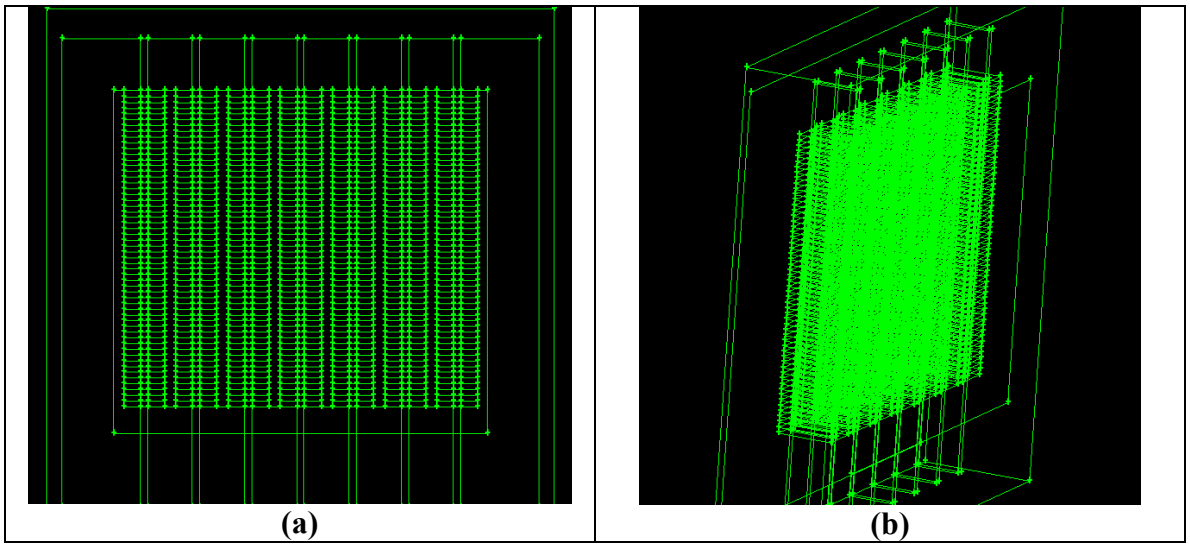

Figure 48: Face-Fin Model (a) Front View (b) Isometric View

The fin faces were each given a thickness of 6.35 mm (0.25 in.) in Fluent. A mesh study was performed on the heater space alone to determine what mesh size would be required to produce "mesh-independent results" (meaning the solution does not change with increasing number of nodes).

A mesh-independent solution was never reached for the heater space. In fact, a mesh with more than two elements between fins required too much memory for the CFD-HT solver to even run. Because an accurate convection heat transfer model would require a much larger mesh, the representation of fins in a system-level model is impractical and unnecessary, and other methods of representing fins banks should be explored.

3.3.2 Porous Media Fin Model

In order to get detailed temperature values for the heaters and fins, a very fine mesh is required at that level. In this study, however, heater temperatures and velocity profiles between fins are not of significant importance. The purpose of the cabinet-level compact CFD-HT model is to obtain overall system pressure drops, outlet velocities, and outlet temperatures as a function of the boundary conditions. Therefore, a more compact model of a fin bank (or heat sink) should be used for a model at this scale. A fin bank in a

system-level model need only be represented as a "black box" object with equivalent thermal and flow resistances. This is the essence of a porous media model.

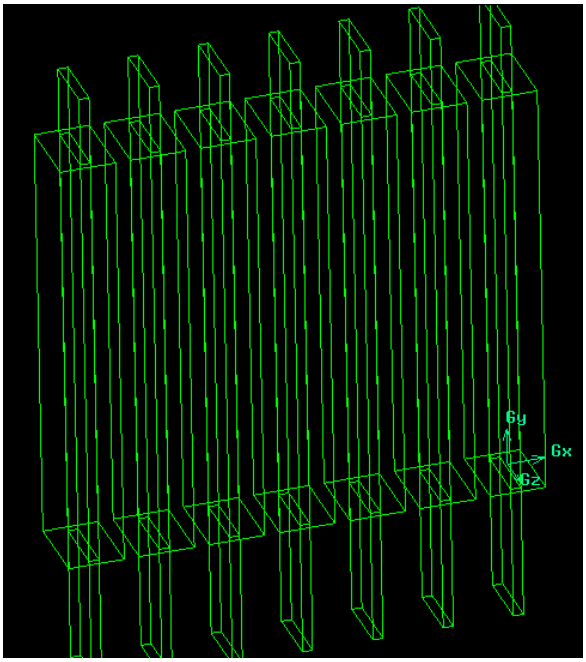

Figure 49: Porous Media Model of Heaters and Fins

Figure 49 shows the geometrical porous media model for the fins used in the system-level compact CFD-HT model. A porous media model is much like the porous jump model used for grilles (and discussed in section 3.2). The basic equation is as follows [30]:

$$S_i = -\left(\sum_{j=1}^{3} D_{ij} \mu \upsilon_j + \sum_{j=1}^{3} C_{ij} \frac{1}{2} \rho \upsilon_{mag} \upsilon_j \right) \tag{3.9}$$

S_i is a pressure drop source term (pressure drop per unit length actually) to be used in the i^{th} momentum equation. D and C are coefficient matrices. The first term on the right hand side of Equation 3.9 is derived from Darcy's law, and the second is the inertial loss term.

The source term may also be represented as

$$S_i = -\left(\frac{\mu}{\alpha} \upsilon_i + C_2 \frac{1}{2} \rho \upsilon_{mag} \upsilon_i \right) \tag{3.10}$$

where μ is the viscosity, α is the permeability, υ is the velocity, C_2 is the inertial resistance factor, and ρ is the density.

The energy transport equation (refer to Equation A.4) is still solved in a porous media region, but the conduction flux term uses an effective thermal conductivity, and the transient term is modified slightly as well (although this study does not involve transients). The porous media energy equation is the following [30]:

$$\frac{\partial}{\partial t}\left(\gamma\rho_f E_f + (1-\gamma)\rho_s E_s\right) + \nabla \bullet \left(\vec{\upsilon}\left(\rho_f E_f + p\right)\right) = \nabla \bullet \left(k_{eff}\nabla T - \left(\sum_i h_i J_i\right) + \left(\bar{\tau} \bullet \vec{\upsilon}\right)\right) + S_f^h \tag{3.11}$$

where E_f is the total fluid energy, E_s is the total solid medium energy, γ is the porosity, S^h_f is the fluid enthalpy source term, and k_{eff} is the effective thermal conductivity of the medium. The effective thermal conductivity of the porous medium is

$$k_{eff} = \gamma k_f + (1-\gamma)k_s \tag{3.12}$$

where k_f and k_s are the thermal conductivities of the fluid and solid, respectively. Also, J is the diffusion flux, h is the sensible enthalpy, and τ is the stress tensor [30].

It is important to point out the shortcomings of a porous media model – especially when applied to a fin bank or heat sink model. For example, a porous media model's effect on the turbulence field will only be approximated. Additionally, the porous media model assumes a constant pressure drop over the length of the fin, which is calculated as the total pressure drop divided by the length. The pressure will then decrease linearly over the fin. In reality, the largest pressure drop will occur at the entrance of the fin bank. As a result, the pressure drop predictions could be skewed. Lastly, because the pressure and velocity profiles are misrepresented, the convection heat transfer coefficient will change, and this may cause a misrepresentation of the temperature distribution across the solid regions and the fluid downstream of the porous medium.

3.3.3 Determination of Fin Pressure Drop Characteristics

To simulate a porous medium in Fluent, the user must input the solid and fluid material properties – along with the porosity – for a calculation of the thermal conductivity. In addition, for each direction, one must input both the viscous resistance coefficient, $1/\alpha$, and the inertial resistance coefficient, C_2 (from Equation 3.10).

Experimental Determination

To determine both of these coefficients experimentally, the airflow test chamber was used. The experimental duct was again mounted to the inlet of the main chamber; however, the duct was modified. Two Plexiglas sheets were placed at a distance of 3.5 cm (1.375 in.) apart, and the spaces outside this interior channel were then plugged with foam to prevent any air from flowing around (instead of through) the space that contained the bank of fins. Because the pressure drop of the fins alone was needed, a piece of Plexiglas with the same dimensions of the heater was placed in the middle of the duct. This was done to ensure that the addition of the fin bank would not alter the flow pattern significantly enough to throw off the results. After the pressure drop was found as a function of the average approach velocity (just like with the grilles), a four inch section of a heater and fins was then placed in the center of the duct, and the pressure drop was again found for varying approach velocities. Figure 50 is a photograph of the heater and fins in the experimental pressure-drop duct.

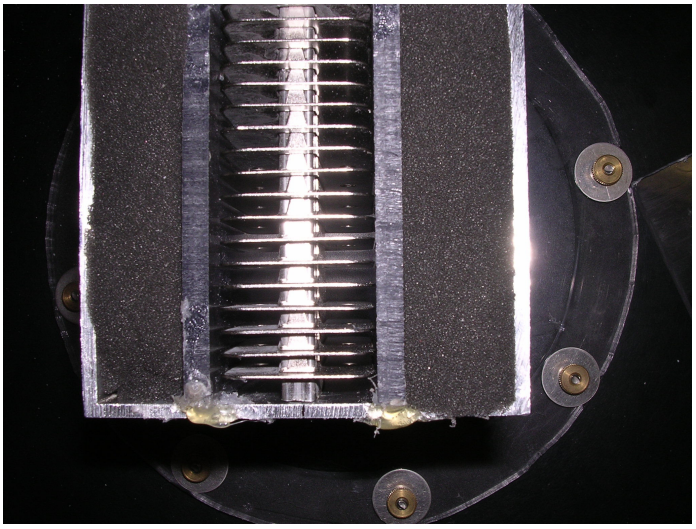

Figure 50: Photographic Illustration of Fin Pressure Drop Measurements

Figure 51 shows the measured pressure drop across the duct with and without the fins.

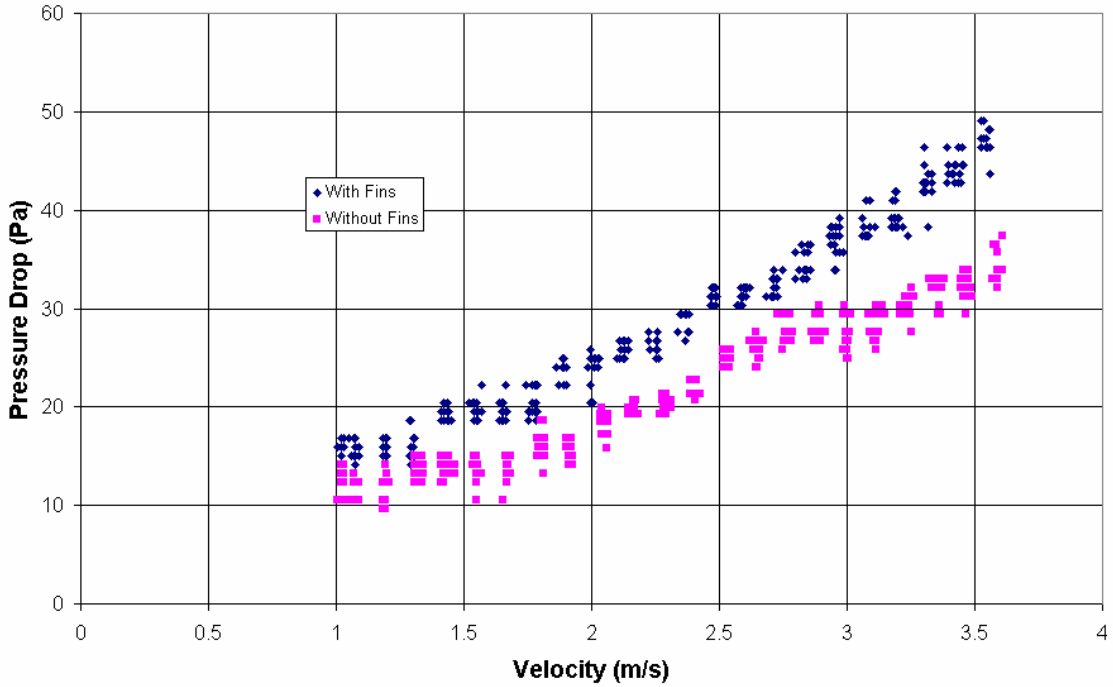

Figure 51: Experimental Pressure Drop with and without Fins

The curve-fit of the pressure drop across the duct and heater was then subtracted from that of the duct, heater, and fins (Refer to Figure 54 on page 80 for the results).

Detailed CFD-HT Modeling of a Portion of a Heater

To determine the pressure drop another way, detailed CFD-HT models of a portion of the heater and fins were created. First, a model of a single fin was created. The fin and small heater portion were placed in a 4 in. long, 1.75 in. wide duct. The top and bottom of the duct represented the mid-plane between fins. The side planes of the duct represented the mid-planes between heaters; therefore, all of the boundaries were set as symmetric borders.

To ensure that the one-fin model could be used to accurately represent an array of fins, a model of a larger portion of the heater was created. This model contained 10 fins in a 4 in. long, 1.75 in. wide duct. Again, the boundaries were set as symmetric borders. Figure 52 shows the two CFD-HT models.

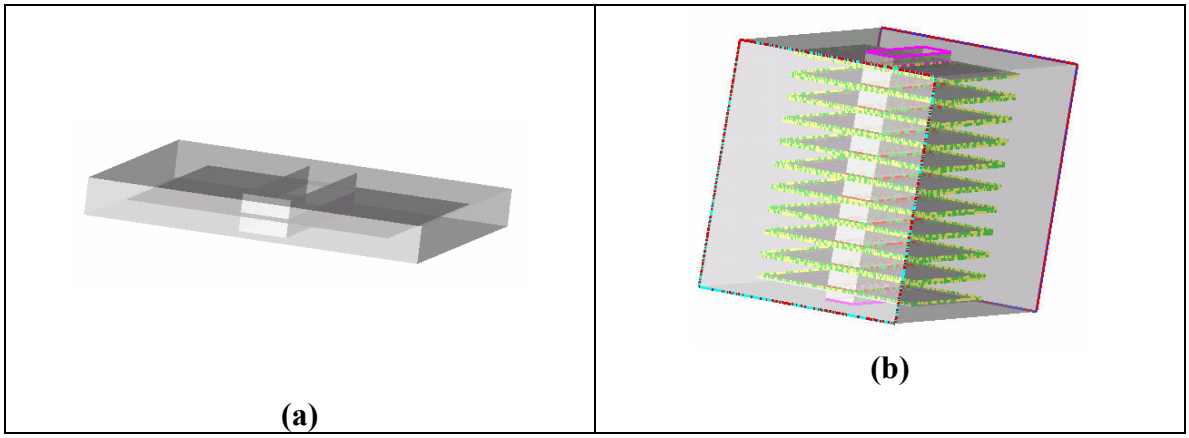

Figure 52: Detailed CFD-HT Model of (a) One Fin (b) Ten Fins

For each case, the inlet velocity was set at a uniform value, and it was varied from 0.5 m/s to 3 m/s. The pressure drop was then found across the duct for each inlet velocity. Figure 53 gives the results of the two detailed fin models along with the measured pressure drops across the heater, fins, and duct.

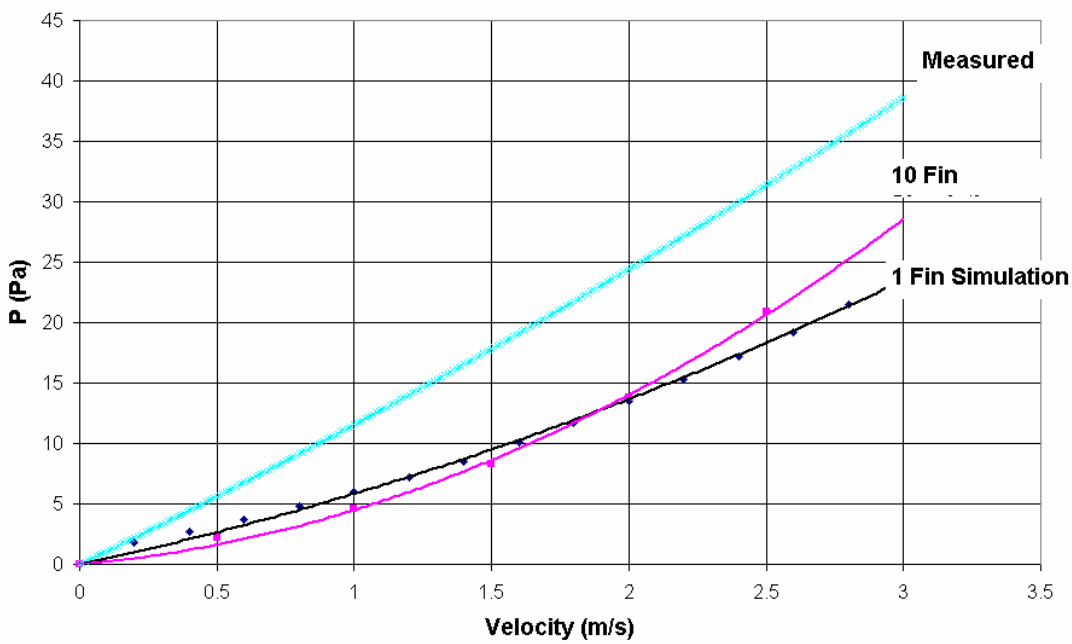

Figure 53: Simulated Fin Pressure Drop Curves

The 10-Fin and 1-Fin simulations agree closely with one another. The simulated pressure drops, however, are in general much lower than the measured fin pressure drops. It should be noted though that the measured values will have additional frictional pressure losses from the duct. In order to find the pressure drop across the fins alone (in order to provide a more accurate comparison with the measured data), the 10-Fin simulation was run again, but without a heater. The results are shown in Figure 54.

Notice that below are the curve-fit results of two experimental runs. The first set of data was taken across a 1.6 in. nozzle, while the second run was taken across the 2 in. nozzle. This was done to try and quantify the uncertainty involved in the conversion from nozzle plate pressure drop to air flow rate. The results show that there is a systematic error involved in this conversion, as the air flow values from the first and the second runs differed by approximately 25%. If the relationship between the nozzle pressure drops and the air flow rates provided by the manufacturer were accurate, then the data should be independent of which nozzle is open, and the two curves should have been much closer than 25%. It is important to point out that the data are repeatable if a set is taken under the exact same conditions (See Figure 57 on page 83).

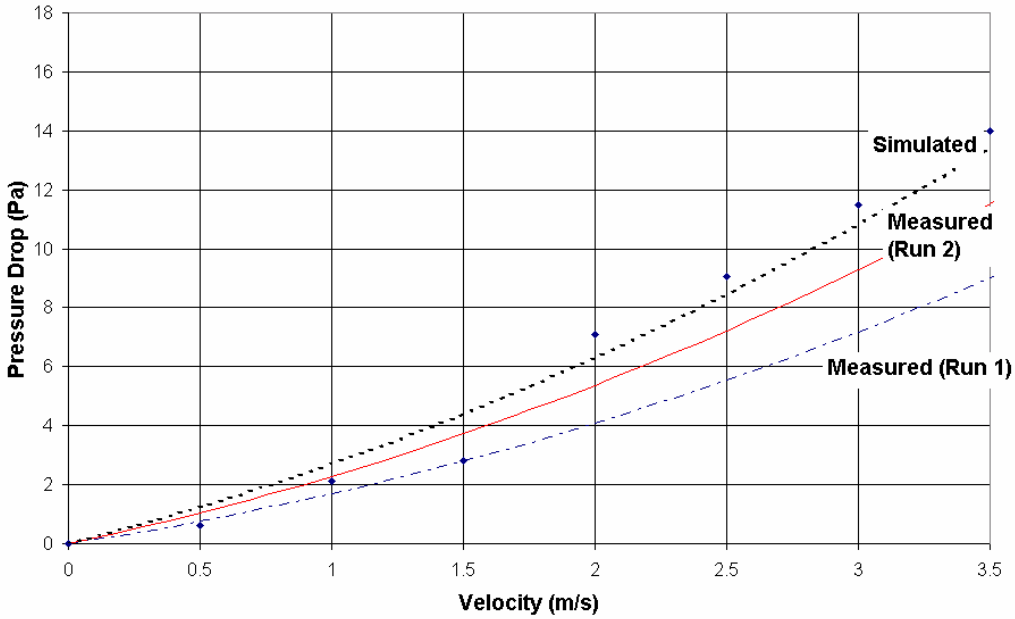

Figure 54: Simulated and Measured Fin Pressure Drops

The 10-Fin model predicts the pressure drop to be slightly larger (as much as 22%) than the measured pressure drops. The differences could be due to a number of factors. First, there could be measurement uncertainties. Also, there could be uncertainties in the curve-fitting. Lastly, the frictional pressure drop in the CFD-HT model could have been over-predicted. Another source of discrepancy could be that the actual approach velocity profile (in the experimental case) probably resembled Poiseuille flow, whereas the approach velocity was uniform in the simulations. Lastly, the turbulence model used in the simulations could have had a significant effect on the pressure drop.

The coefficients were derived from all three fin pressure drop equations. Table 4 gives the possible coefficients.

Table 4: Porous Media Coefficient Values

Method	$1/\alpha$ (m^{-2})	C_2 (m^{-1})
Experimental (Run 1)	1.472×10^6	11.33
Experimental (Run 2)	2.059×10^6	13.08
Simulated (10 Fins)	2.914×10^6	11.46

Although there is about a 25% difference between the three different pressure drop curves, the fin pressure drop does not account for a significant source of the overall system pressure drop. The CFD-HT results presented in the next chapter are those that employed the second experimental run coefficients. Chapter 4 discusses the effect of varying the porous media coefficients on the overall system-level results.

3.4 Fan Modeling

3.4.1 Fan Modeling Basics

A fan is essentially an electrical device with rotating blades that creates an increase in pressure that induces an air flow. The fan model in Fluent does not involve the detailed geometries of the fan blades, and therefore it cannot solve for the detailed flow patterns. Instead, a flow rate is solved for based on an empirical relationship between the head (pressure rise) of a fan and the flow rate (or velocity). The operating point of the system – or the system's flow rate in other words – is determined based on where the fan performance curve meets the system pressure drop curve.

A fan in Fluent is always modeled as an infinitesimally-thin face. Since the fan performance curve includes any pressure drops across the fan volume itself, it is unnecessary to represent the fan volume in a system-level model. In fact, if the fan were modeled as a full cylinder or cube rather than a face, there would be an inaccurate addition of frictional pressure drop; therefore, the fan volume should not be included unless absolutely necessary to represent flow patterns.

The fan performance curve comes in the following form [30]:

$$\Delta p = \sum_{n=1}^{N} f_n \upsilon^{n-1} \tag{3.13}$$

One need only input the coefficients of each polynomial term, f_n. If necessary, the fan swirl can be modeled as well. The fan swirl components may be visualized in Figure 55.

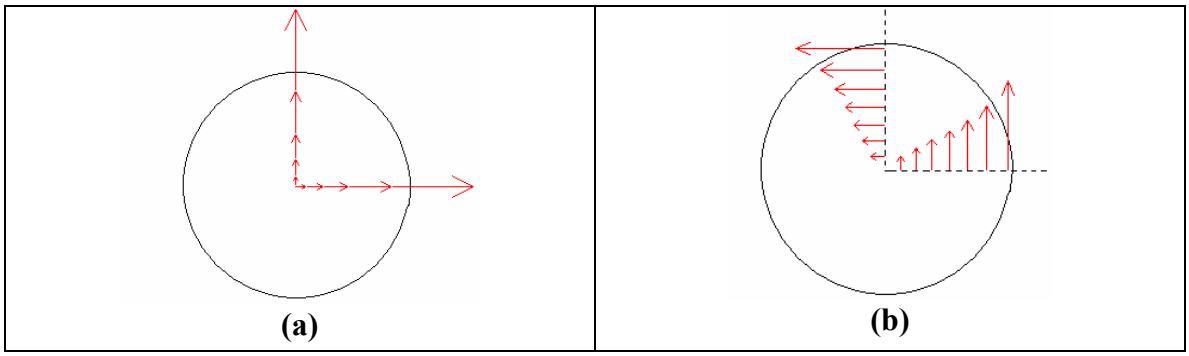

Figure 55: Fan Swirl (a) Radial and (b) Tangential Velocity Components

The two swirl components (tangential and radial velocity) may be functions of the radial position. The components are input using the following two equations [30]:

$$U_\theta = \sum_{n=-1}^{N} f_n r^n \quad -1 \le N \le 6 \tag{3.14}$$

$$U_r = \sum_{n=-1}^{N} g_n r^n \quad -1 \le N \le 6 \tag{3.15}$$

where f_n and g_n are coefficients of a polynomial. The fan swirl was not found empirically or analytically in this study. The effect of the fan swirl will be discussed in the next chapter as well.

3.4.2 Experimental Determination of Fan Performance Curves

The manufacturer only provides a fan performance curve for one specific electrical input. The server simulator, on the other hand, allows one to change the amount of power supplied to the fan. For each dial setting, the fan performance curve will be different.

To find the fan curves at every dial setting, an AA1751HB-AT fan was mounted to the front of the airflow test chamber (Refer back to Figure 27b on page 45). The electrical wiring was detached from a fan in the server simulator and reattached to the fan to be tested. This ensured that the electrical input to the test fan equaled the electrical input of the fan as if it were mounted in the server simulator. For each dial setting, the static pressure and pressure drop across the nozzles were recorded at varying counter

blower frequencies. Each data point was taken over a 2 minute interval. The nozzle pressure drop was then converted to air flow rate using the manufacturer's charts. Figure 56 shows the results of the fan test.

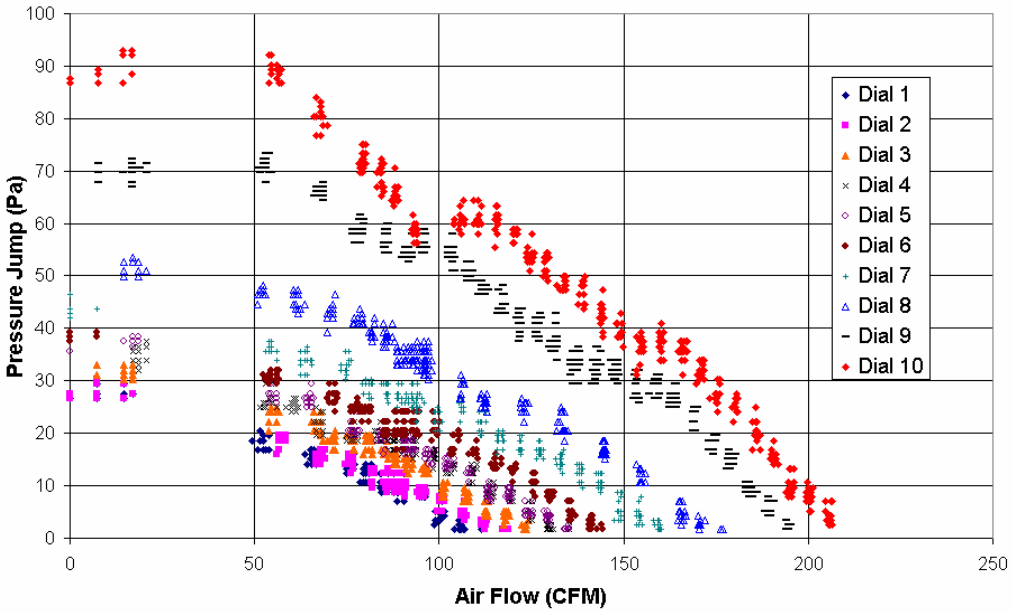

Figure 56: Fan Performance Curves for All Server Simulator Dial Settings

Figure 57 is a comparison between the measured fan performance curve found at the highest dial setting (the power to each fan at the largest dial setting should be 115 V, 60 Hz) and the fan curve that was supplied by the manufacturer.

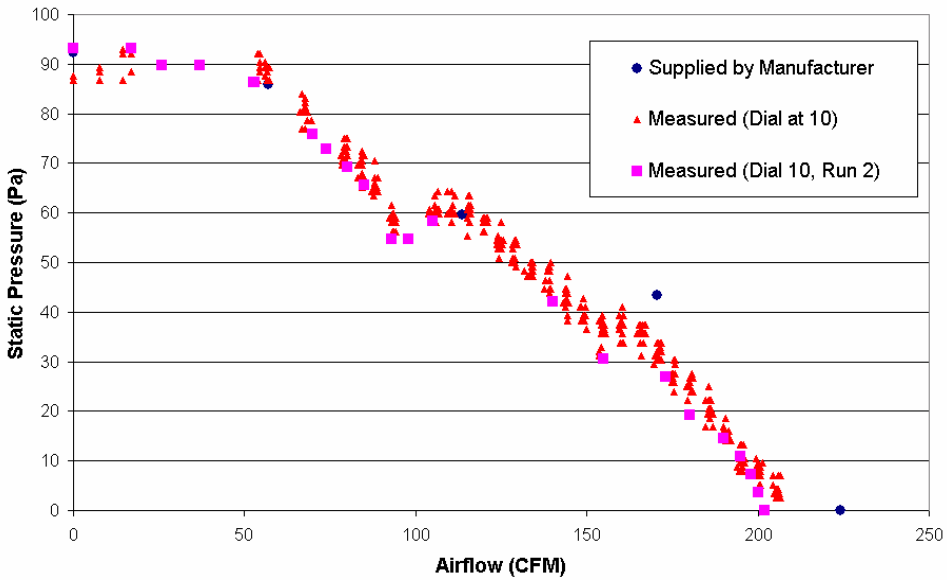

Figure 57: Comparison between Measured and Supplied Fan Performance Curve

The shutoff static pressure of the fan measured at Dial 10 is approximately 4% different than that provided by the manufacturer. Also, the unobstructed fan air flow rate was measured to be within about 6% of the manufacturer's curve. The previous figure also demonstrates the repeatability of measurements. A second set of data was taken at the highest dial setting – with the same nozzles open as the previous set of data. That curve follows very closely with the other one. Despite the fact that the fan curve at the highest dial setting is close to the predicted manufacturer fan curve and the measurements are repeatable, it should be noted that this does not imply accuracy. As was already noticed in testing the fin pressure drops, there may be as much as 25% uncertainty in the CFM values because one must rely on the relationship between the pressure drop across the nozzle plate and the air flow rate to be accurate.

The performance curve must be input as a function of the velocity (Equation 3.13). The air flow rates may be converted to velocities by dividing by the fan cross-sectional area. The fan may be modeled with or without a hub in the center. The results of both will be presented in the next chapter. If the fan is modeled with a hub in the center, the cross-sectional area of the fan is equal to 26.18 in.^{2} (169 cm.^{2}). Figure 58 and Figure 59 show the results for all dial settings. The equations in the top right of the figures are the user inputs for the model.

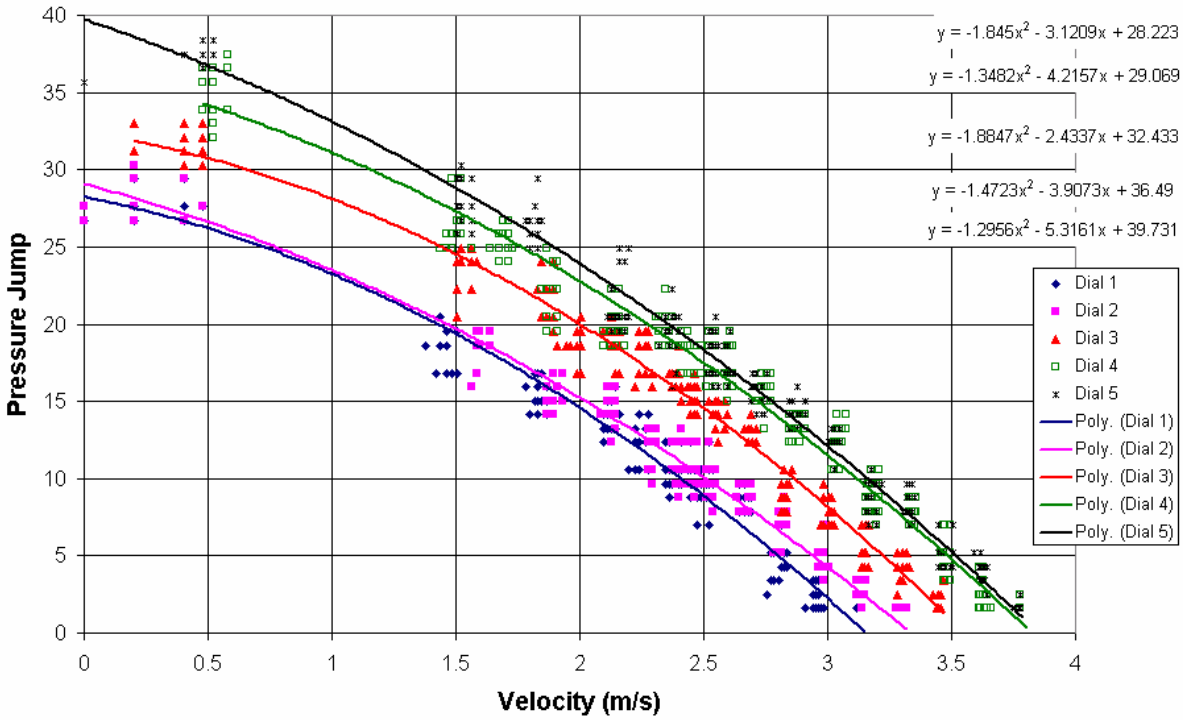

Figure 58: Pressure Jump vs. Velocity for Low Dial Settings

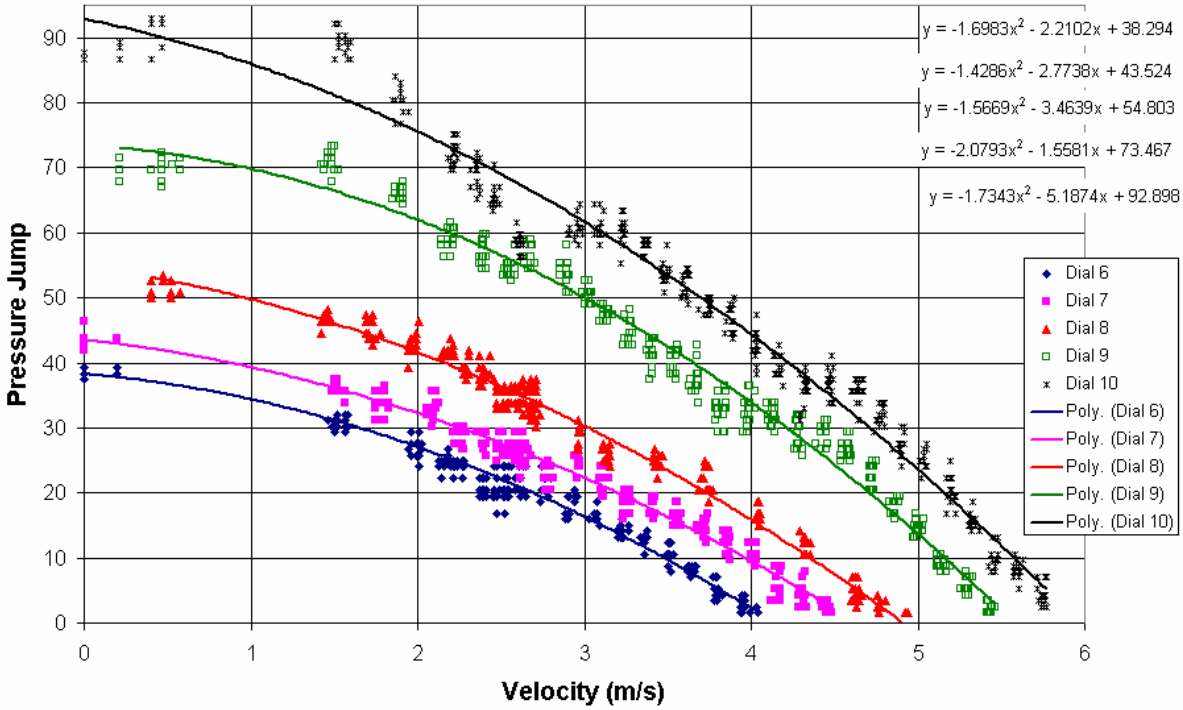

Figure 59: Pressure Jump vs. Velocity for High Dial Settings

If no hub is modeled, the area of the fan is 34.47 in.^{2} (222 cm.^{2}). Table 5 shows the user inputs for the fan performance curves – with and without a hub.

Table 5: User Inputs for Fan Performance Curve Modeling

Dial Setting		Fan Performance Curve
2	**Hub**	$\Delta p = -1.3482\upsilon^2 - 4.2157\upsilon + 29.069$
	No Hub	$\Delta p = -2.3382\upsilon^2 – 5.5517\upsilon + 29.069$
5	**Hub**	$\Delta p = -1.2956\upsilon^2 – 5.3161\upsilon + 39.731$
	No Hub	$\Delta p = -2.247\upsilon^2 – 7.0009\upsilon + 39.731$
8	**Hub**	$\Delta p = -1.5669\upsilon^2 – 3.4639\upsilon + 54.803$
	No Hub	$\Delta p = -2.7175\upsilon^2 – 4.5617\upsilon + 54.803$

CHAPTER 4

RESULTS AND CONCLUSIONS

In the past, much effort has been made to create compact or reduced-order models of electronics enclosures. Traditionally, detailed CFD-HT models of systems or components have served as the basis of comparison with the compact or reduced-order models. Because detailed CFD-HT models of entire racks have not been possible, the compact modeling work has mostly been done at the component level. A compact model is often created and compared with the detailed model of a component, and eventually the component compact model is implemented into a system or sub-system level CFD-HT model. The issue with this methodology is that it does not take into account any discrepancies that might exist between the detailed component models and the actual physical entities. Also, compact *component* models are often created based on detailed *component* models, rather than on detailed models of components within a system. It is difficult to know whether the compact models of components will cause the system to behave differently than it does in reality. For these reasons, it is absolutely essential that experimental data be used as the bases of comparison with compact or reduced-order electronics enclosure models, rather than detailed CFD-HT models of components or enclosure systems.

A compact CFD-HT model of a single server simulator was created using GAMBIT and Fluent. Additionally, a compact model of a rack sub-system was created by placing the server simulator model with associate plena. The compact CFD-HT models required a number of geometrical assumptions: All wiring was excluded from the model, and some complex geometrical objects (such as the set of controls) were represented as simple cuboid blocks. Also, fans were represented as faces rather than as cylinders with rotational curved blades. Lastly, each bank of fins was represented as a single porous medium, with equivalent pressure drop and heat transfer characteristics. As

a result of the geometrical approximations – most notably the fin porous media model – internal temperature results, such as heater temperatures, are expected to be somewhat inaccurate. There is a tradeoff between detail and feasibility. At the enclosure level, approximations must be made at the smaller levels.

Empirical inputs were required for many of the boundary conditions: A fan performance curve was required at each of the ten dial settings. Also, the pressure drop as a function of air flow rate was needed for the heater fins, the server simulator inlet and outlet grilles, and the rack inlet and outlet grilles. Because none of the boundary condition information was provided, experiments had to be performed to determine all of these values. Because of not only the geometrical approximations, but also the uncertainties in the measurements of the empirical inputs, one might expect some discrepancy between the simulation model and the actual physical entity.

Outlet air temperature and velocity measurements were used for comparison with the compact CFD-HT model of the server simulator. Detailed outlet temperature measurements were taken at the outlet of the server simulator using fine grids of thermocouples. PIV was used to obtain the outlet velocities of the server simulator.

This chapter will present the results of the compact CFD-HT model of the server simulator. The compact CFD-HT model will be compared with experimental data of outlet temperature and velocity. Similarly, some representative outlet temperature results will be presented for the rack sub-system model. The chapter will attempt to explain the discrepancies between the simulated and experimental model. This will illustrate the need for one to use experiments as the basis of comparison – rather than using detailed CFD-HT models alone. Based on comparisons between experimental and modeled outlet temperatures and velocities, the chapter will conclude with recommendations for future work.

4.1 Server Simulator Parametric Simulation Results

4.1.1 Effect of Fan Geometry on Results

Modeling Fans as Square or Circular

The fan can be modeled as a rectangular or as a circular face, or as something in between. Often, in rack-level CFD-HT models, a fan is represented as a single rectangular face, without a hub; the advantage of which is that it allows one to mesh the system more easily. A rectangular fan may be meshed with rectangular volumes, and a hex-type mesh may be used for the system, which is much less computationally expensive than other mesh types.

According to previous studies, however, the geometry of a fan must mimic the actual geometry as closely as possible, especially when the fan is upstream of intricate electronic components. A square fan may not accurately capture the velocity profiles. To determine whether or not the fan could be modeled as a square face rather than a circular one, the server simulator was modeled with two different fan geometries: First, all of the four fans were modeled as square faces, without any kind of hub in the center. Next, the four fans were modeled as circular faces, without a hub as well.

The following results are for a fan dial setting of 8 and with heaters 1, 4, 6, and 7 dissipating heat. This amounts to a total 3250 kW of heat dissipated. Figure 60 gives a visual definition of the **outlet plane**, the **horizontal mid-plane**, and the **horizontal plane through a set of fans** at which results will be presented.

Figure 61 gives the results from the two fan models. Images (a) and (b) are contour plots of the z-direction velocities at the outlet of the server simulator using the square and circular fan models, respectively. Images (c) and (d) show the outlet temperature profiles for the square and circular fan models, respectively.

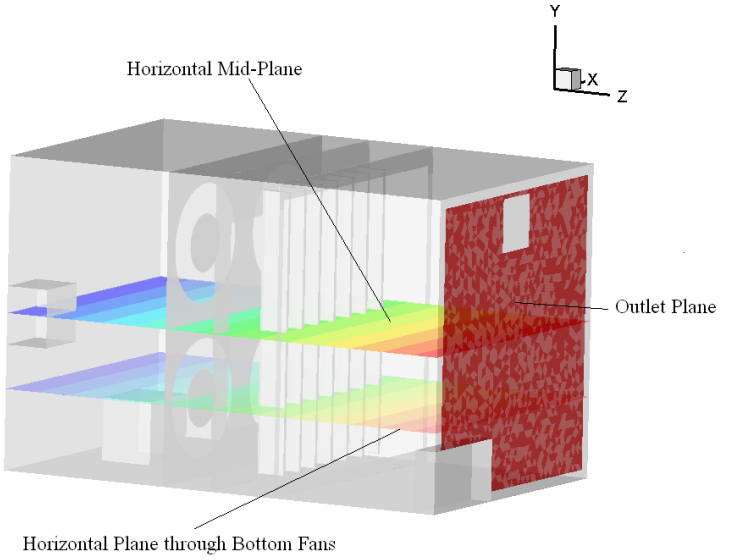

Figure 60: Visual Definition of Simulation Result Planes

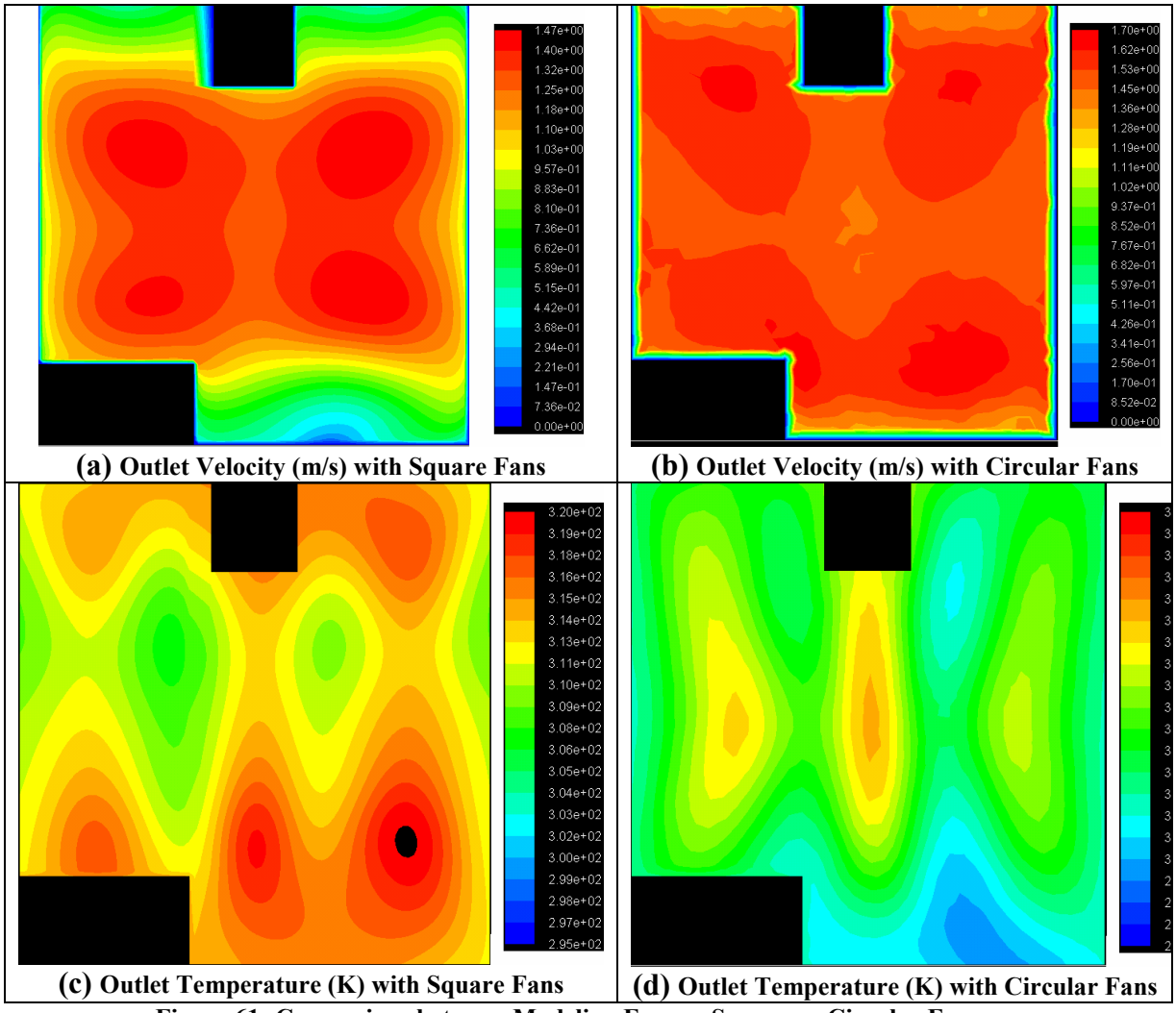

Figure 61: Comparison between Modeling Fans as Square or Circular Faces

Based on both the qualitative and quantitative differences at the outlet of the server simulator, the figure illustrates that a square fan cannot be used to represent a circular one in the server simulator model.

Modeling Fans with or without a Hub

The fan can also be modeled with or without its center hub. As previously mentioned, in larger-scale models, fans are often represented as square and without a hub. As was just demonstrated, a square fan cannot be used in this model; therefore, the fan will be modeled as a circular face. To determine whether it is necessary to model the hub as well, consider the following two figures. Figure 62 shows a comparison between the outlet temperature profiles of a model with and without a hub, and Figure 63 gives a comparison of the z-direction velocity profiles at the server simulator outlet plane.

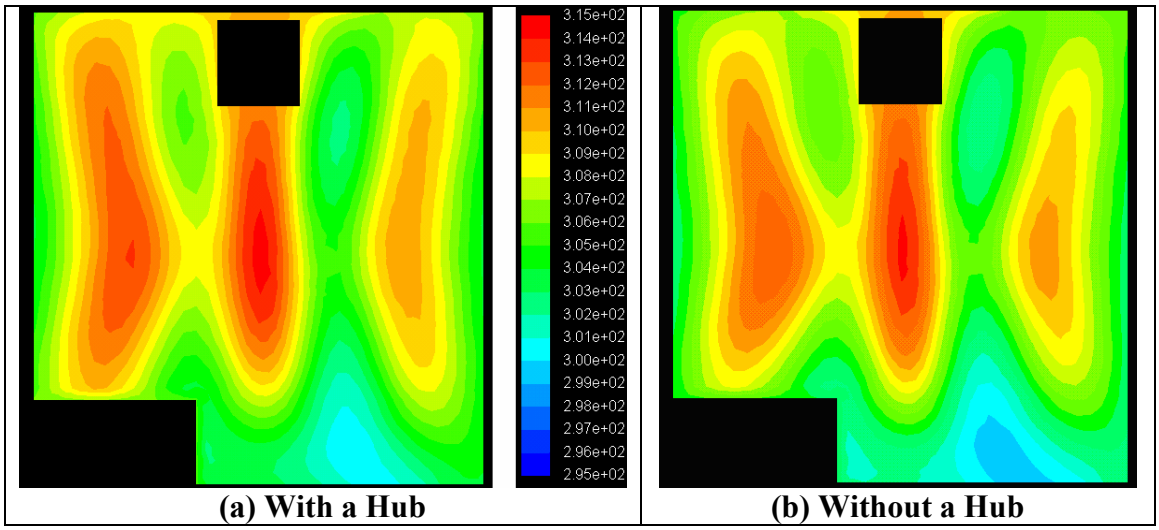

Figure 62: Server Simulator Outlet Temperature Profiles (K) for Two Circular Fan Models

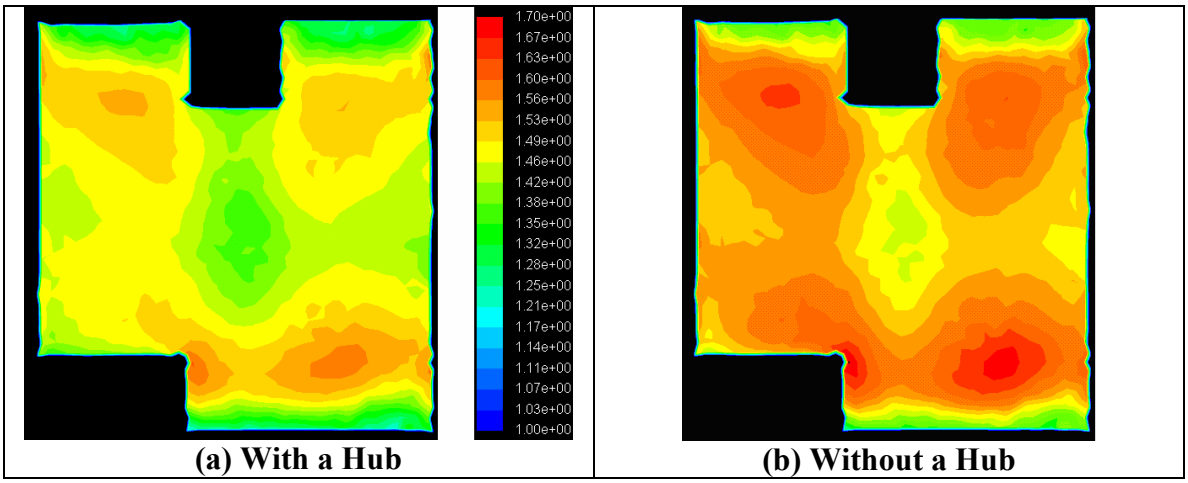

Figure 63: Server Simulator Outlet Velocity Profiles (m/s) for Two Circular Fan Models

Both simulations were run with the same ambient conditions, a uniform temperature at 295.37 K at the inlet, and a uniform pressure (atmospheric). The average outlet temperature of the server simulator with the hub is 307.72 (a mean ΔT of 12.35 K), whereas, the average outlet temperature without the hub is 307.04 K (a mean ΔT of 11.67 K). The difference between the two mean temperature differences is about 5.5%.

The average outlet velocity of the server simulator with the hub is 1.36 m/s and the mass flow rate is 0.261 kg/s, whereas without the hub the velocity is 1.44 m/s, and the mass flow rate is 0.276 kg/s. The difference between the mass flow rates of both models is about 5.8%.

Although the temperature and air flow rate discrepancies are both less than 6%, and the outlet profiles are very similar in the two models, the hub will be modeled in further presented results. Because of the specific geometry of this system, modeling the fan without the hub does not reduce the required mesh size by a significant amount.

4.1.2 Some Representative Server Simulator CFD-HT Results

Simulations were run for four different heat loads at four different fan dial settings. The standard k-ε turbulence model was applied, and the default coefficients were used ($C_{1\varepsilon} = 1.44$, $C_{2\varepsilon} = 1.92$, $C_{\mu} = 0.09$, $\sigma_k = 1.0$, $\sigma_{\varepsilon} = 1.3$). The inlet temperature was

set at a uniform 295.37 K (22.22°C, 72°F) in order to compare the simulation results with experimental results. Also, both the inlet and outlet gage pressures were assumed to be approximately 0. In addition to the pressure drop-velocity input for the grille, the inlet requires the approximate turbulent parameters at the inlet. If one were to assume an inlet velocity through a rectangular pipe that is the size of the holes in the metal grid of the inlet, one would find Re to range from about 1,000 to 2,000. Since the flow is downstream of a perforated plate, and the flow upstream of the inlet grille is undisturbed and under-developed, an inlet turbulence was assumed, and the intensity was estimated using the following relation [30]:

$$I \approx 0.16(\mathrm{Re}_D)^{-1/8} \tag{4.1}$$

The hydraulic diameter used was 6.3 mm (0.25 in.), based on the size of the inlet metal grid opening size. The turbulence intensity, based on this hydraulic diameter, was approximately 5%.

So, for each of the four dial settings, four different heat load combinations were run through the simulations. Table 6 shows the different combinations. Refer back to Figure 15 on page 30 for a definition of the heater number.

Table 6: Heat Load Combinations Simulated

Heat Load	Heaters	Switches
750 W	2, 6	1, 2
1,750 W	2, 4, 6	1, 2, 3
3,250 W	1, 4, 6, 7	2, 3, 5
5,750 W	1, 2, 3, 4, 5, 6, 7	1, 2, 3, 4, 5

Figure 64 gives some representative results of the different server simulator outlet temperature profiles for each of the four heat loads. The plots in that figure are all for the same dial setting (2).

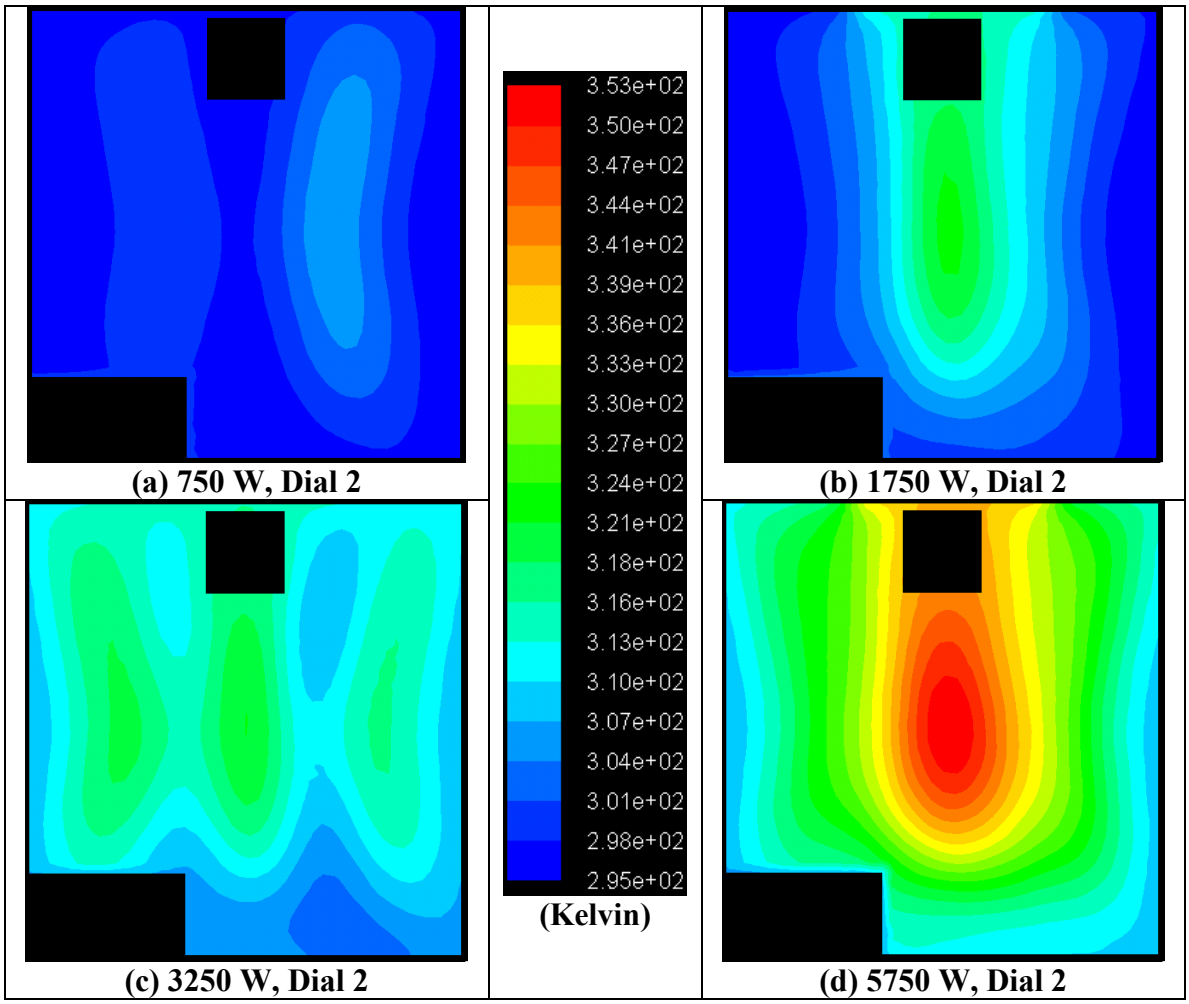

Figure 64: Simulated Server Simulator Outlet Temperature Profiles (K) for Different Heat Loads

Images (a), (b), and (c) make qualitative sense in terms of the shapes of the temperature profile at the outlet. The areas of high temperature correspond to locations that are directly behind the solid blocks that are dissipating the heat. Notice that the maximum temperatures between (b) and (c) are approximately the same (around 322 K). This implies that there is not much lateral heat transfer. What is interesting is that when the remaining heaters are turned on – the two 1000-W heaters that surround the center one – the maximum temperature increases significantly, to about 353 K (or a ΔT of about 78^{o}C). Figure 65 shows a horizontal slice through the middle of the server simulator (Refer back to Figure 60 on page 90 for a visual explanation of the horizontal mid-plane).

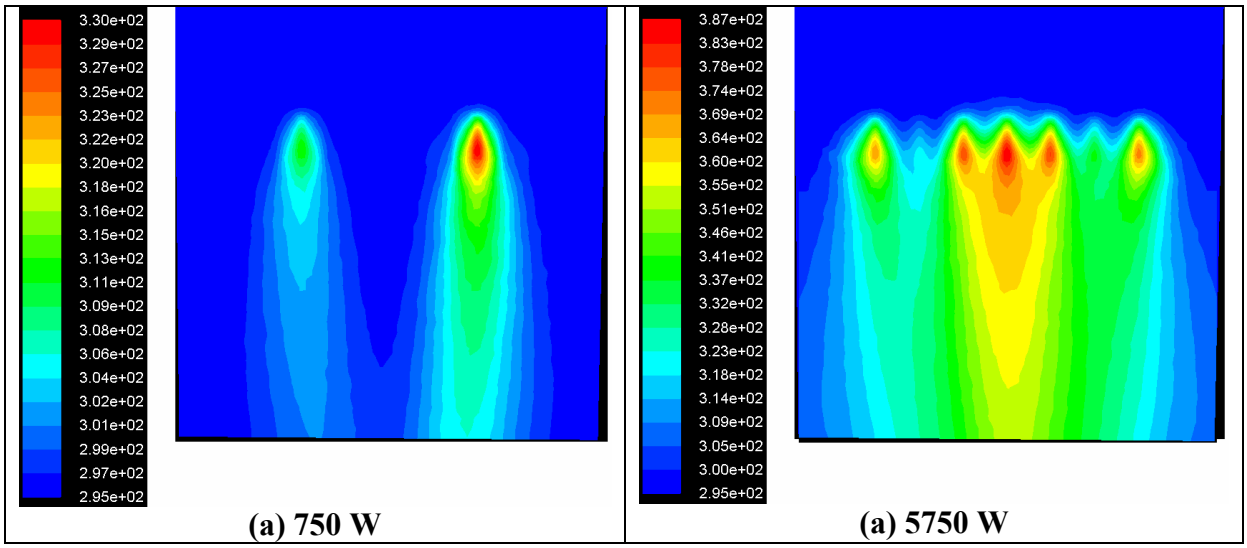

Figure 65: Horizontal Mid-Plane Temperature Profile (K) (Dial 2)

The figure shows that there is in fact some lateral heat transfer in the server simulator. Also, image (a) shows that the high temperatures concentrate almost immediately beyond the heaters.

Figure 66 shows the same horizontal slice through the simulator, but it provides the velocity magnitudes ($\sqrt{\upsilon_x^2 + \upsilon_y^2 + \upsilon_z^2}$). Based on the velocity magnitudes, one may notice that much more air passes through the outside of the server simulator than through the middle. This explains why the temperatures in the middle of the unit are much higher than they are at the outside of the unit, as there is less air flow over the heaters.

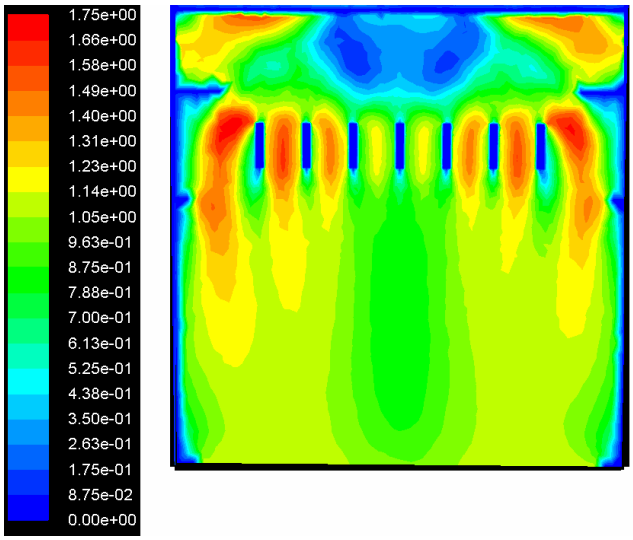

Figure 66: Horizontal Mid-Plane Velocity Magnitude Profile (m/s) of Server Simulator Rear (Dial 2)

It makes sense that the velocity magnitudes are higher on the outside of the heaters because of the flow resistance associated with the heater and fin region. Because the resistance is high relative to the outside, more air will tend to move to those outside regions. Figure 67 further demonstrates the interaction between the fans and the heaters. It shows a horizontal slice through the middle of the bottom fans (Refer back to Figure 60 on page 90). Notice that there is no velocity toward the outlet in the center of the fan. This corresponds to the location of the fan hub. Notice also that the air velocity is much higher at the outside of not only the fin space but also the fan itself. Since there is less resistance on that side of the fan, more air is able to travel through the outside.

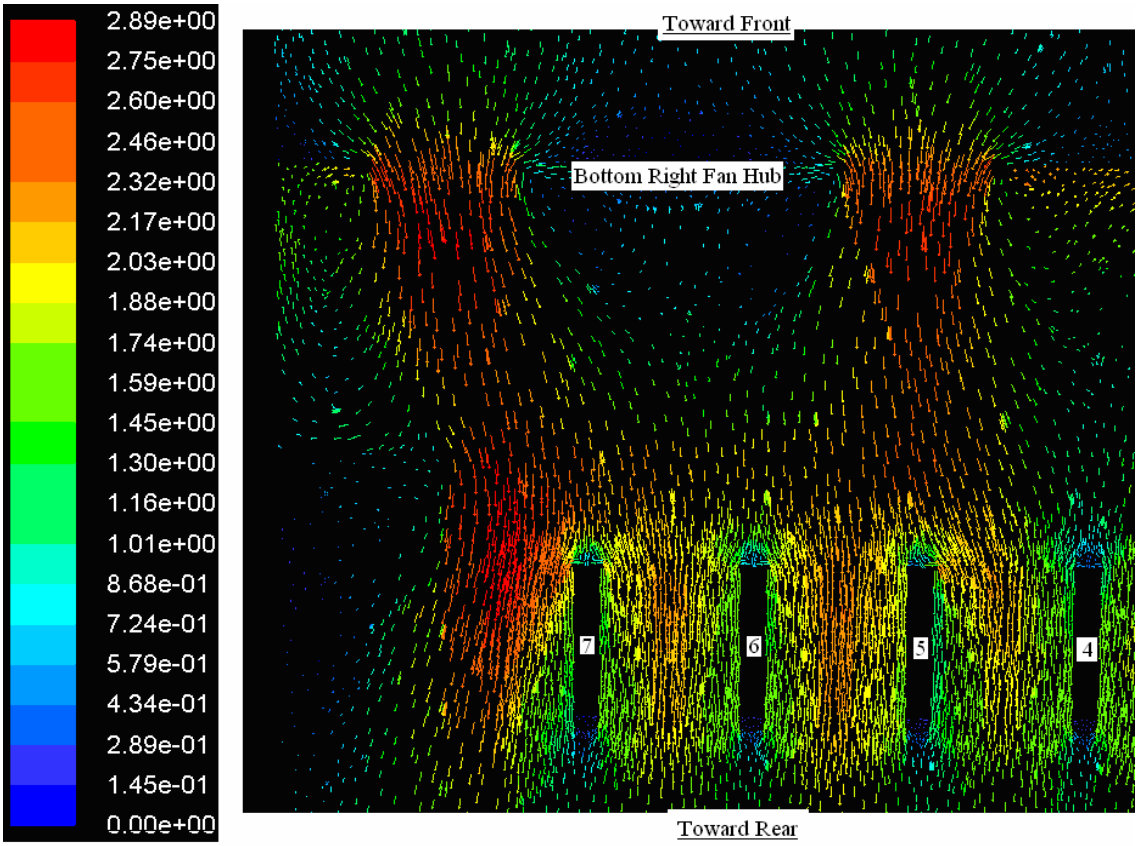

Figure 67: Velocity Vectors (m/s) between Fan and Heaters

Figure 68 gives the z-velocity profile at the outlet at a dial setting of 2.

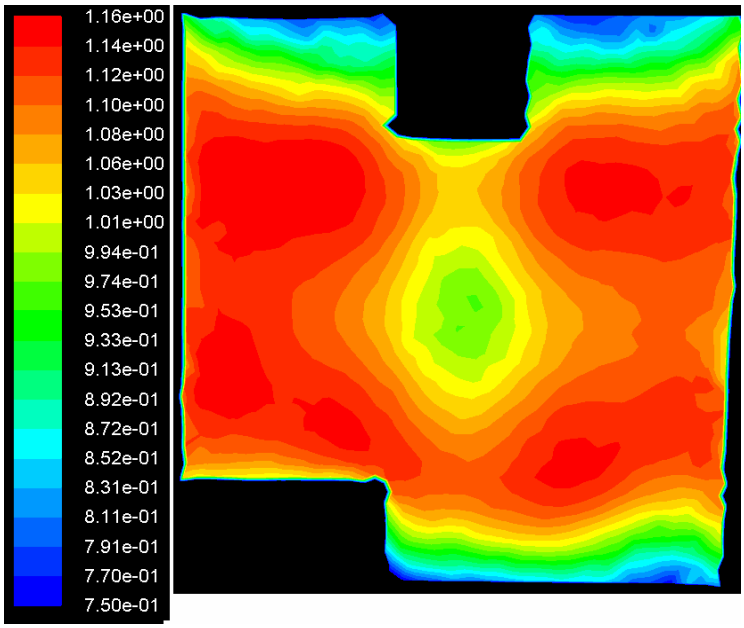

Figure 68: Server Simulator Outlet Z-Velocity Profile (m/s) at Dial 2

The outlet velocity profile makes sense, given that the highest velocities occur at the four quadrants – each one corresponding to the location of a fan upstream of the outlet, and the lowest air flow is in the center of the unit. The fact that the air flow is low at the center also explains why the temperature is higher at the center.

It is important to point out also that increasing the dial setting does not change the velocity or temperature profiles. It does change the magnitudes of the velocities and temperatures, though. The following figure illustrates this. Figure 69 shows the outlet temperature profiles of the server simulator with varying dial settings. A constant heat load of 3,250 W was applied. The figure shows the outlet plane temperatures for dial settings of 2, 5, 8, and 10. It makes sense that increasing the dial setting (which increases the air flow rate) generally decreases both the maximum and the average temperatures.

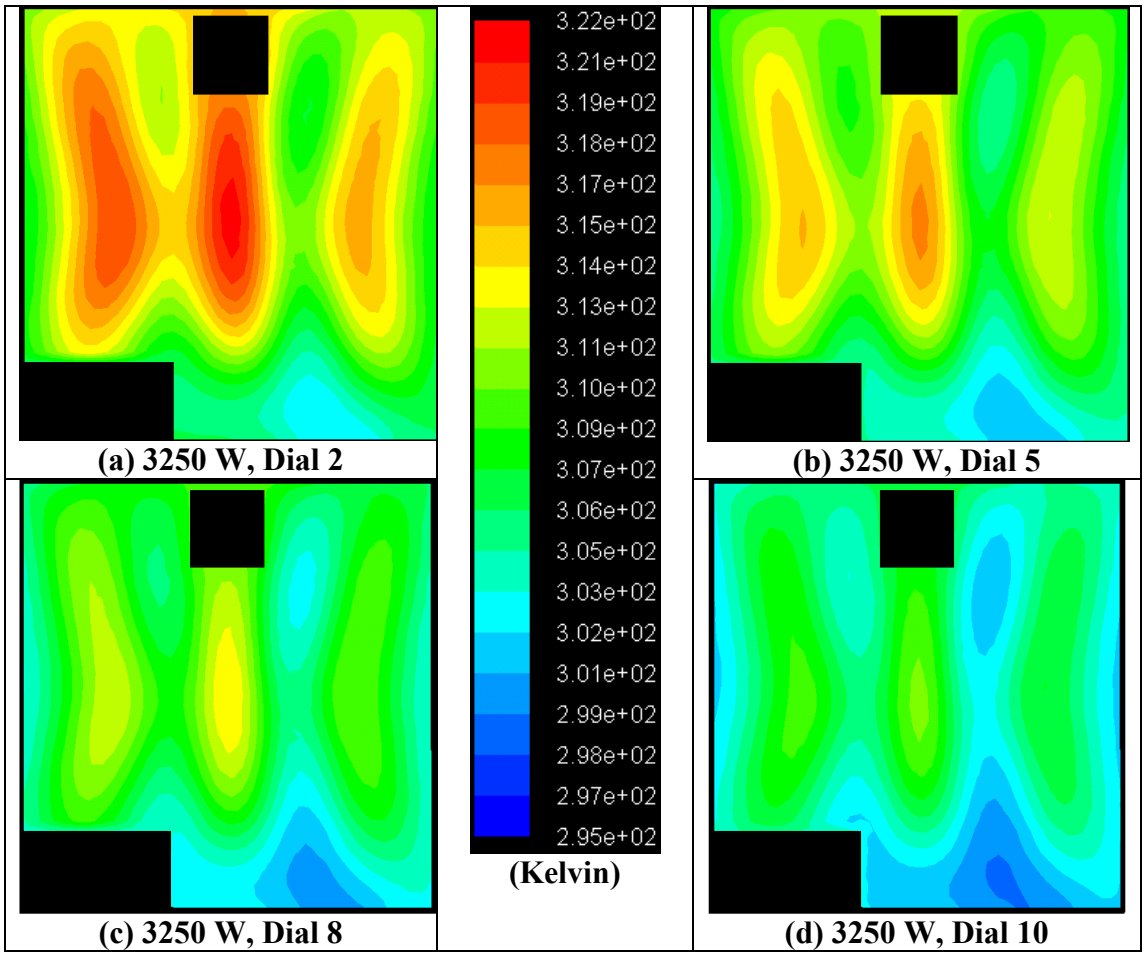

Figure 69: Server Simulator Outlet Temperature Profiles (K) for Varying Dial Settings

Figure 70 is a plot of the relationship between the mean temperature difference – or the difference between the average outlet temperature and the inlet temperature – and the amount of heat dissipated from the unit. The figure shows that the outlet temperature increases linearly with increasing heat load. Figure 71 shows the relationship between mean temperature difference and mass flow rate. The mean outlet temperature decreases approximately linearly with increasing mass flow rate.

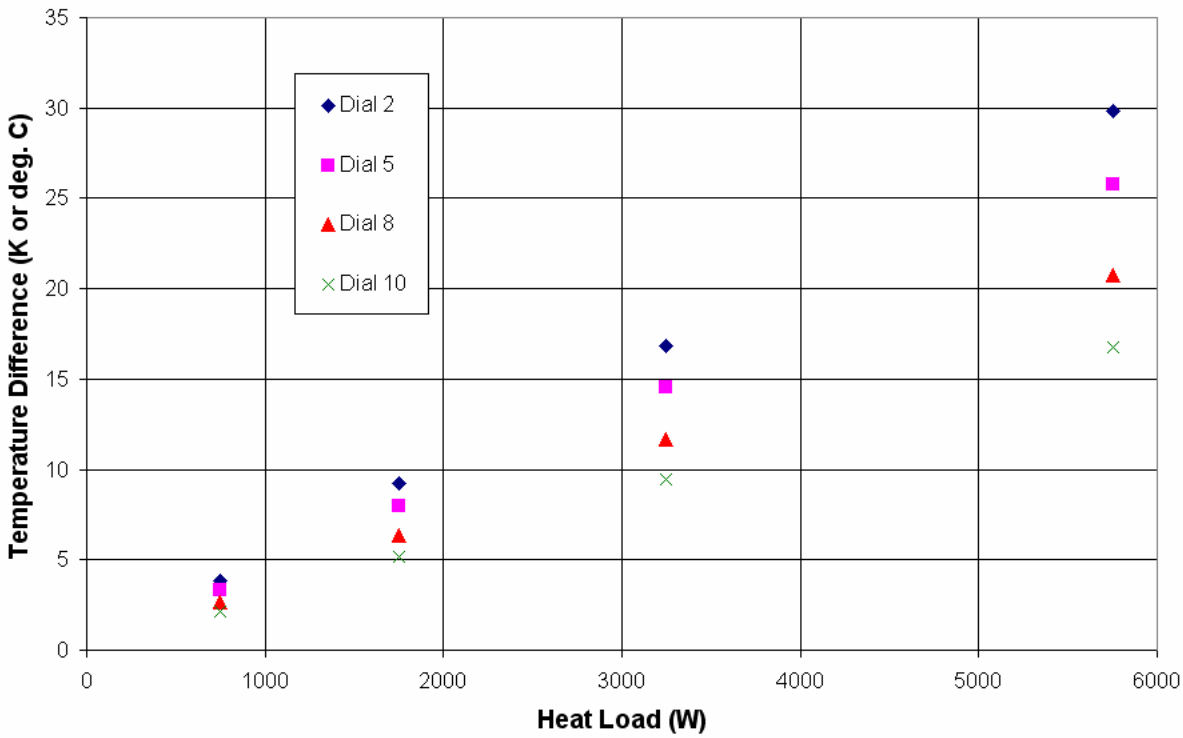

Figure 70: Mean Temperature Difference vs. Heat Load

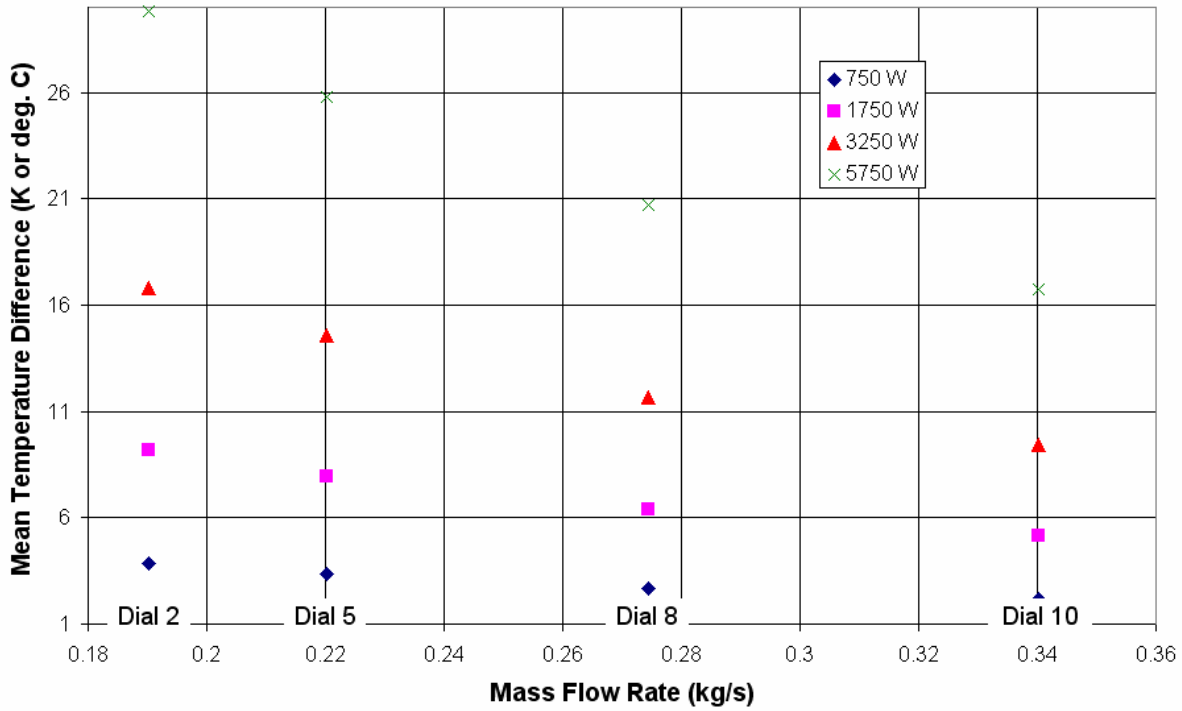

Figure 71: Mean Temperature Difference vs. Mass Flow Rate

Another advantage to using CFD-HT to develop models of an electronics enclosure is the ability to extract internal information that would otherwise be unavailable. Most important in an actual electronic enclosure is the chip temperature. Although the server simulators do not have actual chips, the heater temperature may be of interest. Figure 72 shows the effect of increasing the mass flow rate on the heater temperature difference (the difference between the mean heater temperature and the inlet temperature). The results are for the case when all of the heaters are dissipating heat.

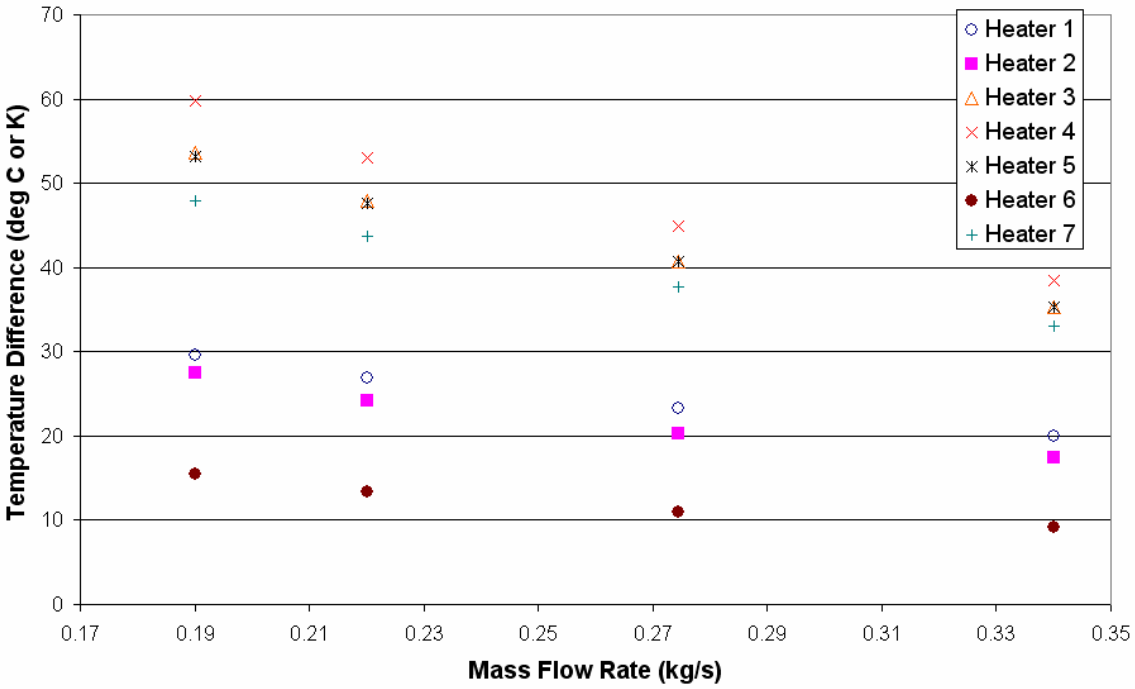

Figure 72: Heater Temperature as a Function of Mass Flow Rate in the Server Simulator

In general, the heater temperatures decrease with increasing flow rate. Also, it makes sense that heaters 3, 4, and 5 are at the highest temperatures. They all dissipate 1,000 W of heat and are located in regions of the lowest air flow. Heater 7 is also in an area of slightly lower air flow, due to the flow resistance upstream caused by the set of controls and downstream by the power input.

4.2 Experimental Results and Comparisons

If one did not have access to the actual enclosure that was modeled using CFD-HT, the conclusion would likely be that the model made physical sense and is an accurate representation of the thermal characteristics. Based on the locations of the fans, it makes sense that the areas of highest air flow would correspond to the quadrants with the fans. Based on this velocity profile, one might expect the temperatures in the middle of the outlet to be slightly higher than the temperatures around the edges. In this case, however, the unit was available, so it could be determined if the velocity profiles and corresponding temperature values were represented accurately in the compact CFD-HT model.

4.2.1 Server Simulator Experimental Results and Comparisons

Figure 73 shows the experimental outlet temperature profile of the server simulator for varying heat loads at the same dial setting (2). Figure 74 is a plot of the mean temperature difference (the difference between the average outlet temperature and room temperature, which is assumed to be 72^{o}F or 295.37 K) as found experimentally.

Figure 75 shows the measured outlet temperature profile of the server simulator under a constant heat load (3250 W – heaters 1, 4, 6, and 7) and different dial settings: 2, 5, and 8. Figure 76 shows the relationship between the experimental mean temperature difference and the mass flow rate found experimentally. The air flow rate was found experimentally using the FlowHood. To find the mass flow rate, an air density of 1.225 kg/m^3 was assumed, and the volumetric flow rate was multiplied by the density.

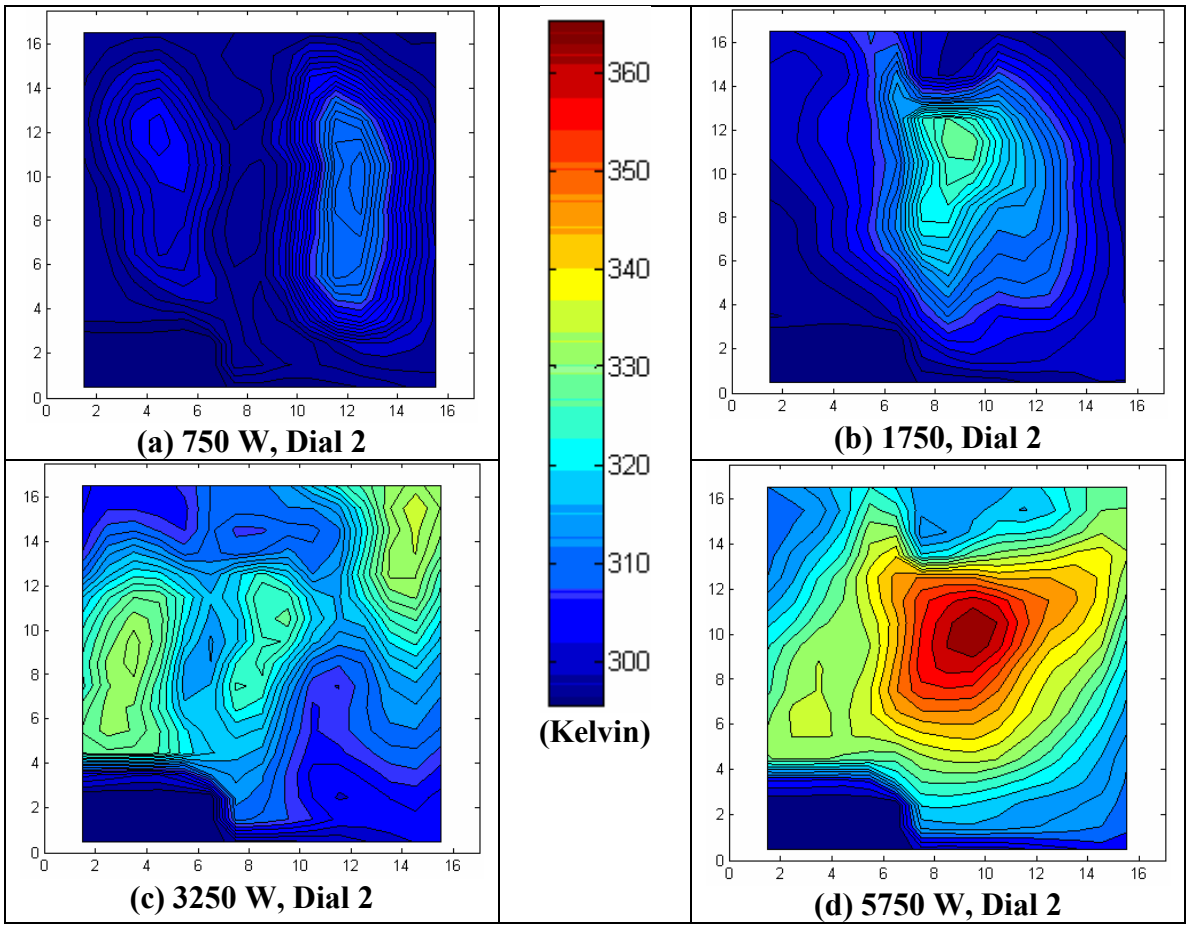

Figure 73: Experimental Server Sim. Outlet Temperature Profiles for Diff. Heat Loads (Dial 2)

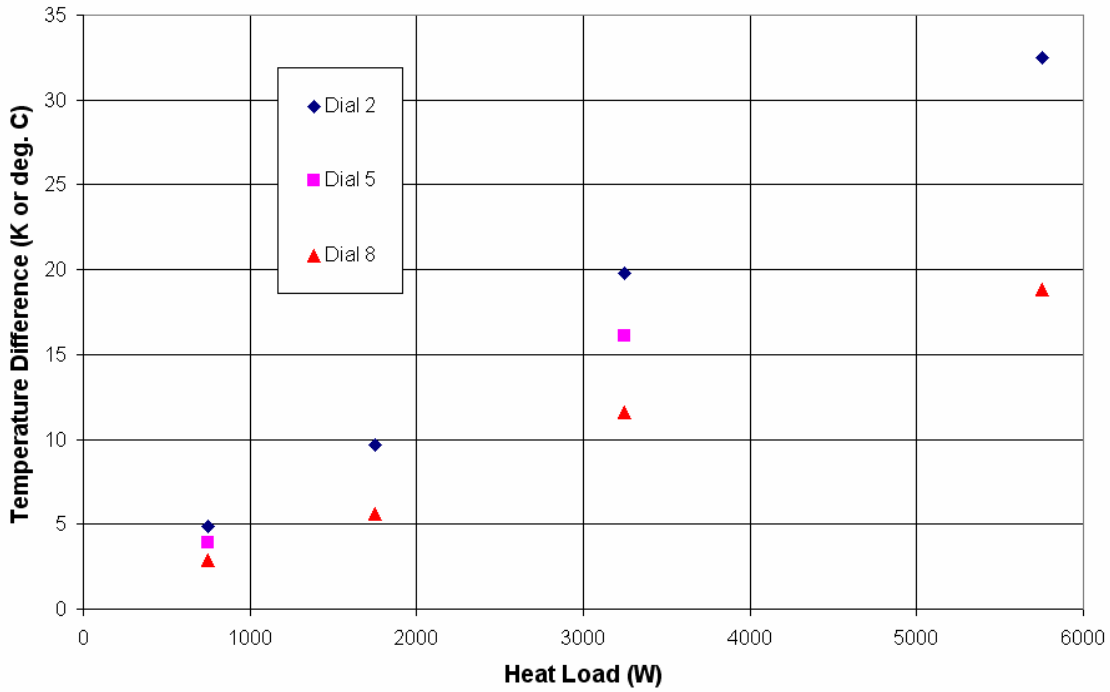

Figure 74: Experimental Mean Temperature Difference vs. Heat Load

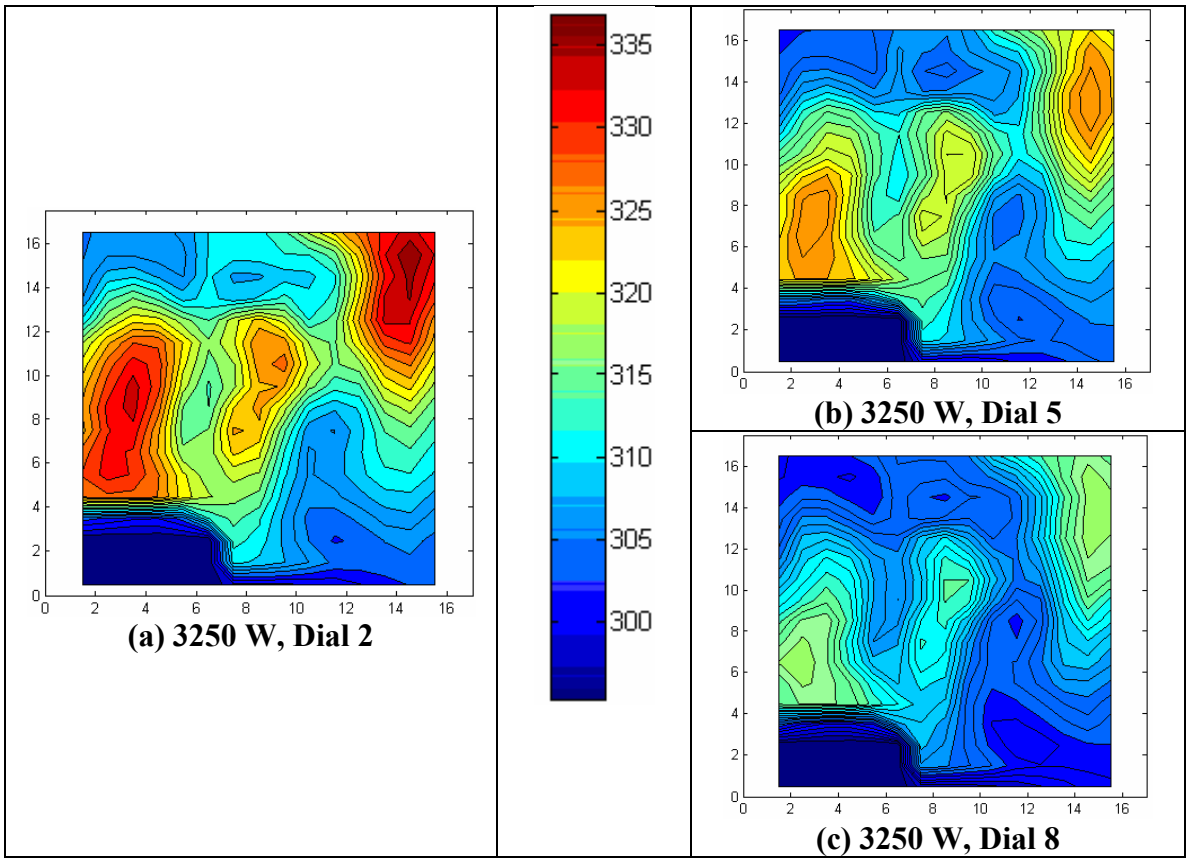

Figure 75: Experimental Server Sim. Outlet Temperature Profiles for Different Dial Settings

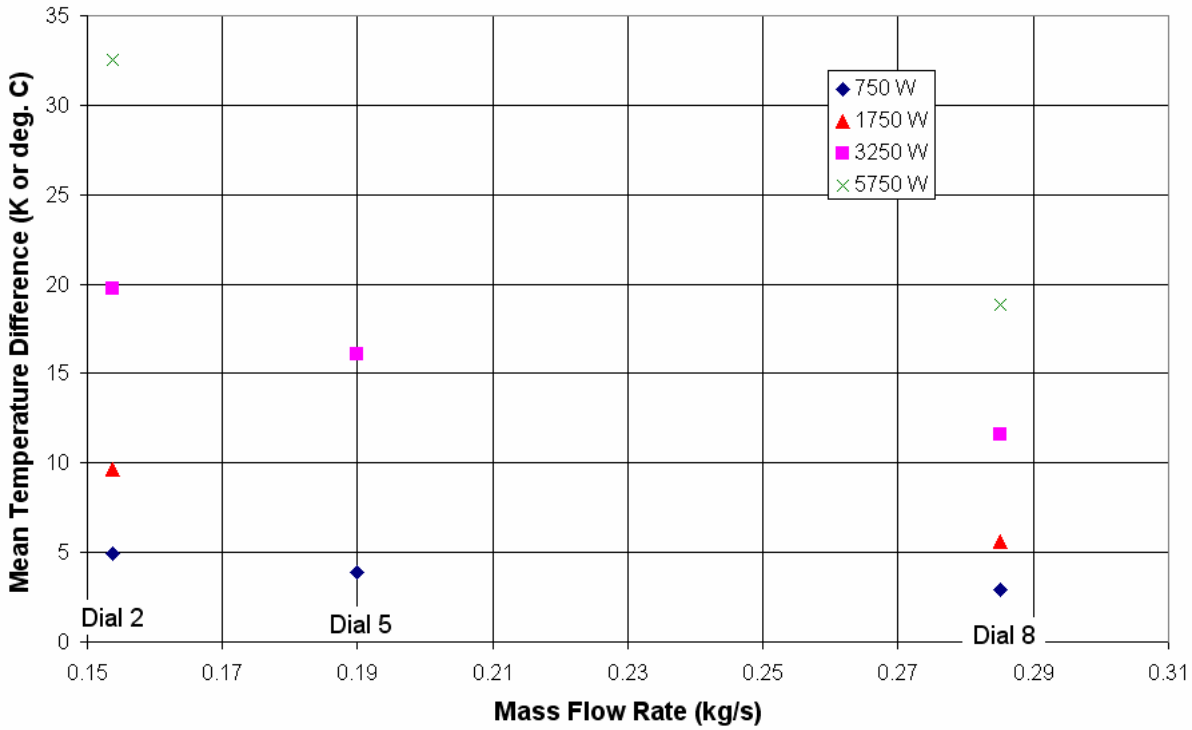

Figure 76: Experimental Mean Temperature Difference vs. Mass Flow Rate

Figure 73 (a) and (b) both make sense qualitatively, as the regions of high temperature are downstream of the heaters that are turned on. Image (d) also makes physical sense, as the temperatures are the highest in the center, and they get lower as the edge is approached radially. Image (c), however, is somewhat surprising. It is interesting that the high temperature region on the right side of the outlet is closer to the upper right corner of the outlet than closer to the middle of the server simulator. One possible explanation for this is that the heat may not be dissipated uniformly by this heater. It might be possible that the amount of heat dissipated increases with increasing height along that heater.

Figure 74 shows that the relationship between the mean temperature difference and the heat load is nearly linear, based on the data taken at dial settings of 2 and 8. Figure 75 confirms the simulation findings that the temperature pattern is not affected by the air flow rate, but the temperature magnitude is. The figure also further demonstrates the repeatability of the temperature measurements. Figure 76 shows the relationship between the mean temperature difference and mass flow rate. Again, the relationship is approximately linear, based on the data taken for heat loads of 750 W and 3250 W.

Comparisons between Simulated and Measured Server Simulator Results

Figure 77 shows the simulated and measured outlet temperature profiles for each of the four heat load combinations (750 W, 1750 W, 3250 W, and 5750 W) at a dial setting of 2. Figure 78 compares the simulated and measured outlet temperature profiles for two different heat load combinations (750 W and 3250 W) at a dial setting of 5. Figure 79 shows the simulated and measured outlet temperature profiles for four different heat load combinations at a dial setting of 8.

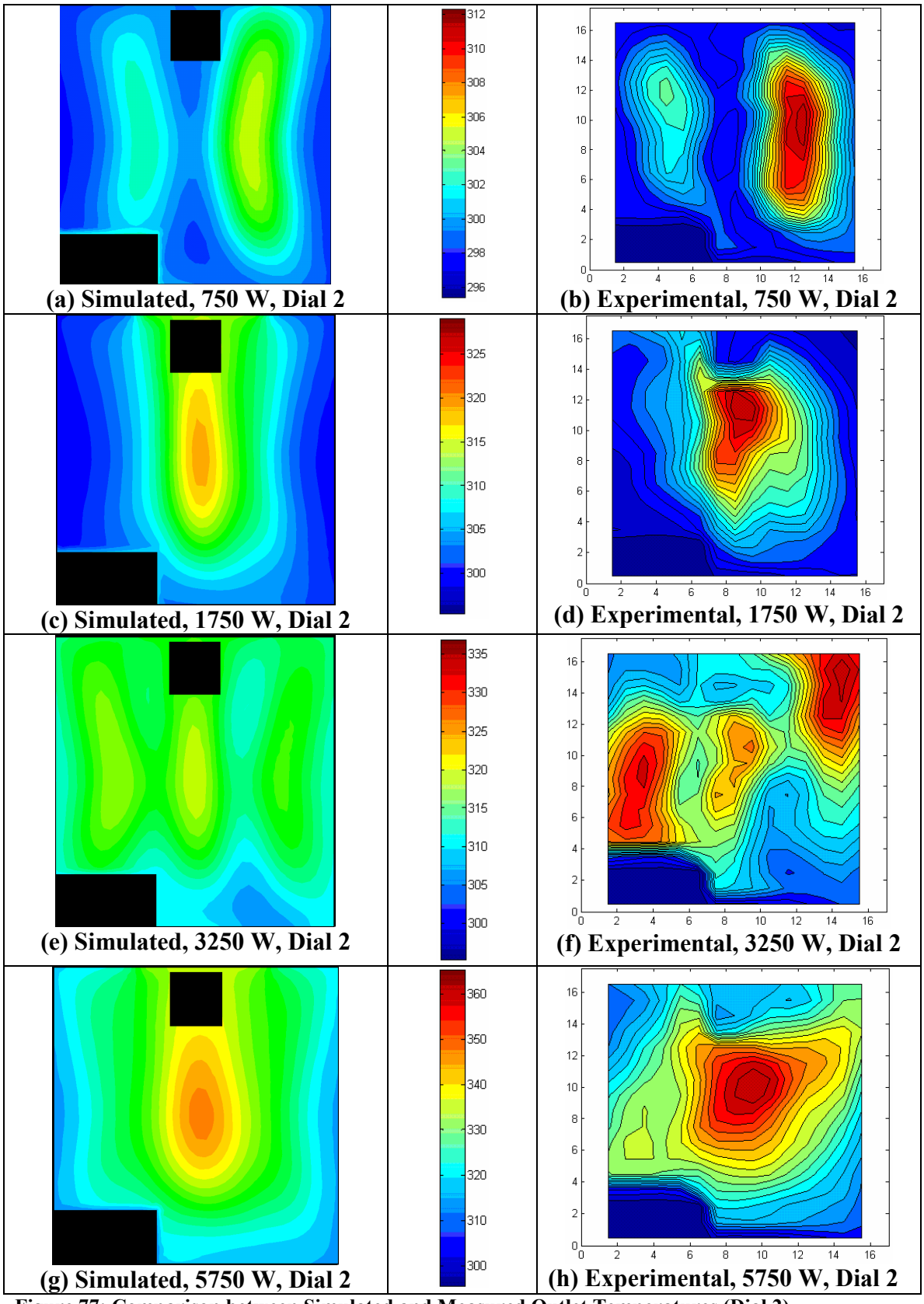

(a) Simulated, 750 W, Dial 2 (b) Experimental, 750 W, Dial 2

(c) Simulated, 1750 W, Dial 2 (d) Experimental, 1750 W, Dial 2

(e) Simulated, 3250 W, Dial 2 (f) Experimental, 3250 W, Dial 2

(g) Simulated, 5750 W, Dial 2 (h) Experimental, 5750 W, Dial 2

Figure 77: Comparison between Simulated and Measured Outlet Temperatures (Dial 2)

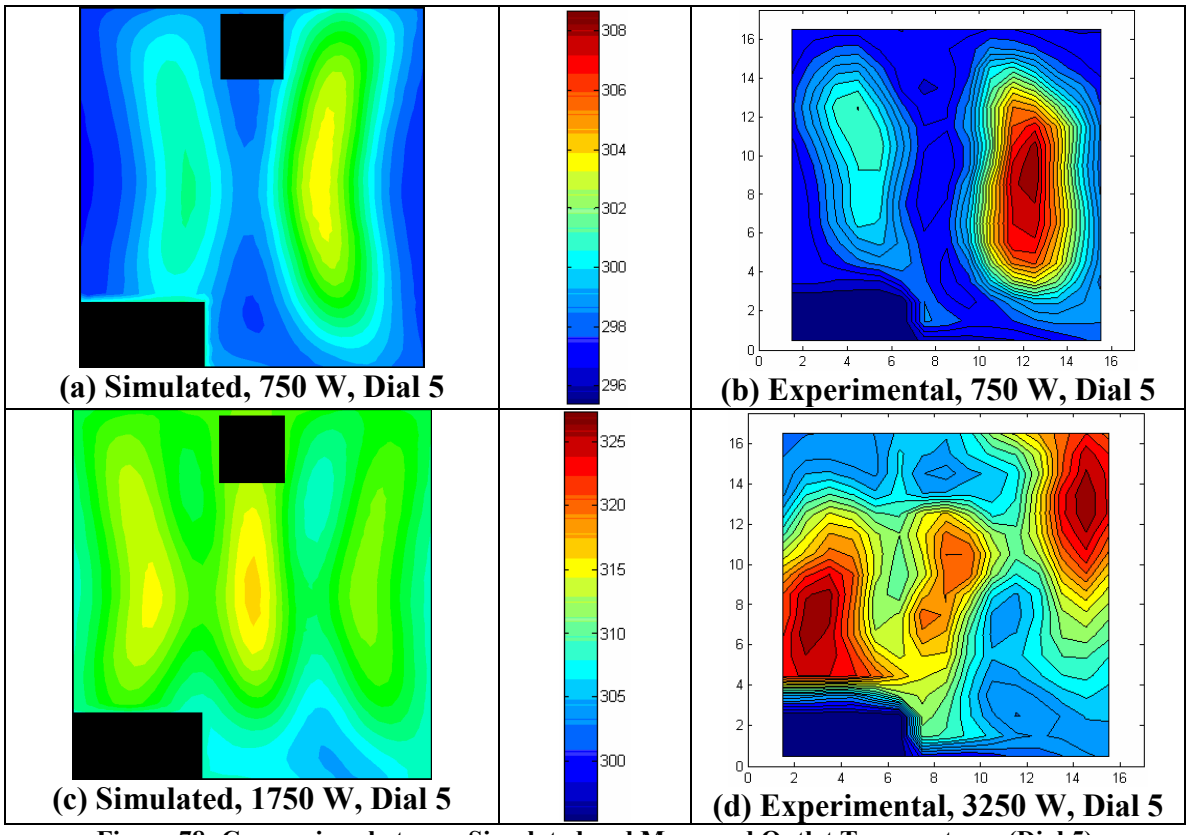

Figure 78: Comparison between Simulated and Measured Outlet Temperatures (Dial 5)

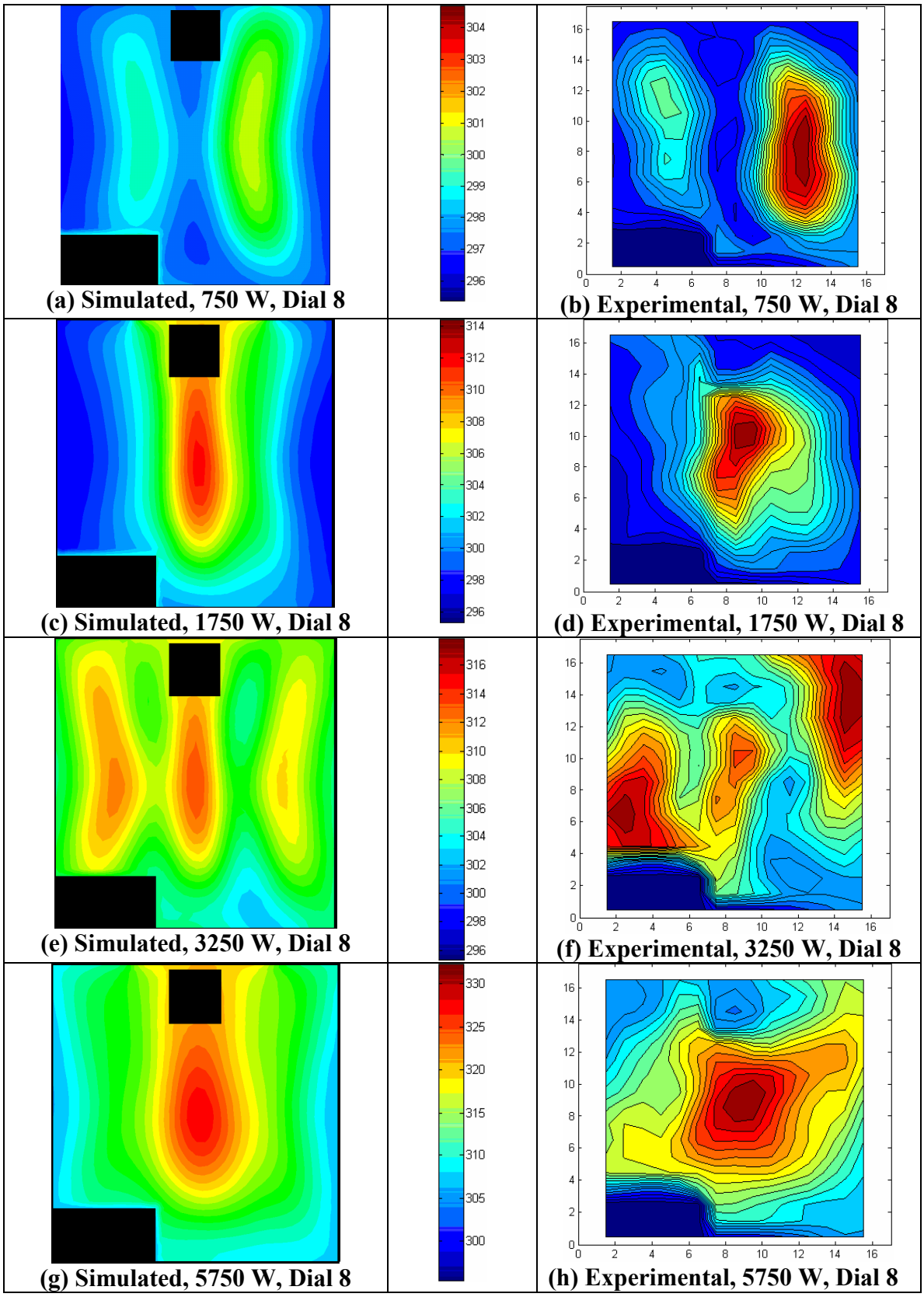

(a) Simulated, 750 W, Dial 8

(b) Experimental, 750 W, Dial 8

(c) Simulated, 1750 W, Dial 8

(d) Experimental, 1750 W, Dial 8

(e) Simulated, 3250 W, Dial 8

(f) Experimental, 3250 W, Dial 8

(g) Simulated, 5750 W, Dial 8

(h) Experimental, 5750 W, Dial 8

Figure 79: Comparison between Simulated and Measured Outlet Temperatures (Dial 8)

In general, the outlet temperature profile patterns are somewhat similar between the simulated and the experimental – especially for the 750 W, 1750 W, and 5750 W cases. The CFD-HT model tends to spread the heat over a larger area than in reality. This could be because the heat is not generated as uniformly as was assumed. Also, the porous media model could have had much to do with the temperature patterns. As previously discussed, it is interesting that the high temperatures for the 3250 W case exist closer to the top of the unit than what is predicted. This could also be due to the non-uniformity of the heat. The other qualitative thing of note is that the maximum temperatures in the simulated 3250-W models exist in the middle, whereas the higher temperatures actually are associated with the heaters on the outside.

A large reason why temperature profiles may not match up exactly is the velocity profile. Figure 80 shows a comparison between the simulated and the measured (using PIV) velocity profiles for three different dial settings (2, 5, and 8). The CFD-HT model predicts that the air flow will be distributed much more uniformly than in the real case. The largest velocity magnitudes in the simulations occur at the four quadrants – each one directly downstream of a fan, whereas the majority of the air is drawn to the center in reality, according to the PIV measurements.

As previously discussed, areas of high air flow rate should have lower temperatures. Therefore, if the air flow rate is actually low toward the outside of the server simulator, then the temperatures on the outside should in turn be higher. The simulations predict high velocities on the outside and low velocities on the inside, which generally results in lower temperatures on the outside and higher temperatures in the middle. In actuality, the opposite is true, as the high velocities on the inside drive the temperatures down near the middle, and low air flow around the edges causes the temperatures there to increase. The reason for the discrepancy between velocity profiles will be discussed later in this chapter.

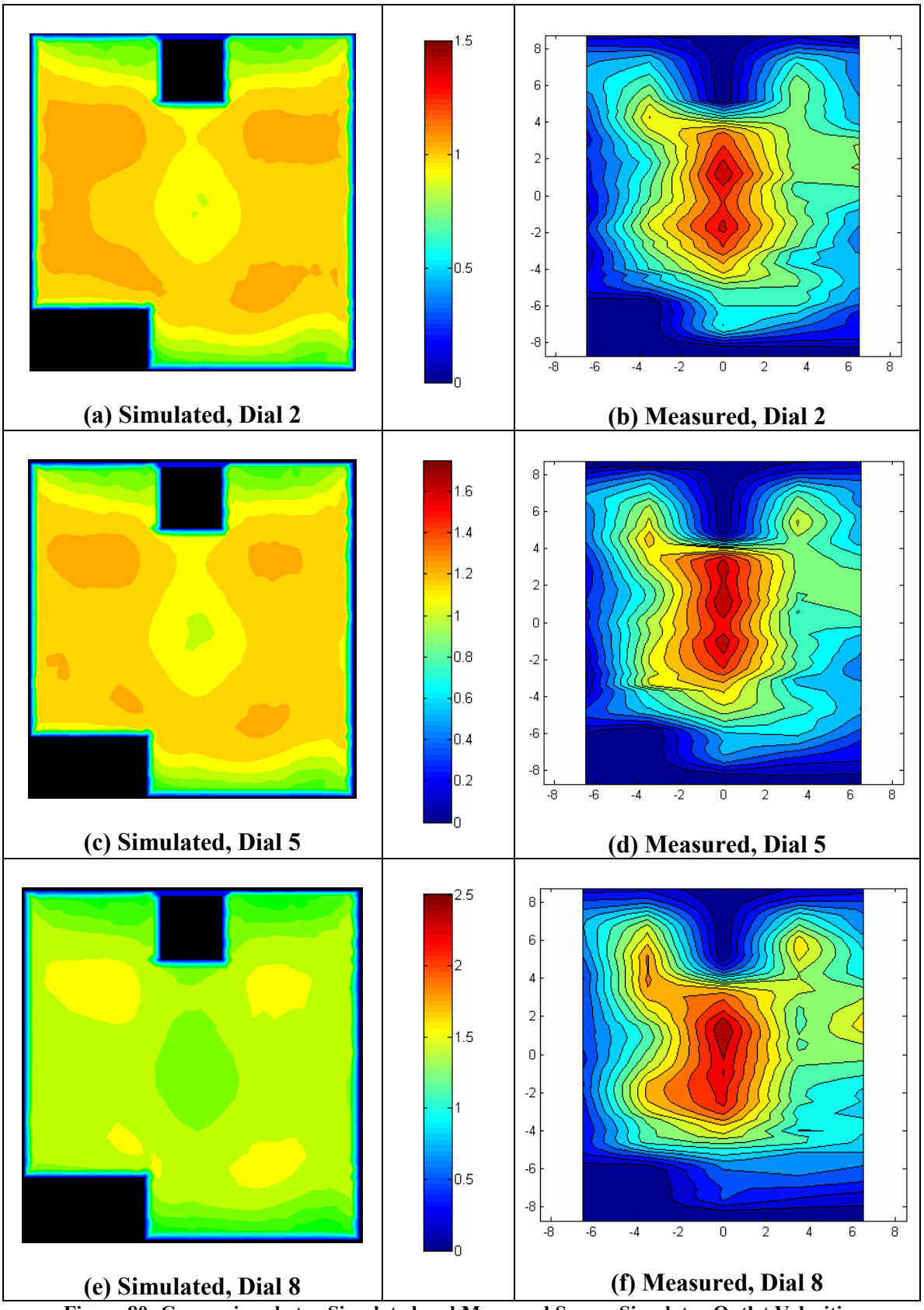

(a) Simulated, Dial 2

(b) Measured, Dial 2

(c) Simulated, Dial 5

(d) Measured, Dial 5

(e) Simulated, Dial 8

(f) Measured, Dial 8

Figure 80: Comparison betw. Simulated and Measured Server Simulator Outlet Velocities

It is important to note that the detailed experimental velocity profiles presented in the contour plots above are the result of only 5 vertical planes of outlet velocity measurements. The interrogation areas basically resulted in 42 data points in the vertical direction, however.

While the measured velocity profiles may not be exact, the location and magnitude of the highest velocity values is accurate. This was verified using a rotational anemometer air velocity meter, which has a digital readout. The anemometer was held at different locations at the outlet of the server simulator to compare the readings to those found using the PIV. It was confirmed that the maximum velocities were indeed located at the center of the outlet. It was also found that for a dial setting of 8, the maximum velocity from the anemometer ranged between 2.3 and 2.5 m/s, whereas the maximum velocity found by PIV was approximately 2.5 m/s. For a dial setting of 5, the maximum velocity was found by the anemometer to be between 1.5 and 1.6 m/s, whereas the velocity from the PIV measurements was found to be approximately 1.65 m/s. Lastly, for a dial setting of 2, the anemometer readings ranged from approximately 1.3-1.4, whereas the value from the PIV was found to be 1.5 m/s. The anemometer uses a set of rotating blades to estimate the air flow rate, and then it integrates over the area of the meter to estimate the velocity. If the velocity decreases from the center of the meter to the edges, then it might slightly under-report the maximum velocities, as was the case.

Table 7 contains a summary of the temperature results. ΔT is defined as the difference between the outlet and the inlet temperature. $\Delta \overline{T}$ is defined as the difference between the area-weighted average outlet temperature and the average inlet temperature. It is important to note that the inlet temperature for the simulations was set as a uniform 22.22^{o}C (72^{o}F or 295.37 K), based on the assumption that the inlet temperature of the actual server simulator was uniform and equal to the set point temperature of the CRAC unit. The server simulator was placed in the room away from areas of varying air flow

rates – near the CRAC unit return. So, for example, a reported $\Delta\overline{T}$ of 3.87 K means that the area-weighted average temperature was 26.09°C (or 299.24 K).

Table 7: Simulated vs. Measured Outlet Temperature Quantitative Results

Dial	Heat (W)	$\Delta\overline{T}$ (K or °C)			ΔT_{max} (K or °C)		
		Sim.	Measured	% Diff.	Sim.	Measured	% Diff.
2	750	3.9	4.9	21.24%	10.5	16.9	37.9%
	1750	9.2	9.7	4.65%	26.9	33.6	19.9%
	3250	16.8	19.8	14.93%	26.0	41.5	37.3%
	5750	29.8	32.5	8.30%	57.5	69.9	17.8%
5	750	3.4	3.9	13.89%	9.2	13.3	30.9%
	3250	14.6	16.1	9.50%	22.7	32.0	29.2%
8	750	2.7	2.9	7.56%	7.5	9.3	19.6%
	1750	6.4	5.6	13.27%	19.0	19.1	0.2%
	3250	11.7	11.6	0.78%	18.5	22.5	18.0%
	5750	18.8	20.7	10.11%	40.2	36.9	9.1%

It is important to point out that there is some uncertainty associated with both the inlet and outlet measured temperature measurements. For example, the inlet temperature for the simulation was chosen as 72°F (22.22°C) based on the CRAC unit set point. It was observed (based on thermocouple measurements) that the temperature at the inlet would vary by as much as 0.7°F (0.39°C) over time. Also, the thermocouples have a possible uncertainty of approximately 0.8°F (0.44°C). Therefore, the measured ΔT's have approximate uncertainties of about 0.83°C associated with them.

In general, however, the temperatures are under-predicted at the lower fan dial settings. As previously discussed, the reason that the CFD-HT model does not accurately predict the maximum outlet temperature is that the velocity profile is predicted to be more uniform than it is in actuality. The CFD-HT model does not predict areas of

extremely low air flow rate, especially those that exist near the edges. This is one possible explanation of why the maximum temperatures for the 750 W and 3250 W cases are generally under-predicted by the model; the maximum temperature should be higher near the edges than represented in the simulations.

The reason that the mean temperatures are different, especially for the lower dial settings, is that the operating points are inaccurate. Figure 81 shows the air flow rate as a function of the dial setting. The nominal air flow rates were provided by the manufacturer, and they are based on the power input (208V, 3PH). The volumetric flow rates were also measured using the FlowHood.

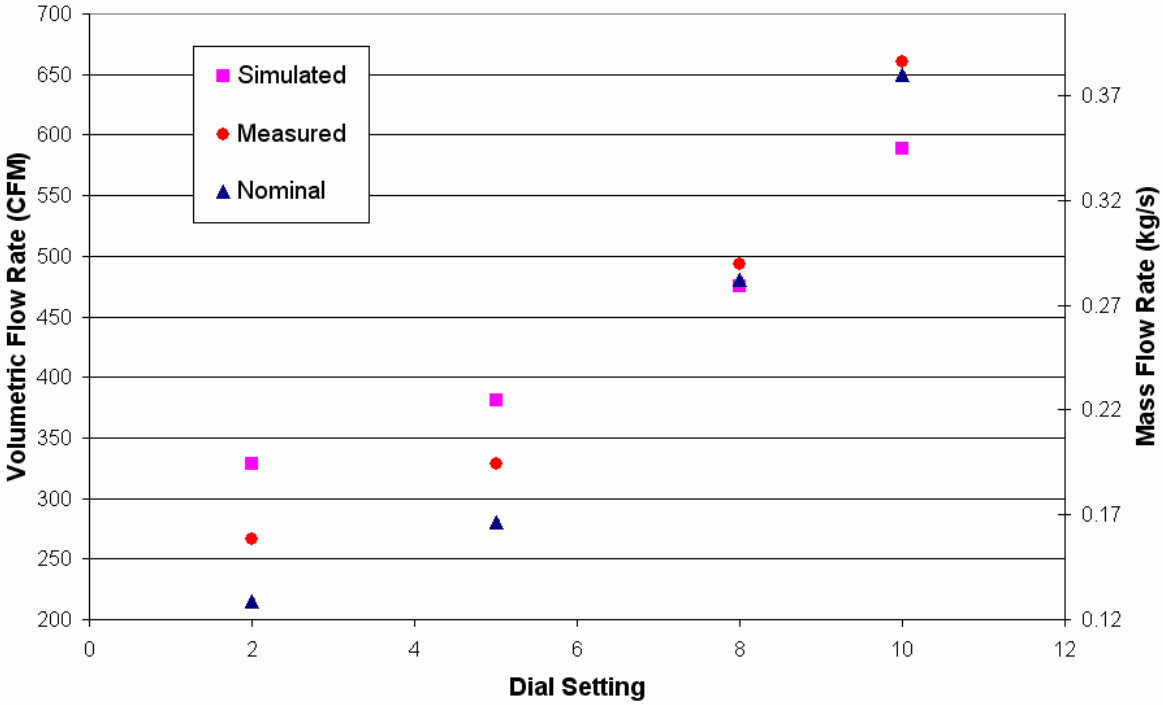

Figure 81: Air Flow Rate vs. Dial Setting

The simulated air flow rates were calculated by Fluent. To find these values, Fluent essentially approximates that the velocity is equal over each face node. The velocity is then multiplied by the area of that node, and those values are summed to find the volumetric flow rate.

The air flow rate is over-predicted by the CFD-HT model for dial settings of 2 and 5. This explains why the mean temperatures are generally under-predicted by the model at these dial settings. The CFD-HT model slightly under-predicts the air flow rate at a dial setting of 8; this results in the mean outlet temperatures being much closer to the measured values. Table 8 summarizes the air flow rate results. Notice that the simulated air flow rate at a dial setting of 2 has the highest disagreement – approximately 24%.

Table 8: Air Flow Rate vs. Dial Setting

Dial	**Nominal**		**Measured**		**Simulated**		
	Q (CFM)	$\dot{m}$ **(kg/s)**	**Q (CFM)**	$\dot{m}$ **(kg/s)**	**Q (CFM)**	$\dot{m}$ **(kg/s)**	**% Diff.**
2	215	0.124	265.9	0.154	329.0	0.190	23.8%
5	280	0.162	328.5	0.190	380.9	0.220	16.0%
8	480	0.278	493.1	0.285	474.8	0.275	3.7%
10	650	0.376	660.4	0.382	588.3	0.340	10.9%

It should be noted, however, that there is some uncertainty in the reported air flow rates. In reality, the air flow rate will change with a change in temperature, or with increasing heat loads. The manufacturer recommends that if air flow rate measurements were taken at higher temperatures, the actual air flow should be calculated as follows:

$$CFM_{actual} = CFM_{measured} * \sqrt{\frac{460 + \overline{T}(^{o}F)}{530}} \tag{4.2}$$

In the previous equation, $\overline{T}(^{o}F)$ is the average air temperature of the air (in ^{o}F) through the Flowhood. At the temperature range for this case, however, the change in density caused by the change in temperature would have a very small effect on the air flow rate measurements. The highest measured average outlet temperature was for a dial setting of 2 and a heat load of 5,750 W – a temperature of 54.7^{o}C, or 130^{o}F. At this temperature, the air flow rate correction factor would be 1.055. So, the most that the air flow rate measurements would be off by is approximately 5.5%.

4.2.2 Rack Sub-System Experimental Results and Comparisons

Because the server simulator contains the most complicated geometrical objects, those units are the major focus of this study. The only difference between the server simulator model and the rack sub-system model is that the rack sub-system model includes two additional plena and both an inlet and outlet vent. If the pressure drop characteristics of the inlet and outlet vent are known, then the creation of the rack sub-system model from the server simulator model is simple. The rack sub-system level model does not significantly alter the velocity patterns, and therefore it does not have a significant effect on the temperature characteristics of the server simulator model.

A model of a portion of the rack was created to represent the second server simulator from the ground and the associate plena in the rack. Figure 82 shows the rack sub-system model.

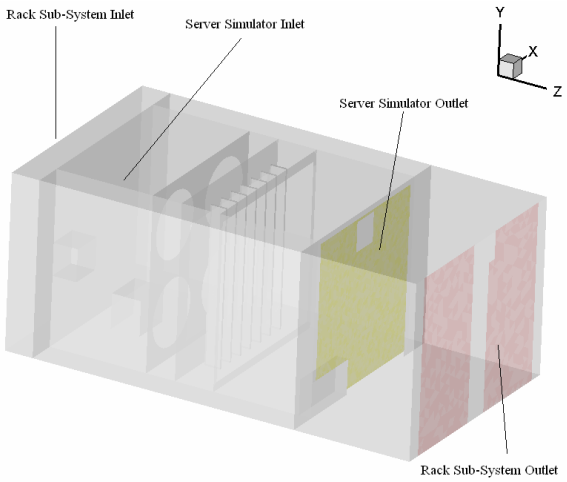

Figure 82: Visual Definition of Outlet Plane for Rack Sub-System Results

The following figures show the simulated and measured temperature profiles at the rack sub-system outlet plane. The rack was located adjacent to a set of porous tiles, and the inlet temperature at the entrance to the modeled portion was approximately constant and uniform (21.11^{o}C or 70^{o}F). Figure 83 shows the rack outlet temperature profiles for varying heat loads at a dial setting of 2. Figure 84 shows the rack outlet temperatures for varying heat loads at a dial setting of 8.

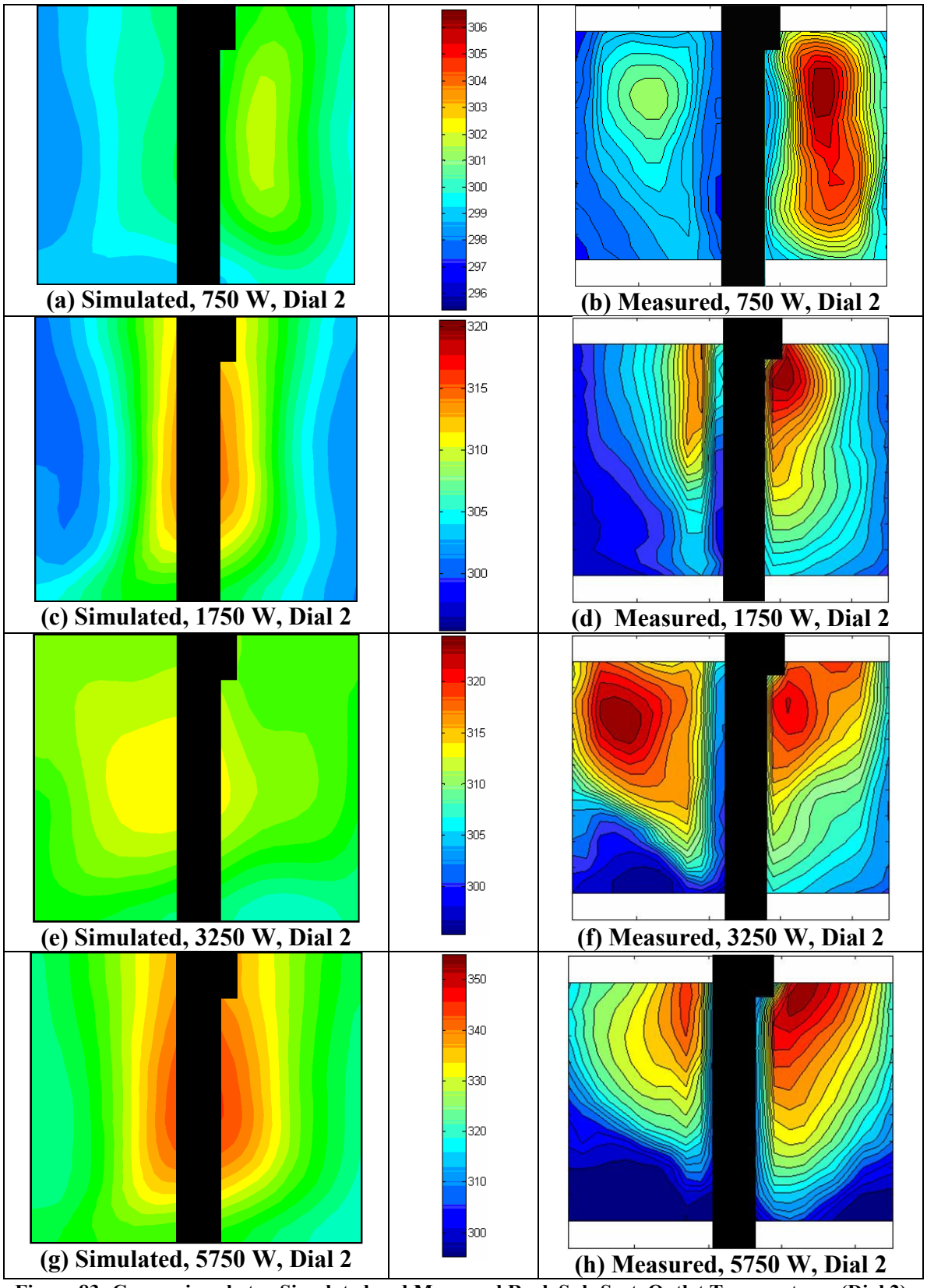

Figure 83: Comparison betw. Simulated and Measured Rack Sub-Syst. Outlet Temperatures (Dial 2)

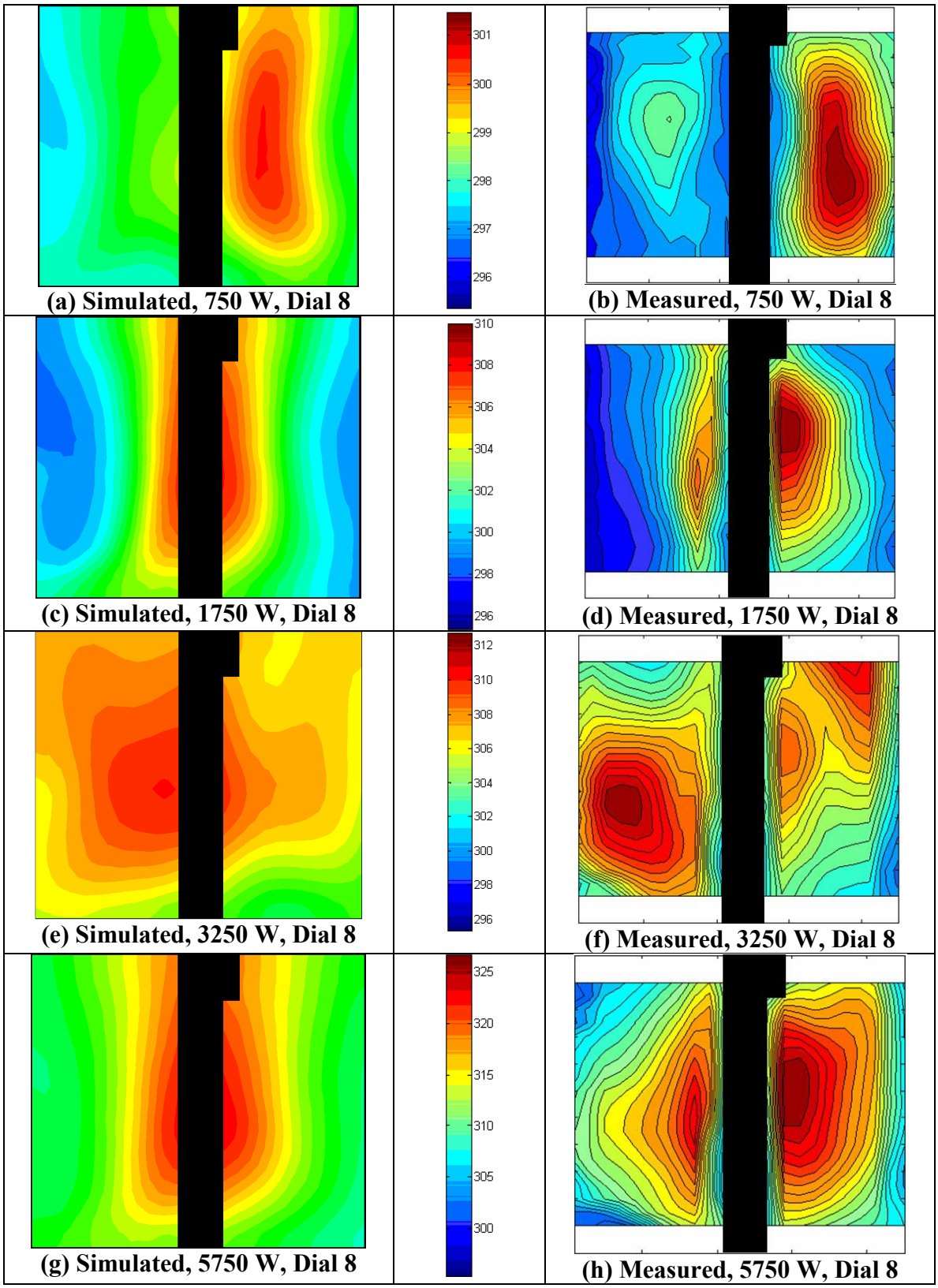

Figure 84: Comparison betw. Simulated and Measured Rack Sub-Syst. Outlet Temperatures (Dial 8)

Just as was the case for the model of the server simulator model, the rack sub-system model under-predicts the outlet temperatures of the rack at a dial setting of 2, but the model is much closer to reality for a dial setting of 8.

4.3 Discussion of the Findings and Conclusions from this Study

A CFD-HT model can provide an engineer with a valuable tool in estimating the velocities and temperatures within electronic enclosures. Such models may potentially provide much more useful information in the design stage than bulk mass and energy balances. Due to the difficulty in multi-scale modeling, it is necessary to develop models at different length levels. For example, a data center CFD-HT model is meant to study the interactions between the CRAC units and the racks in the room than on the chip temperatures. In order to estimate the chip temperatures, on the other hand, a detailed model must be developed at the chip and heat sink level. A model at this level may use estimates of the inlet conditions, rather than relying on what is actually going on at the rack-to-room level. In order to bridge the gap between chip-level and room-level models, more effort must be devoted to creating compact models of the rack. Rather than representing the rack as a cuboid block in a data center environment, it should be represented as an active entity. If a reduced-order model is obtained for each level – chip, rack, and room – then the models can be stitched together to obtain computationally-efficient solutions.

Even at the rack and enclosure level, there must still be some simplifications in order to obtain results in a feasible amount of time. Many detailed components such as vents, heat sinks, and fans must be modeled as simple faces or cuboid volumes with known boundary inputs. Most models of this sort have relied on detailed modeling of each component to create so-called “compact” models of such components. The compact models of the enclosure or rack are then compared to the model that is composed of the most detailed components possible. The problem with this is that there must be a

comparison between the actual physical entities and the detailed or compact CFD-HT models. Experimental data are invaluable in providing a way to evaluate the effectiveness of approximations.

4.3.1 Possible Reasons for Discrepancies

Discrepancies between the Measured and Simulated Mean Outlet Temperatures

The outlet temperature measurements show that the model generally under-predicts both the maximum and the mean temperatures for dial settings of 2 and 5, whereas the mean and maximum outlet temperatures at dial setting 8 are much closer to the actual values. There are two possible reasons for discrepancy between the simulated and the experimental mean temperature values. The uncertainty in the outlet temperature measurements is approximately 0.44^{o}C (0.8^{o}F). Also, there is about a 0.39^{o}C (0.7^{o}F) uncertainty in the room temperature, as the temperature varied from approximately 21.83^{o}C to 22.61^{o}C (71.3^{o}F to 72.7^{o}F). The model assumes a constant and uniform inlet temperature of 72^{o}F (22.22^{o}C). This uncertainty could account for some of the difference at low heat loads or at high air flow rates (such as Dial 8 results) because the temperature difference will be much smaller.

The other reason that the temperatures are generally under-predicted by the CFD-HT model at lower dial settings is that there is much uncertainty in the determination of the operating points. The Dial 2 model over-predicts the air flow rate by approximately 24%, and the Dial 5 model over-predicts the air flow rate by approximately 16%, but the Dial 8 model predicts an air flow rate that is within about 4% of the actual value. It makes sense, then, that the mean temperatures are under-predicted for the lower dial settings and much closer for the dial 8 setting.

The operating point is solved for as the point where the system's fan performance curve meets the system pressure drop curve. For this system, four fans contribute to the

system fan performance curve. There are also a number of sources that contribute to the system pressure drop curve: frictional pressure drops across walls of the simulator, contraction and expansion pressure drops through the simulator, the outlet grille pressure drop, the inlet grille pressure drop, and the pressure drop across the fins. Because the fan performance curves and all of the component pressure drop characteristics depend on empirical data as inputs to the CFD-HT model, the uncertainties in the experimental determination of these characteristics could lead to large discrepancies between the simulated and the experimental results.

All of the fan performance and the component pressure drop characteristics were found using the airflow test chamber. It was noticed in Figure 57 (page 83) that the measurements of the change in pressure as a function of the air flow rate are in fact repeatable. It was found in Figure 54 (page 80), however, that the results may not be accurate. There is some uncertainty (possibly as much as 25%) involved in the conversion of the pressure drop across the nozzle plate to the air flow rate through the airflow test chamber. The relationships for each of the nozzles was provided by the manufacturer, but another method of measuring the air flow rate through the chamber should be used to calibrate these curves.

The largest difference between the measured and simulated flow rates occurs at a dial setting of two – 24% – which is slightly less than the 25% difference of flow rates found using two different nozzles. The three empirical pressure drop relationships combined (inlet grille, outlet grille, and fins) cannot account for 25% system uncertainty even if the uncertainty in each is 25% because they do not account for 100% of the system pressure drop; there is still pressure drop associated with friction, expansion, and contraction that is calculated by the CFD-HT package. However, they may account for some of the discrepancy.

The empirical fan performance curves also contribute significantly to the overall uncertainty. Combined, the four fan performance curves account for 100% of the

system's air flow. Therefore, if everything else in the system correctly predicted the pressure drop as a function of flow rate (which it probably does not), but each of the fans was off by 25%, then the system air flow rate would be off by 25%. The following two figures illustrate this point.

Figure 85 shows the measured fan curve data for dial settings of 2, 8, and 10, along with the curve-fits, and the curve fits if the air flow values were off by 25% from the polynomial curve-fits. Figure 86 shows the system fan performance curves for dial settings of 2, 8, and 10. Since the four identical fans are in parallel, the system fan curve can be estimated by keeping the static pressure constant but summing the corresponding air flow rates from each of the fans. Then, the system air flow value at each corresponding static pressure value would be four times the air flow value for each fan.

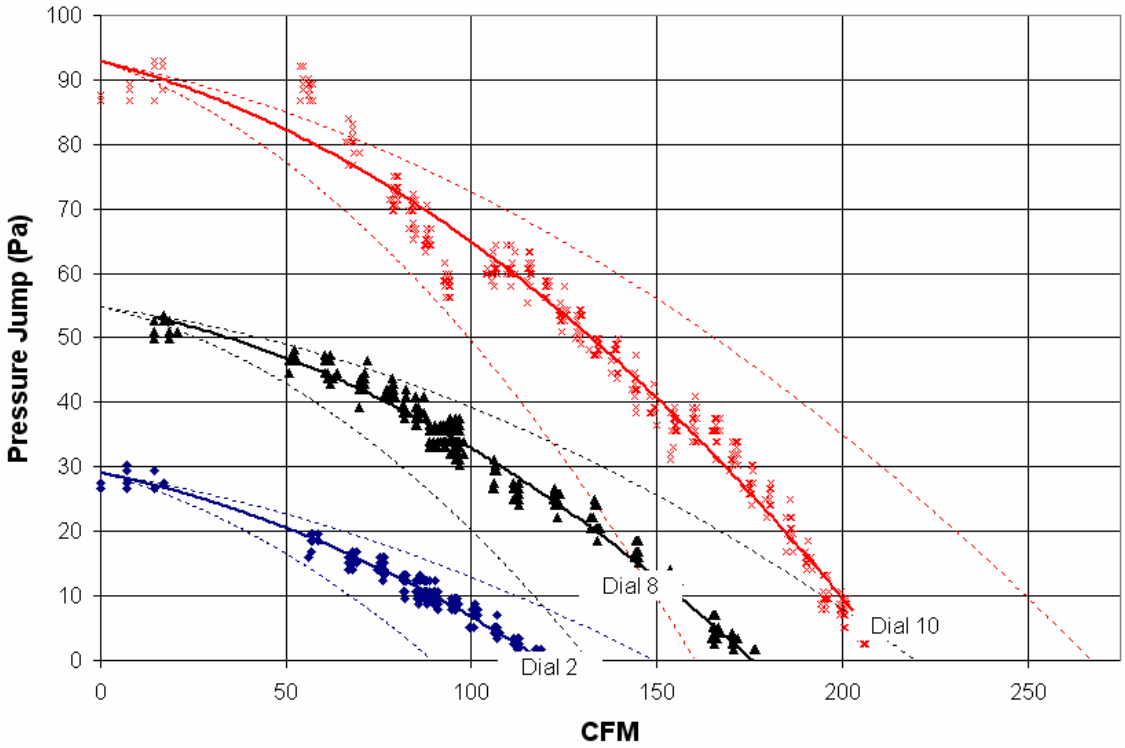

Figure 85: Fan Performance Curves with 25% Air Flow Uncertainty Bars

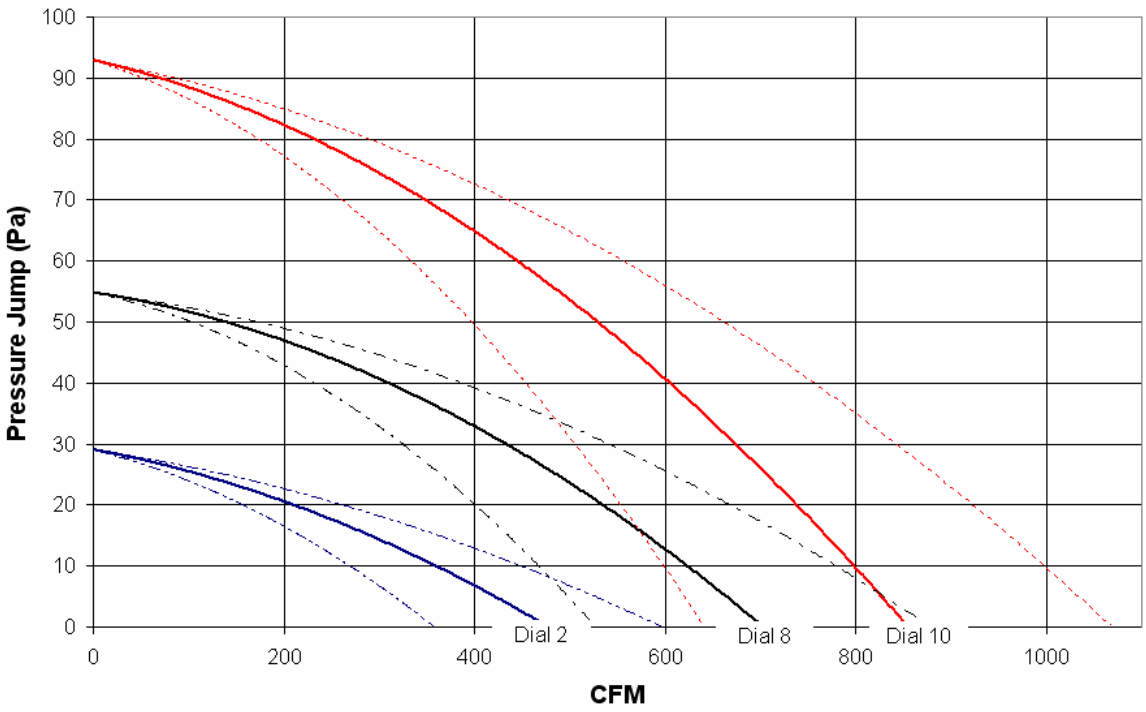

Figure 86: System Fan Performance Curves with 25% Air Flow Uncertainty Bars

Again, if the uncertainty in the fan performance curves accounted for the entire system uncertainty, then the system air flow rate could be off by as much as 25%. For example, if the simulated system air flow rate at a dial setting of 2 is 329 CFM, then it is possible that the actual CFM could be anywhere from 247 to 411 CFM, which is a large range. Add to this the uncertainty in each of the component pressure drop characteristics, and the range would be even higher than 25%. Therefore, since the measured characteristics relied on the manufacturer's relationship between the nozzle pressure drop and the air flow rate, and since it was found that those air flow rates could possibly be off by as much as 25% between nozzle curves at the same air flow rate, then it is certainly plausible that the measurement uncertainty is the largest factor to the discrepancy between the simulated and measured air flow rates; this in turn leads to the discrepancy between the measured and simulated mean outlet temperatures.

Discrepancies between the Measured and Simulated Maximum Temperature Values and Locations

There are four possible reasons for the differences between the server simulator CFD-HT outlet temperatures and the measured values. For dial settings of 2 and 5, the maximum temperatures for all of the heat load combinations are under-predicted. This is because the air flow rate is over-predicted by the CFD-HT model. That is the first source of discrepancy.

The second source of discrepancy between the measured and the simulated maximum outlet temperatures is the modeling of the heater. It was assumed that the heat is dissipated uniformly across the height of the heater that is surrounded by the fins. This results in the heat being removed more uniformly over the heater than in actuality. The experimental results show that the highest outlet temperatures downstream of each of the heaters are more concentrated in the middle than at the top or bottom. Also, the highest outlet temperature downstream of heater 1 occurs near the top of the outlet.

The third reason why the maximum temperature at the outlet may differ from the actual case is the treatment of the fin bank as a porous media. In actuality, the heat removal will be due to conduction from the heater to the fins and convection from the heater and fins to the fluid. The compact model treats the bank of fins as a cuboid block with an equivalent thermal conductivity. This will affect the way that the heat is spread across the fins.

The fourth, and perhaps the most significant reason why the maximum temperatures are in general under-predicted is due to the differences in velocity patterns within the server simulator. The model predicts the largest air flow rates to occur at the four quadrants downstream of the fans, whereas the air flow is actually drawn to the center of the unit. This explains why the maximum temperatures for the 3250 W case are

predicted to exist in the center but they are actually toward the edges where the flow in reality is lower than predicted.

The reason for this large difference is that the fans are modeled as simple faces with empirical pressure drop characteristics. In reality, the fans have curved blades that rotate and propel fluid in a swirling pattern, but this is not represented in the server simulator model; the simplified fan model in the server simulator causes the air to be propelled only in the z-direction, toward the outlet. Consider, on the other hand, if the actual pattern looked like the following Figure 87, which is probably closer to reality.

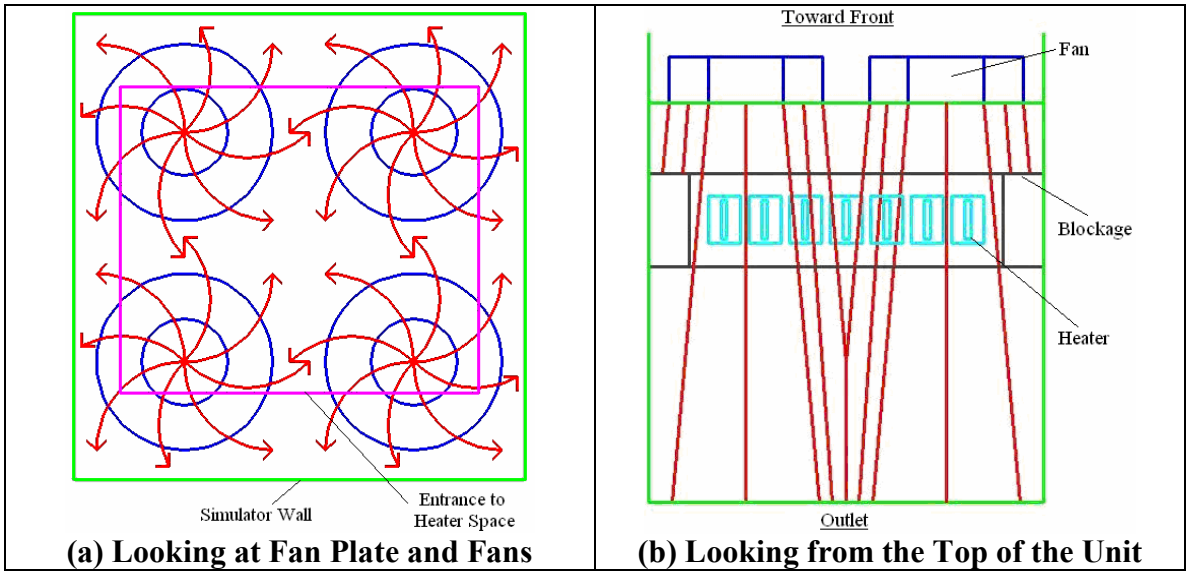

(a) Looking at Fan Plate and Fans **(b) Looking from the Top of the Unit**

Figure 87: Explanation of the Effect of Fan Swirl on Server Simulator Model

Image (a) shows a view as if looking directly at the fan plate and fans. The outer rectangle represents the outer walls of the server simulator, while the inner rectangle shows the opening in the heater space that is 3 in. (7.6 cm) downstream of the fans. The fans all rotate the same way, so the swirl velocity may look something similar to what is represented in this image. There is a high resistance toward the edges of the server simulator, as the air would hit the outer walls of the unit and then hit the blockage around the entrance to the heater space. Therefore, the majority of the radial air flow would be directed toward the center of the server simulator. Since the fans are identical, and they

are placed symmetrically around the center of the unit, air would move to the middle before exiting the unit. Image (b) shows a top view of the schematic of the effect of fan swirl, and particularly the radial velocity.

Fluent offers the ability to model fan swirl, as previously discussed, by allowing one to input the relationship between the radial and tangential velocity components and the distance from the center of the fan. The problem is that one may not determine these components analytically based on the geometry of the fan blades. Also, it has been shown that even detailed models of fan blades do not accurately predict the fan swirl components [17]. The only way to model the fan swirl is to determine the relationships experimentally.

4.3.2 Recommendations for Future Work

The airflow test chamber is a helpful tool in obtaining fan performance curves and component pressure drop characteristics. Unfortunately, the method of calculating the air flow rate relies on a relationship between the pressure drop across a nozzle plate and the air flow rate. This relationship was provided by the manufacturer, and it was determined – based on the fact that there are some discrepancies between data sets for two different nozzles – that these calibration curves may not be reliable. In the future, these curves should be calibrated. The problem, however, is that one must measure the air flow rate and the nozzle pressure drop simultaneously at a number of different flow rates to obtain the relationship between the two values.

To estimate the air flow rate, point-wise velocity measurements must be taken at several locations over the inlet of the airflow test chamber. The velocities should then be integrated over the area. This must be done for each nozzle and for many different values of air flow (obtained by varying the counter blower rotational speed). Although this would be a time-consuming process, it would be the best way to calibrate the nozzle plate curves. One might also use a measurement tool, like a flowhood, that could take an array

of point-wise velocity measurements over the entire area of the inlet at one time. In any case, after the nozzle plate curves were recalibrated, one must do the following: From fan performance curves, grille and fin pressure drop curves, one must convert the air flow rates back to nozzle plate pressure drops using the old calibration curves. For the fans, two 2 in. nozzles were used. For the fins and grilles, the reported curves used the 1.6 in. nozzle. The new calibration curves could then be used to convert the nozzle pressure drops back to air flow rates, and the new fan performance curves and component pressure drop curves could then be reapplied to the CFD-HT model. This process would reduce much of the experimental uncertainty in the empirical boundary conditions, which would in turn likely reduce the discrepancy between the air flow rates found by the simulations and by measurement.

Also, the Flowhood measurements of air flow rates were taken with no heat dissipation, and therefore the air was at room temperature. If the air flow rates had been taken for every dial setting and heat load combination, slightly different values would have been reported due to a decrease in air density with increasing temperature. It was noticed, for example, that a measurement of the air flow at the highest temperature in this case might need to be corrected for changes in density by as much as 5.5%. While this cannot quantify the effect that temperature would have on the actual air flow rate for ranging temperatures in a system, it does illustrate that temperature would have some effect. Therefore, in order to report the most accurate air flow rate values, the air flow measurements should be repeated at every dial setting ***and*** heat load combination. The reported values should then be corrected for density by using the average outlet temperatures measured under the corresponding conditions. It might also be useful to calibrate the Flowhood as well. If one could measure known air flow rates, one could relate the reported values to the actual ones and obtain a relationship between the two.

Temperature measurements were taken by two different methods. In one case, a number of thermocouples were attached to a vertical line and traverse horizontally. Each

of those thermocouples was placed in a thermocouple calibrator to determine the relationship between actual temperature and measured temperature. It was found that the algorithm used by the data acquisition system to relate voltage to temperature was very accurate, as the absolute largest difference between any one measurement and the actual temperature was less than 0.35^{o}C, which is about half of the uncertainty of the temperature measurements. In the other case, a copper wire was grounded, and constantan wires were soldered along the horizontal copper wire. That assembly was then traversed vertically to obtain outlet temperature measurements. The outlet temperature measurements found by this method were then compared to those taken by the other method, but no calibration of this thermocouple "rake" was performed because it would have to have been placed in a large water bath that could be maintained at a constant and uniform temperature. In the future, however, one might attempt to create such a bath in order to obtain a calibration and report more accurate outlet temperature results.

Another future improvement would be to determine the pressure drop characteristics using a wind tunnel. To find component pressure drops, an experimental duct was placed at the inlet of an airflow test chamber. The pressure drop characteristics of the empty duct were subtracted from the pressure drop characteristics of the grille (or fins) mounted in the duct. A relationship between the pressure drop and the average approach velocity to the component was then obtained. If a low-speed wind tunnel could have been used, a uniform approach velocity could have been applied, and more accurate pressure drop relationships could have been obtained. The rectangular test duct might have affected the overall flow pattern, which would have had an effect on the pressure drop characteristics.

Also, the compact model of the fins should be investigated. The porous media model in Fluent does not allow one to change the treatment of the energy equation in the porous medium. It simply calculates an effective isotropic thermal conductivity based on the porosity and the conductivities of each of the materials. In reality, there is more

conduction heat transfer in the lateral direction than in the vertical direction, and there must be a way of representing that more effectively. For example, one might investigate using an effective convection heat transfer coefficient.

Lastly, it is recommended that one take a closer look at the modeling of the fans in the enclosure-level model. Based on the experimental results, it is evident that the fan swirl should be included in this type of model. The problem with doing so is that Fluent only allows one to input the relationship between the fan swirl components and the distance from the center of the fan. In reality, the fan swirl is dependent not only on the radial distance from the center, but on the rotational speed and the operating air flow rate as well. Therefore, to effectively capture the effect of fan swirl in the server simulator, the fan swirl components as a function of radial distance would have to be determined at each dial setting and at varying air flow rates. Therefore, it might be more beneficial to work on obtaining a detailed CFD-HT model of a fan in order to create a compact model of a fan.

A parametric study should also be performed on the turbulence model. The standard k-ε model was used in this study. The inlet turbulence was estimated based on an empirical relationship between the intensity and the estimated Reynolds number. A study on the turbulence characteristics of an inlet vent should be performed. Also, different turbulence models should be applied to determine the sensitivity of the results to the different models.

4.3.3 Conclusions

Creating a model where one has access to the actual physical entity may be viewed as either a blessing or a curse. It is extremely useful in that one may easily obtain many important characteristics that must be used in the thermal CFD-HT models; most notably, fan performance curves and pressure drops characteristics may be obtained and applied to the model, rather than relying on the manufacturer's data, which may or may

not be correct and may not even be available. Experimental testing of components such as heat sinks and grilles is also useful in evaluating the validity of analytical models that are often used to represent the pressure drop characteristics.

If the actual server simulator had not been available, one might have concluded that the compact CFD-HT model correctly predicts the outlet temperatures and velocities. The velocity patterns of the model make physical sense, as the majority of the air flow is concentrated at the four corners of the simulator, which correspond to the locations downstream of the four fans. Given the velocity patterns, the outlet temperature profiles make physical sense as well. For the case with heaters 2 and 6 on (750 W), the areas of high temperature at the outlet are directly downstream of those two heaters. Also, the higher temperatures are spread toward the sides of the unit, which implies that the porous media model is indeed representing the removal of heat through fins somewhat. Similarly, when heaters 2, 4, and 6 are on (1750 W), the outlet temperature is highest at the center (downstream of the 1000 W heater), and it decreases toward the side. When heaters 1, 4, 6, and 7 are on, the areas of high temperature are again downstream of the heaters. The highest temperature corresponds to the area behind the middle heater, which makes sense because the model predicts lower air flow in the center. When all of the heaters are on (5750 W), the highest temperatures exist at the center of the server simulator, behind the three 1000 W heaters.

The experimental data from the server simulator provide invaluable information about the electronics enclosure. Although experimental data could only be taken at the outlet of the server simulator, one may use the results to deduce some of its internal characteristics. The model should be modified according to these deductions, although this is somewhat beyond the scope of this current study, and it is a recommendation for future work. The purpose of this study was to develop a model of an electronics enclosure using the most information possible. Many simplifications had to be made to obtain a

solution, and experiments were then used to determine the validity of the assumptions and the effectiveness of the modeling methods employed.

The experimental data showed that the simulations over-predict the air flow rate at dial settings of 2 and 5. This results in an under-prediction of both the maximum and the mean outlet temperatures. The Dial 8 temperature results are much closer to the measured ones because the air flow rate is very close to the measured. The experimental data also show that the air flow is directed more toward the center of the server simulator than what the model predicts. This results in higher temperatures at the outside of the unit. To resolve these discrepancies, the flow rate measurement method for the airflow test chamber should be calibrated. Also, the fan swirl components need to be determined experimentally to allow the model to more accurately represent the air flow in the simulator.

Once the discrepancies between the measured and simulated outlet temperature and velocity profiles are resolved, it will be simple to create an entire rack-level model. One need only use the server simulator and rack sub-system model to obtain a number of different observations using CFD-HT simulations. Based on these observations, a method such as proper orthogonal decomposition could be used to obtain a reduced-order model of a rack sub-system model. The sub-system models could then be combined to form an entire rack, which could be placed in a room-level CFD-HT model.

The server simulator is invaluable in that it contains many of the same types of geometries that would exist in an actual rack. Since all servers typically contain grilles, fans, and heat sinks, which are attached to the chips or other heat-dissipating components, the methods described in this thesis can be applied to any such model at the rack level. This will hopefully bridge the gap between room-level and chip-level CFD-HT models, which will provide an invaluable tool in the protection of mission-critical electronic equipment.

APPENDIX A

IMPORTANT PRINCIPLES

A.1 A Brief Description of Computational Fluid Dynamics [30, 32]

The only way to determine the temperature and velocity fields at *every* point in a fluid region, one must be able to solve the governing equations at every single infinitesimal point in space. Of course, this can only be done if the solution can be obtained analytically. Unfortunately, in most cases either the geometry or the fluid characteristics (such as turbulence) are much too complex to solve the equations by hand. Therefore, it is necessary to employ CFD-HT.

Computational Fluid Dynamics (CFD-HT) is basically a method by which numerical techniques and algorithms are used to solve the Navier-Stokes equations (described in the next section) in a region that contains a moving fluid. Essentially, a computer is used to apply what is known as the finite element method – which is basically a procedure for solving simplified versions of these equations to iteratively obtain a solution of the Navier-Stokes differential equations.

An important requirement of this method (or any such numerical method for that matter) is that the domain be discretized. In other words, the domain must be split into a collection of smaller volumes. This is known as "meshing." Each volume in a mesh is assumed spatially uniform, and the equations are solved at the intersections of each of these volumes, which are known as "nodes." In the finite element method, each volume in the region is given an initial temperature and velocity, and CFD-HT software changes those values at every volume until the conservation of mass, momentum, and energy are all satisfied for every discrete volume. When the equations are satisfied, a "converged" solution has been reached.

Of course, such iterative processes can often be computationally expensive. Ideally, the domain could be split into an infinite number of volumes, such that the solution could be found over a continuous fluid region. If the domain is split into a large number of volumes, it can more accurately represent the continuous region. So in general, the smaller the volumes in a domain (or the larger the mesh in other words), the more accurate the velocity and temperature field solutions will be. A mesh with an insufficient number of volumes may not even reach a converged solution. This is the fundamental struggle with the use of computers to solve equations iteratively. Obviously, a more refined mesh requires more storage space, and it therefore requires more time to converge. Also, it is not uncommon to run into a situation where the computer used for simulations does not have the resources (particularly the available memory) to run simulations of this sort. Therefore, the trick to CFD-HT is finding the balance between an extremely detailed and accurate solution and one that may be obtained in a feasible amount of time.

A.2 Governing Equations of Fluid Flow and Heat Transfer [32]

All fluid flows can be characterized by a few basic equations. The **conservation of mass** equation basically states that the time rate of change of the mass in a region must be zero. In other words, the mass entering a region must equal the mass leaving a region plus any mass that is stored in the region. The conservation of mass equation may be represented in the following form:

$$\frac{\partial \rho}{\partial t} + \nabla \bullet (\rho \upsilon) = S_m \tag{A.1}$$

In the previous equation, ρ is the density (or mass per unit volume), υ is the velocity, and S_m is the mass source term (This last term is generally zero unless one is dealing with a two-phase fluid).

The **conservation of momentum** principle states that the time rate of change of the linear momentum of a region is equal to the sum of the forces on that region. There may be two types of sources acting on that region: body forces (like gravity) that act on the entire bulk of fluid in the region and also surface forces, which act at the boundaries. The conservation of momentum equation is the following:

$$\frac{\partial}{\partial t}(\rho\vec{\upsilon}) + \nabla \bullet (\rho\vec{\upsilon}\vec{\upsilon}) = -\nabla p + \nabla \bullet (\bar{\tau}) + \rho\vec{g} + \vec{F} \tag{A.2}$$

In this equation, p represents the static pressure and g is the acceleration due to gravity. F is a term that includes any other model-dependent body forces. One such example of a user-defined force is one that is due to pressure drops involved in a porous media model (This will be discussed in more detail later). Lastly, τ is defined as the stress tensor. It may be found from the following:

$$\bar{\tau} = \mu\left[\left(\nabla\vec{\upsilon} + \nabla\vec{\upsilon}^{T}\right) - \frac{2}{3}\nabla \bullet \vec{\upsilon} I\right] \tag{A.3}$$

In Equation 3, μ is the molecular viscosity, and I is the unit tensor.

The **energy equation** states that any increase in the energy of a region is the result of work done to or by the region and also the heat transfer to or from that region. Mathematically, the energy equation may be written as follows:

$$\frac{\partial}{\partial t}(\rho E) + \nabla \bullet (\vec{\upsilon}(\rho E + p)) = \nabla \bullet \left(k_{eff}\nabla T - \sum_{j} h_j \vec{J}_j + (\bar{\tau}_{eff} \bullet \vec{\upsilon})\right) + S_h \tag{A.4}$$

k_{eff} is defined as the effective thermal conductivity of the region, and it is found by summing the thermal conductivity of the fluid in the region (k) and the turbulent thermal conductivity (k_t), which may be estimated by different turbulent models. In Equation A.4,

$$E = h - \frac{p}{\rho} + \frac{\upsilon^2}{2} \tag{A.5}$$

h is the sensible enthalpy, and J is defined as the diffusion flux of the species j. Lastly, S_h includes any kind of volumetric heat generation, such as that caused by an electrical current passing through the volume or a chemical reaction.

Combined, the continuity, momentum, and energy equations are often referred to as the **Navier-Stokes equations**. Together, they prove to be extremely useful in determining the velocity and temperature fields in a material region. For simple cases, it is possible to solve these equations analytically, but often one must use some numerical technique in order to obtain a solution for a more complex problem. This is where a Computational Fluid Dynamics software package becomes of particular use.

APPENDIX B

SAMPLE CALCULATIONS

B.1 Estimation of the Pressure Drop across the Fins Alone

To experimentally determine the fin pressure drop curves, data were first taken with a duct and a heater. Then, data were taken with the duct, heater, and fins. The two sets were then fit to second-order polynomials, and the coefficients were subtracted to find the relationship between the mean approach velocity and the pressure drop across the fins alone.

For example, the curve-fit of the duct and heater for one of the runs was

$$\Delta p = 9.049\upsilon + 0.2423\upsilon^2$$

The curve-fit of the duct, heater, and fins was then

$$\Delta p = 10.921\upsilon + 0.6494\upsilon^2$$

Therefore, the pressure drop across the fins alone was estimated as

$$\Delta p = (10.921 - 9.049)\upsilon + (0.6494 - 0.2423)\upsilon^2 = 1.872\upsilon + 0.4071\upsilon^2$$

B.2 Porous Media Coefficients

The general equation is the following:

$$S_i = -\left(\frac{\mu}{\alpha}\upsilon_i + C_2\frac{1}{2}\rho\upsilon_{mag}\upsilon_i\right) \tag{3.10}$$

In other words, $\Delta p / L = \frac{\mu}{\alpha}\upsilon + \frac{1}{2}C_2\rho\upsilon^2$

Δp is the pressure drop, L is the length, μ is the viscosity, α is the permeability, υ is the velocity in the direction of the flow, C_2 is the inertial loss coefficient, and ρ is the density. To determine these coefficients, the pressure drop vs. velocity data were fit to a second-order polynomial to get $\Delta p = A\upsilon + B\upsilon^2$, where A and B are the coefficients of the curve fit. Therefore, the viscous resistance coefficient is the following:

$$\frac{1}{\alpha} = \frac{A}{\mu L}$$

and the inertial loss coefficient is

$$C_2 = \frac{2B}{\rho L}$$

So, for example, a curve fit of one experimental run of the fins was

$$\Delta p = 1.872\upsilon + 0.4071\upsilon^2$$

Therefore,

A = 1.872, B = 0.4071 and $\mu = 1.789 \times 10^{-5}$ kg/ms, $\rho = 1.225$ kg/m^3, L = 0.0508 m (2 in.)

$$\frac{1}{\alpha} = \frac{1.872}{(1.789 \times 10^{-5})(0.0508)} = 2.059 \times 10^6$$

$$C_2 = \frac{2(0.4071)}{(1.225)(0.0508)} = 13.08$$

APPENDIX C

MESHING STUDY

The smallest length scales in the CFD-HT model exist in the space that contains the heaters. Most notably, the heater itself is 0.25 inches thick, there is only 0.1875 inches between the front of a fin and the front of the heater, and there is 0.375 inches between heater fin banks. Therefore, the majority of the meshing study was performed for the space that contained the heaters alone. The heater space inlet was given a constant and uniform velocity, and the effect of the number of mesh volumes on the mean outlet (of the heater space) velocity and temperature, on the mid-plane temperature and velocities, and on the heater temperatures was studied to determine what mesh size is required. The baseline case was a hex mesh (simple cuboid volumes) containing approximately 1.8 million volumes, which was the largest number possible.The server simulator model was built of a tgrid mesh, which is essentially composed of unstructured tetrahedral elements. The advantage of using a tgrid mesh is that it allows much more freedom. For example, intricately-shaped geometries such as circular fans cannot be modeled using a hex mesh. Also, a tgrid mesh allows one to have very fine mesh areas in one region and then a transition to a coarser mesh in regions of larger lengthscales.

Figure A 1 shows a comparison between the outlet temperatures of the heater space for different meshes. Image (a) results from the baseline hex mesh, and it is the source of comparison. From the figure, one may notice that there is not much difference between the outlet temperature patterns for the different meshes. Similarly, Figure A 2 shows a comparison between the outlet velocities from the hex mesh with 1.8 million elements and a tgrid mesh with roughly 0.86 million elements. This tgrid mesh predicts an average mid-plane velocity that is within 2.8% and an outlet velocity that is within 2.5% of the largest hex mesh. Also, it predicts all of the mean temperatures within 0.35%. Therefore, this mesh size was chosen for the server simulator model.

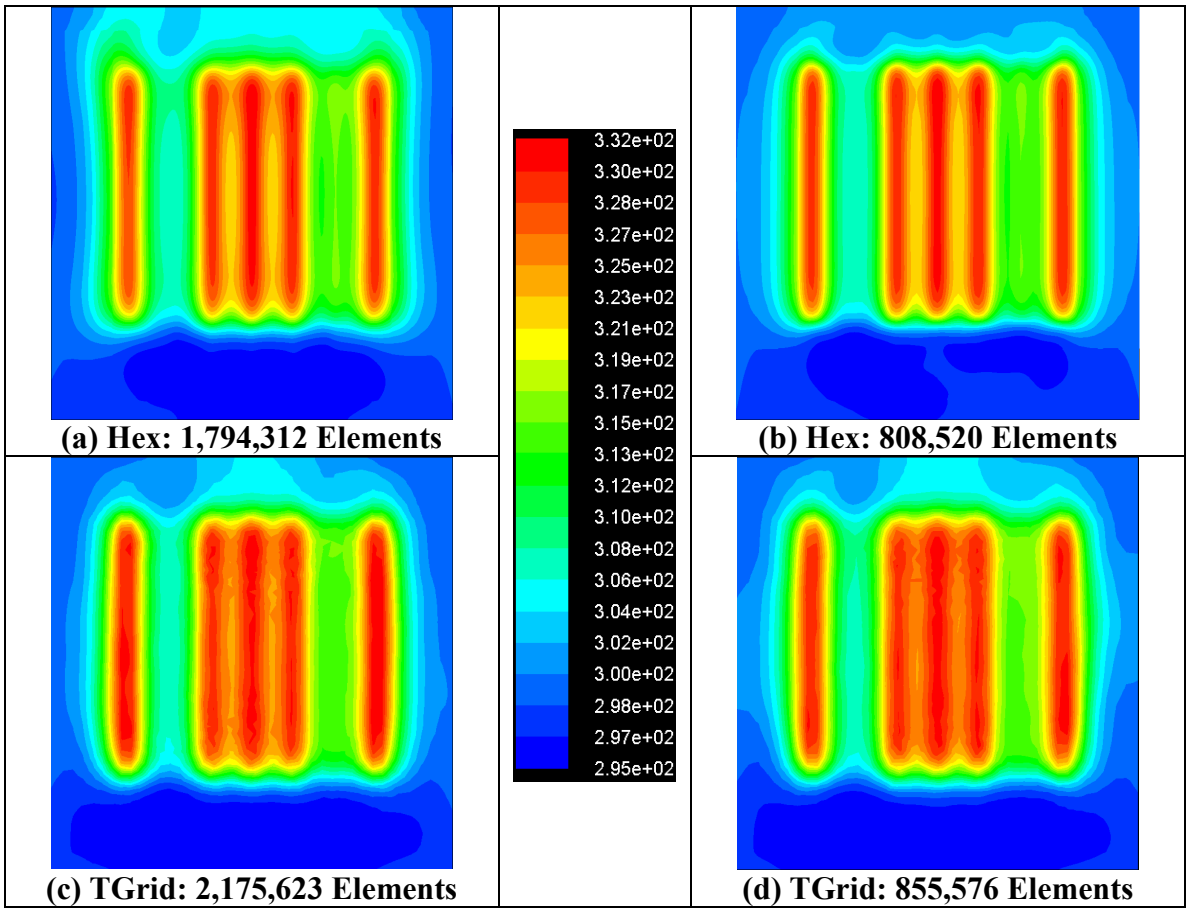

Figure A 1: Comparison between Heater Space Outlet Temperatures for Different Meshes

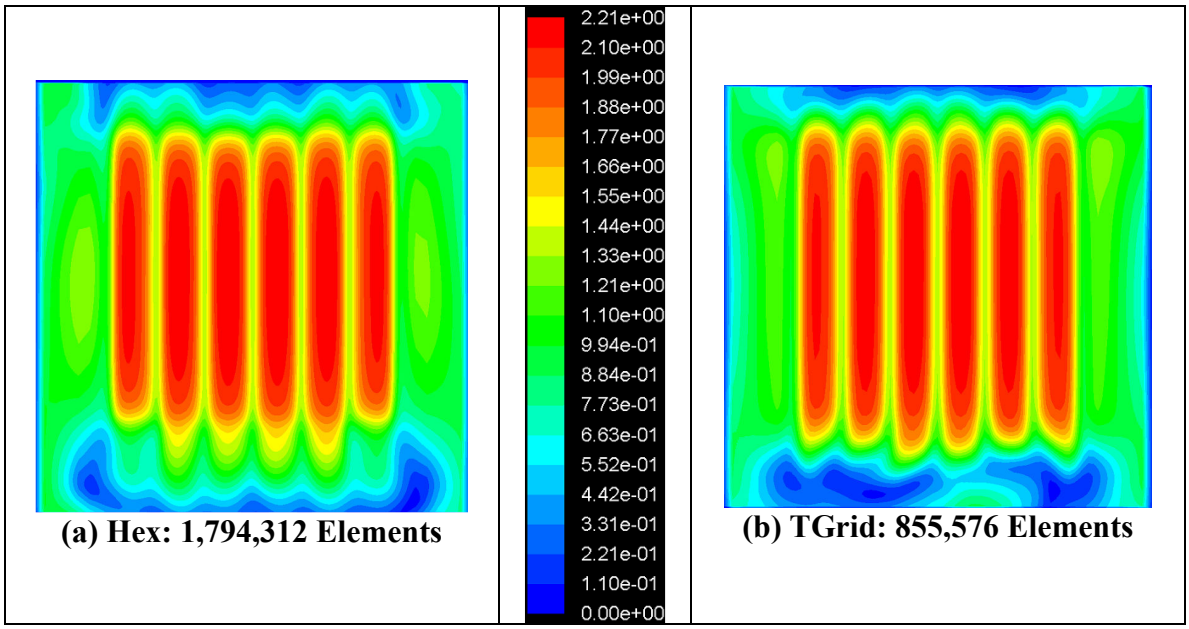

Figure A 2: Comparison between Heater Space Outlet Velocities for Different Meshes

APPENDIX D

CALIBRATION CURVES

D.1 Airflow Test Chamber Curves

In order to convert from the pressure drop across the nozzle plate in the airflow test chamber, the manufacturer provides curves. In order to quickly relate the pressure drop with the air flow rate, several data points were manually extracted for the case with a 1 in. nozzle, then a 1.6 in. nozzle, a 2 in. nozzle, and finally two 2 in. nozzles. The data were then fit to curves. The following Figure A 3 shows the data points extracted from the manufacturer's curves along with the resulting curve fits used for all air flow rate calculations.

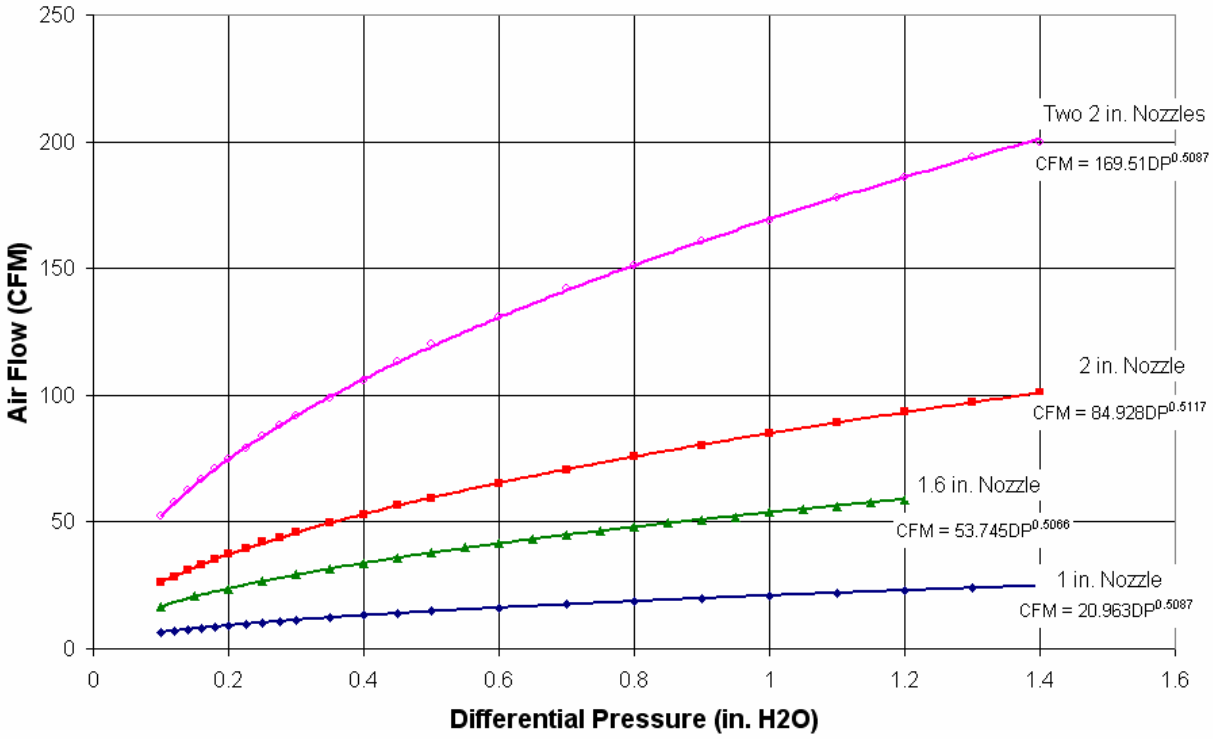

Figure A 3: Airflow Test Chamber Nozzle CFM vs. Differential Pressure Curves

D.2 Pressure Transducer Calibration

The pressure transducers were calibrated before each set of measurements was taken of the airflow test chamber. To calibrate them, an inclined manometer was used to measure the pressure drop across the nozzle plate for varying counter blower frequencies. The pressure transducer was then used to measure the voltage imposed by the pressure drop across the same nozzle plate at the same counter blower frequencies. The pressure drop of the manometer was then plotted as a function of the voltage output of the transducer. The following figure shows some representative results from the pressure transducer calibration. The figure demonstrates the repeatability of the calibration method.

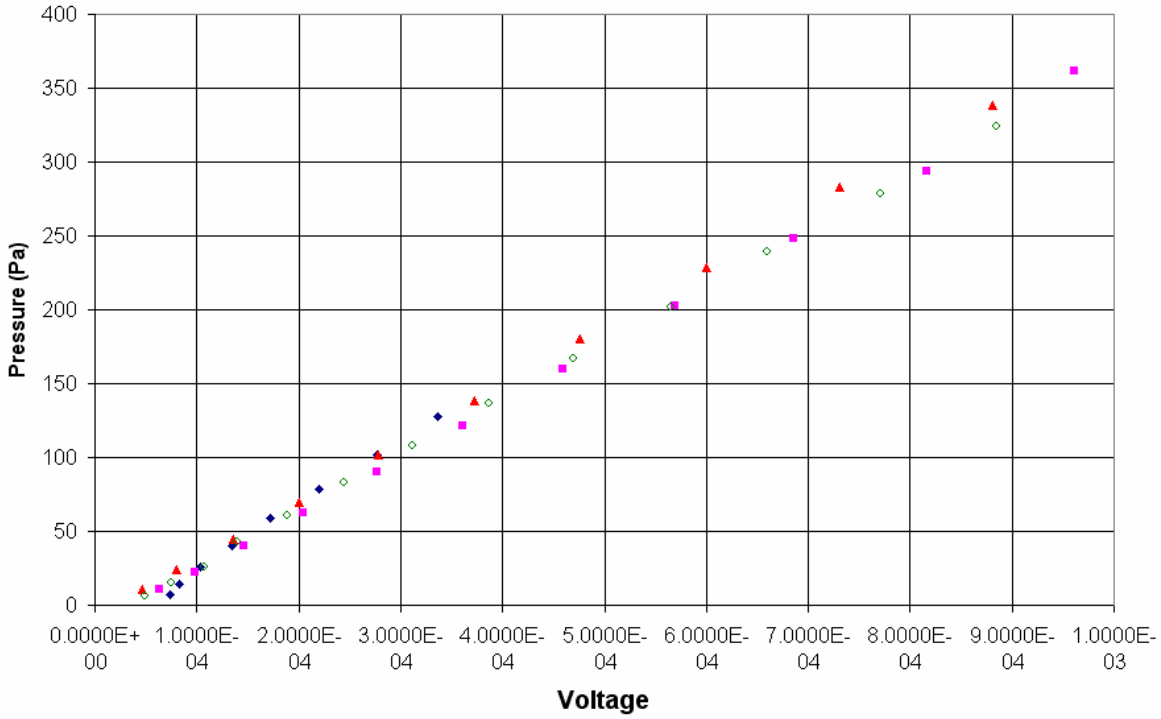

Figure A 4: Representative Pressure Transducer Calibration Data

D.3 Thermocouple and Temperature Data Acquisition System Calibration

The data acquisition system uses a simulated cold-junction temperature along with an algorithm that relates the voltage measured by the thermocouple wire and the temperature. In order to ensure the accuracy of this temperature-measurement method, an individual calibration was performed on each of the thermocouples mounted to the vertical row. Thermocouples that were connected to multiple channels were separately placed in a small tube of water within a thermocouple calibrator. For each of the thermocouples, the temperature of the water bath was set at 20°C, 30°C, 45°C, 60°C, 75°C, and 90°C. A Resistance Temperature Detector (RTD) located internally within the thermocouple calibrator, gave indication of the actual temperature of the water bath. At each of the six water bath temperatures (and for each thermocouple), a set of temperature measurements was taken over a two minute interval. The time-averaged temperature found by each of the thermocouples was then compared to the RTD reading on the calibrator. The following figure contains a representative result of calibration.

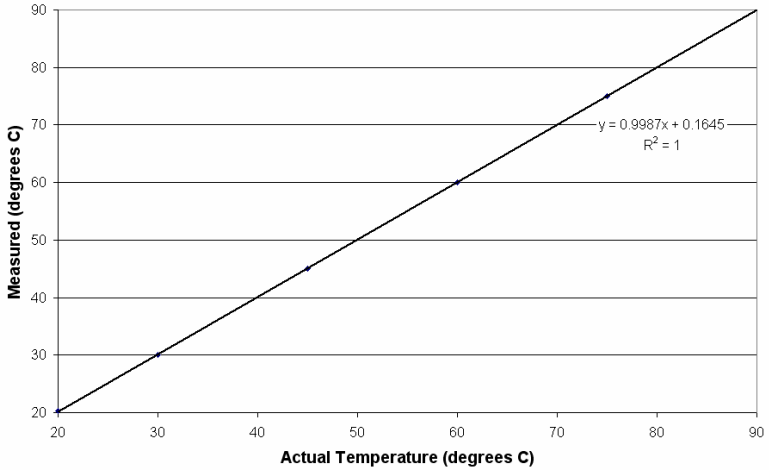

Figure A 5: Representative Thermocouple Calibration Curve

It was found that none of the thermocouples were systematically under or over-predicting the temperatures, and the maximum difference between any measured temperature and the one reported by the calibrator was approximately 0.35°C, which is within the uncertainty of measurements.

APPENDIX E

EXPLANATION OF PIV OUTLET VELOCITY PROFILES

To estimate the outlet velocity profiles of the server simulator, PIV measurements were taken at 5 different vertical planes, as described in Chapter 2. The vertical planes were split into three overlapping sub-planes: one in the middle of the outlet, one near the top, and one near the bottom. Forty pairs of images were taken (from each camera) at each sub-plane. After applying an adaptive correlation to all of the images to determine the velocity vector map, a moving-average filter was applied. This deleted all of the noise vectors. Lastly, a 3D calibration was performed to stitch the results of the two cameras together to form the actual velocity map with accurate values.

Figure A 6 shows some representative results – a raw PIV velocity vector map behind the middle of the server simulator outlet. The orientation is somewhat confusing because of the way the cameras are rotated, but the top of the figure actually runs vertically along the outlet of the server simulator (Refer back to Figure 37 on page 55 for a visualization of the planes). The right side of the image runs parallel to the floor, and the left side runs parallel to the ceiling. So essentially, the air is flowing straight out from the server simulator outlet. Figure A 7 shows the same image after a moving-average filter is applied. Notice that the random large vectors from the raw map are eliminated. Figure A 8 shows the result of the 3D calibration of this image, paired with the same plane taken with the other camera at the same time.

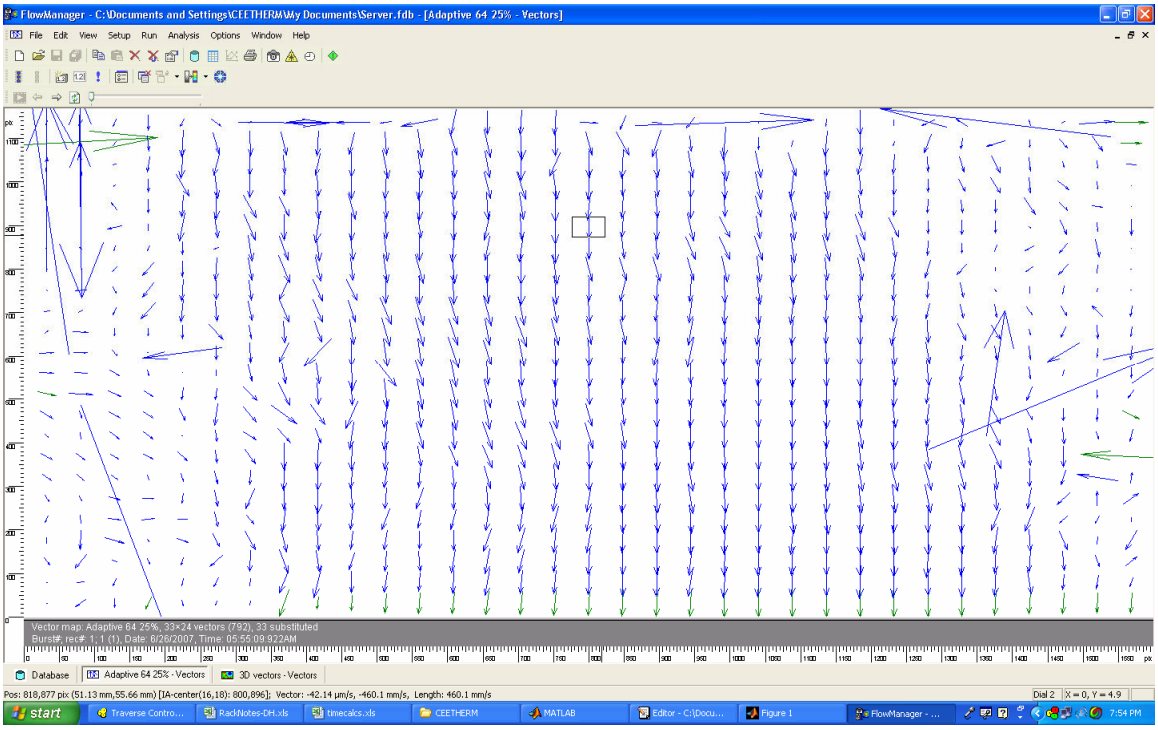

Figure A 6: Raw PIV Vector Map Image of Server Simulator Outlet

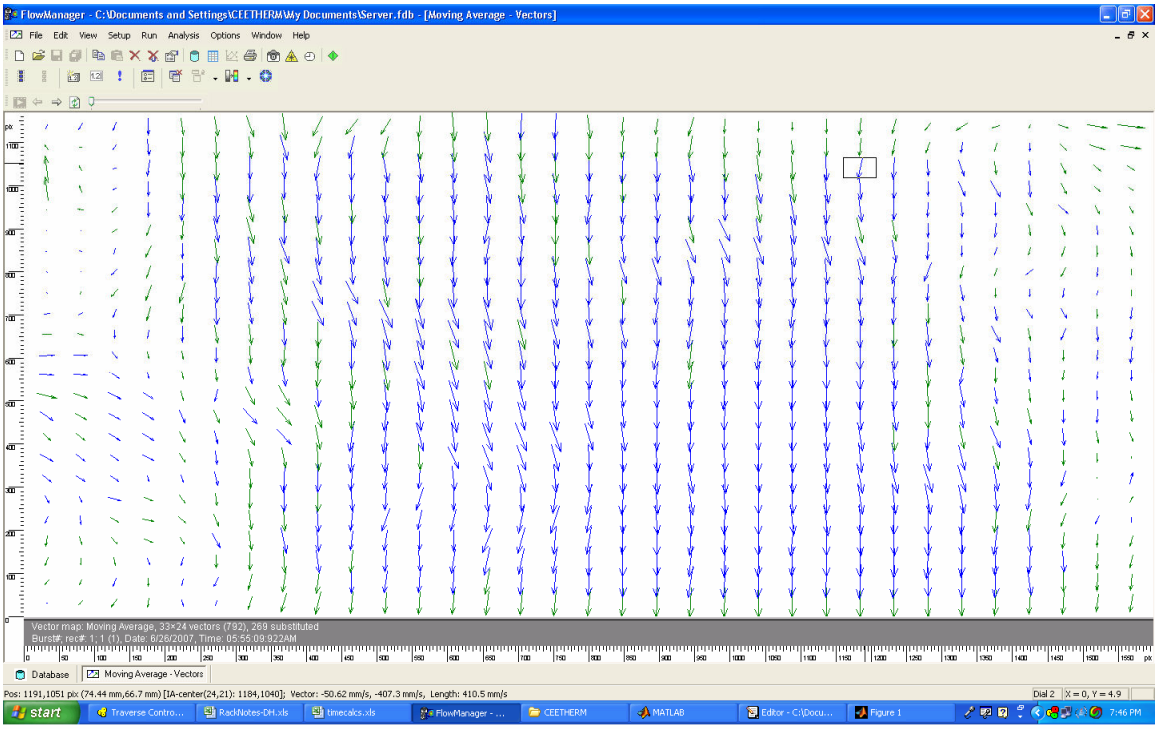

Figure A 7: PIV Velocity Vectors After Moving-Average Filter

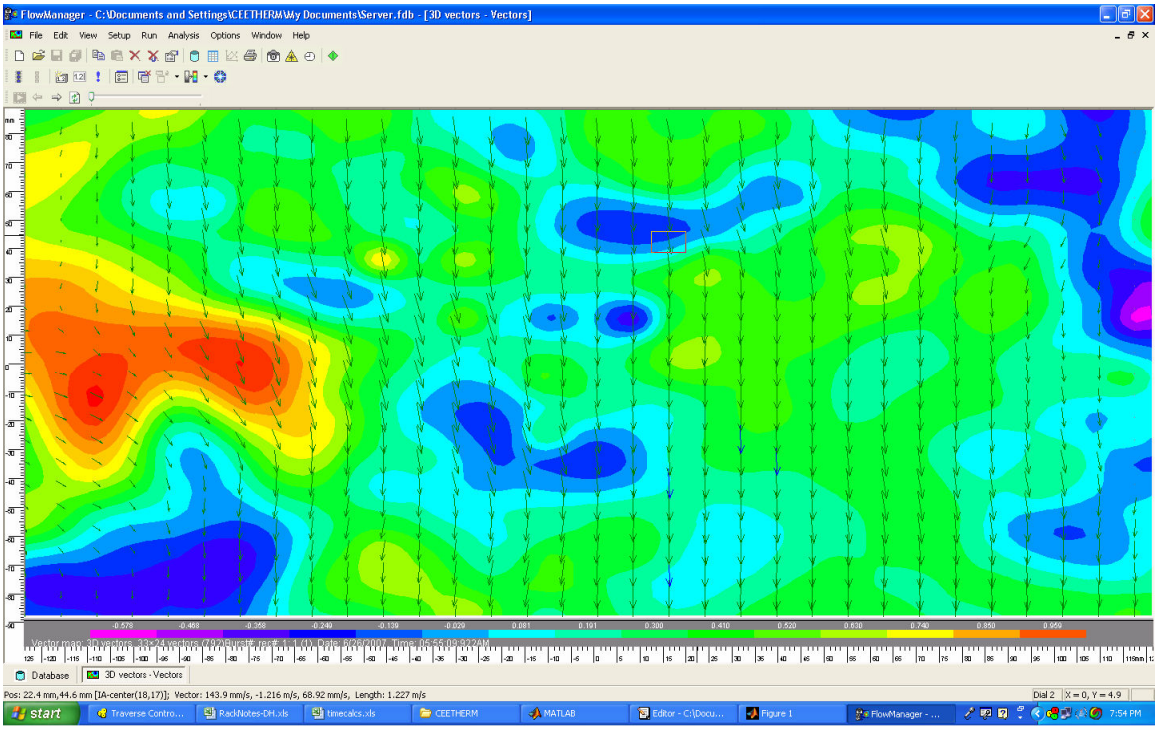

Figure A 8: PIV Velocity Vectors After 3D Calibration

After this, the velocity magnitudes of the second row from the top (a vertical row in space) were exported for each of the 40 images for each plane. The velocity magnitudes were then averaged, and the sub-plane results were then stitched together by deleting the velocity vectors near the edge of the image. The following Figure A 9 shows some representative results of the outlet velocity at each of the five planes as a function of height. So, the five images correspond to the five planes, which were taken at the center (x = 0), 3.5 inches to the left and right (x = -3.5 and x = 3.5, respectively), and 6.5 inches to the left and right (x = -6.5 and x = 6.5, respectively). A vertical position of 0 corresponds to the bottom of the server simulator, and 500 mm is at the top.

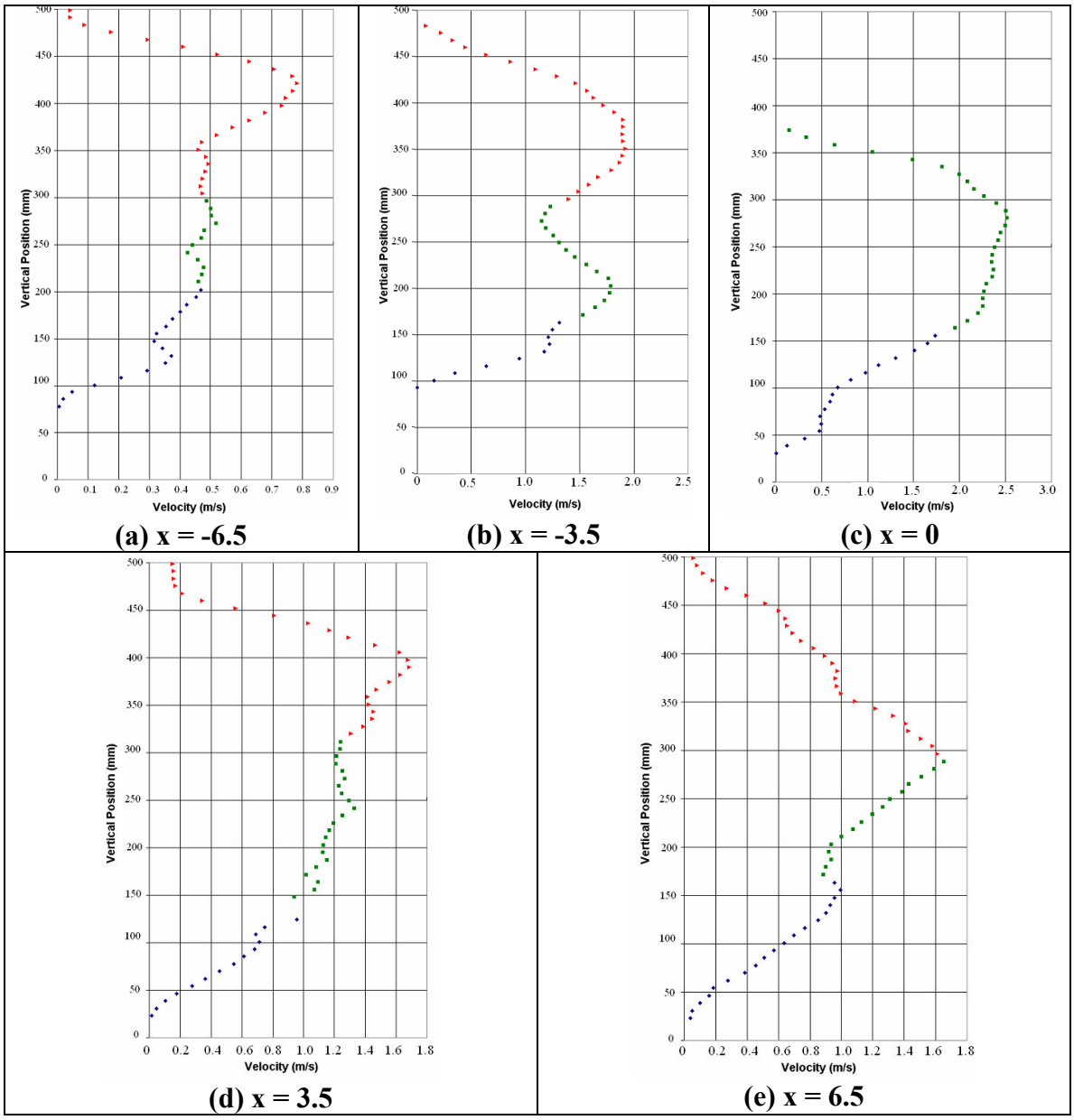

Figure A 9: PIV Explanation - Representative Outlet Velocity Results

It is important to point out that these five planes alone cannot be used to create a detailed outlet velocity map. They are useful, however, in that they provide information about general patterns. A handheld anemometer was used to check the validity of the PIV measurements (the magnitude of the velocities) – along with the validity of the outlet velocity profiles deduced from these measurements (the locations of the areas of high velocity).

APPENDIX F

IMPORTANT PARAMETERS

Table A 1: Important Dimensions

Server Simulator Width:	43.2 cm.	17 in.
Server Simulator Height:	44.5 cm.	17.5 in.
Server Simulator Depth:	68.9 cm.	27.125 in.
Rack Width:	58.4 cm.	23 in.
Rack Depth:	1.07 m.	42 in.
Heater Width:	6.35 mm.	0.25 in.
Heater Depth:	4.13 cm.	1.625 in.
Heater Height:	40 cm.	15.75 in.
Height of Fin Bank:	27 cm.	10.6125 in.
Number of Fins:	56	
Fin Width:	3.5 cm.	1.375 in.
Fin Depth:	5.1 cm.	2 in.
Fin Thickness:	0.635 mm.	0.025 in.
Fan Outer Diameter:	16.8 cm.	6.625 in.
Fan Hub Diameter:	8.26 cm.	3.25 in.
Inlet Metal Grid Opening Height/Width:	6.35 mm.	0.25 in.

Table A 2: Default k-ε Turbulence Model Inputs

$C_{1\varepsilon}$:	1.44
$C_{2\varepsilon}$:	1.92
C_{μ}:	0.09
σ_k:	1.0
σ_{ε}:	1.3

Table A 3: Important Model Boundary Condition Inputs

Inlet Temperature:	295.37 K
Inlet Gage Pressure:	0 Pa
Outlet Room Temperature:	295.37 K
Outlet Room Gage Pressure:	0 Pa
Dial 2 Fan Curve:	$\Delta p = -1.3482\upsilon^2 - 4.2157\upsilon + 29.069$
Dial 5 Fan Curve:	$\Delta p = -1.2956\upsilon^2 - 5.3161\upsilon + 39.731$
Dial 8 Fan Curve:	$\Delta p = -1.5669\upsilon^2 - 3.4639\upsilon + 54.803$
Heater 1, 3, 4, 5, 7 Volumetric Heat Generation:	1.415×10^7
Heater 2 Volumetric Heat Generation:	7.077×10^6
Heater 6 Volumetric Heat Generation:	3.539×10^6
Fin Bank Porous Media Porosity:	87%
Fin Bank Porous Media Viscous Resistance (1/α):	2.059×10^6
Fin Bank Porous Media Inertial Resistance (C_2):	13.08
Server Sim. Inlet Vent Pressure Drop Equation:	$\Delta p = 2.6\upsilon^2$
Server Sim. Outlet Vent Pressure Drop Equation:	$\Delta p = 0.4757\upsilon^2 + 1.4664\upsilon$
Rack Inlet/Outlet Vent Pressure Drop Equation:	$\Delta p = 0.0534\upsilon^2 + 1.0136\upsilon$

Table A 4: Estimation of Overall Measurement Uncertainties

Temperature Measurements:	≈ 0.875°C
Room Temperature:	≈ 0.35°C
Pressure Measurements:	≈ 0.7 Pa
Air Flow Rate:	≈ 7 CFM
PIV Velocity Measurements:	Unknown

REFERENCES

1. Rolander, N., *An Approach for the Robust Design of Air Cooled Data Center Server Cabinets*, in *Mechanical Engineering*. 2005, The Georgia Institute of Technology: Atlanta, GA.

2. Wang, D., *Cooling challenges and best practices for high density data and telecommunication centers*, in *The Conference on High Density Microsystem Design and Packaging and Component Failure Analysis*. 2006. p. 49-54.

3. Patel, C.D., Sharma, R., Bash, C.E., Beitelmal, A., *Thermal considerations in cooling large scale high compute density data centers*, in *The Eighth Intersociety Conference on Thermal and Thermomechanical Phenomena in Electronic Systems*. 2002. p. 767-776.

4. ASHRAE, *Thermal Guidelines for Data Processing Environments*. 2004, ASHRAE.

5. Schmidt, R., Karki, K., Kelkar, K.M., Radmehr, A., Patankar, S.V. *Measurements and Predictions of the Flow Distribution Through Perforated Tiles in Raised Floor Data Centers*. in *The Pacific Rim/ASME International Electronics Packaging Technical Conference and Exhibition*. 2001. Kauai, Hawaii.

6. Schmidt, R., Karki, K., Patankar, S., *Raised-floor data center: perforated tile flow rates for various tile layouts*, in *The Ninth Intersociety Conference on Thermal and Thermomechanical Phenomena in Electronic Systems*. 2004: Las Vegas, Nevada. p. 571-578.

7. Kang, S., Schmidt, R., Kelkar, K., Patankar, S., *A methodology for the design of perforated tiles in raised floor data centers using computational flow analysis.* IEEE Transactions on Components and Packaging Technologies, 2001. **24**(2): p. 177-183.

8. Rambo, J., Nelson, Graham, Joshi, Yogendra. *Airflow Distribution through Perforated Tiles in Close Proximity to Computer Room Air-Conditioning Units*. in *2007 ASHRAE Annual Meeting*. 2007. Long Beach, California.

9. Sharma, R., Bash, C., Patel, Chandrakant, Beitelmal, M., *Experimental investigation of design and performance of data centers*, in *The Ninth Intersociety Conference on Thermal and Thermomechanical Phenomena in Electronic Systems*. 2004. p. 579-585.

10. Patel, C.D., Bash, C.E., Sharma, R., Beitelmal, M. *Smart Cooling of Data Centers*. in *RIM/ASME International Electronics Packaging Technical Conference and Exhibition*. 2003.

11. Moore, J., Chase, J.S., Ranganathan, P., *Weatherman: Automated, Online and Predictive Thermal Mapping and Management for Data Centers*, in *IEEE International Conference on Autonomic Computing*. 2006. p. 155-164.

12. Poyyapakkam, M.N., Joshi, Yogendra K. *Computational Simulations of Server Room Cooling - A Parametric Study*. in *8th International Workshop on THERMal Investigations of ICs and Systems*. 2002.

13. Rambo, J., Joshi, Yogendra, *Thermal Performance Metrics for Arranging Forced Air Cooled Servers in a Data Processing Cabinet.* Journal of Electronic Packaging, 2005. **127**.

14. Patel, C.D., Bash, Cullen E., Belady, Christian. *Computational Fluid Dynamics Modeling of High Compute Density Data Centers to Assure System Inlet Air Specifications*. in *The Pacific Rim/ASME International Electronic Packaging Technical Conference and Exhibition*. 2001. Kauai, Hawaii.

15. Wang, D., *A passive solution to a difficult data center environmental problem*, in *The Ninth Intersociety Conference on Thermal and Thermomechanical Phenomena in Electronic Systems*. 2004. p. 586-592.

16. Nie, Q., Joshi, Y., *Multi-scale thermal modeling methodology for electronics cabinets*, in *The Tenth Intersociety Conference on Thermal and Thermomechanical Phenomena in Electronics Systems*. 2006. p. 7.

17. Baelmans, M., Meyers, J., Nevelteen, K., *Flow Modeling in Air-Cooled Electronic Enclosures*, in *Semiconductor Thermal Measurement and Management Symposium. Nineteenth Annual*. 2003, Institute of Electrical and Electronics Engineers, Inc. p. 27-34.

18. Kowalski, T., Radmehr, A., *Thermal analysis of an electronics enclosure: coupling flow network modeling (FNM) and computational fluid dynamics (CFD)*, in *Sixteenth Annual IEEE*. 2000, Institute of Electrical and Electronics Engineers. p. 60-67.

19. Incropera, F.P., DeWitt, David P., *Fundamentals of Heat and Mass Transfer, 5th Edition*. 5th ed. 2001: Wiley.

20. Loh, C.K., Chou, D.J., *Comparative analysis of heat sink pressure drop using different methodologies*, in *Semiconductor Thermal Measurement and Management Symposium. Twentieth Annual IEEE*. 2004. p. 148-153.

21. Lu, J., Duan, Xiao, *EMC computer modeling techniques for CPU heat sink simulation*, in *3rd International Conference on Computational Electromagnetics and Its Applications*. 2004. p. 272-275.

22. Linton, R.L., Agonafer, D., *Coarse and detailed CFD modeling of a finned heat sink*, in *IEEE Transactions on Components, Packaging, and Manufacturing Technology*. 1995. p. 517-520.

23. Rencz, M., Farkas, G., Szekely, V., Poppe, A., Courtois, B., *Boundary condition independent dynamic compact models of packages and heat sinks from thermal transient measurements*, in *5th Conference on Electronics Packaging Technology*. 2003. p. 479-484.

24. Narasimhan, S., Bar-Cohen, A., Nair, R., *Flow and pressure field characteristics in the porous block compact modeling of parallel plate heat sinks.* IEEE Transactions on Components and Packaging Technologies, 2003. **26**(1): p. 147-157.

25. Roknaldin, F., Sahan, R.A., Sun, X.H., *A simplified CFD model for the radial blower*, in *The Eighth Intersociety Conference on Thermal and Thermomechanical Phenomena in Electronic Systems*. 2002. p. 600-604.

26. Temmerman, W., Christiaens, Baelmans, M., *Application of Fan Models for Thermal Simulation*, in *ISPS*. 1997. p. 81-86.

27. Thurlow, E., Prather, E., Mansingh, V., *Fan swirl effects on cooling heat sinks and electronic packages*, in *Sixteenth Annual IEEE Semiconductor Thermal Measurement and Management Symposium*. 2000. p. 91-98.

28. NI, *FieldPoint Operating Instructions*, in *FP-TC-120 and cFP-TC-120 8-Channel Thermocouple Input Modules*. 2002, National Instruments Corporation.

29. Dantec, *FlowManager Software and Introduction to PIV Instrumentation*, in *Software User's Guide*. 2002, Dantec Dynamics.

30. Fluent, *Fluent 6.2 User's Guide*, Fluent, Inc.

31. Schmitz, N., *SF Pressure Drop 6.2 Help Menu*, Software-Factory, Editor. 2005, Software-Factory: Schifferstadt, Germany.

32. Panton, R.L., *Incompressible Flow, Second Edition*. 1996, New York: John Wiley & Sons, Inc.